Architecture for a Mobile Robotic Camera Positioning System for Photogrammetric Data Acquisition in Hydroelectric Tunnels

by

Ryan Daniel Keizer

BScE, University of New Brunswick, 2021

A THESIS SUBMITTED IN PARTIAL FULFILLMENT OF THE REQUIREMENTS FOR THE DEGREE OF

Master of Science in Engineering

In the Graduate Academic Unit of Mechanical Engineering

Supervisors:	Rickey Dubay, PhD, Mechanical Engineering
	Lloyd Waugh, PhD, Civil Engineering
Examining Board:	Clodualdo Aranas, PhD, Mechanical Engineering
	Mohsen Mohammadi, PhD, Mechanical Engineering
	Shabnam Jabari, PhD, Geodesy & Geomatics Engineering

This thesis is accepted by the
Dean of Graduate Studies

THE UNIVERSITY OF NEW BRUNSWICK

April, 2023

© Ryan Daniel Keizer, 2023

Abstract

The structural condition of hydroelectric tunnels is important to the overall performance, safety, and longevity of generating stations. Significant effort is required to inspect, monitor, and maintain these tunnels. Photogrammetry is an effective method of collecting highly accurate visual and spatial data. However, it also presents the complex challenge of positioning a camera at thousands of difficult to reach locations throughout the large and varying-diameter tunnels.

A robotic semi-automated camera positioning system was developed to enhance the collection of images within hydroelectric tunnels for photogrammetric inspections. A continuous spiral image network was developed to optimize the collection speed within the bounds of photography and capture-in-motion constraints. The positioning system and image network optimization reduce the time and effort required, while providing the ability to adapt to different and varying tunnel diameters. To demonstrate, over 28,000 images were captured at a ground sampling distance of 0.4 mm in the 822 m long concrete-lined section of the Grand Falls Generating Station.

Acknowledgements

This project and influential stage of my life would not have been achievable without the support and contributions of many great individuals; my gratitude is indescribable. Thank you:

To my friends and family, near and far, for providing the perfect balance of motivation, encouragement, and distraction needed to get through this journey.

To my supervisors Dr. Lloyd Waugh and Dr. Rickey Dubay for your continuous support and invaluable advice throughout this process. Your guidance and selflessness is unmatched and has greatly influenced me and my future. Thank you for this opportunity.

To Cody Bradley, this project could not have been successful without your dedication and irreplaceable knowledge throughout. Your passion and enthusiasm in this field and in life are an inspiration. I am very grateful for the experience and opportunities you have, and continue to, present to me.

To David and Peggy Bradley, for providing incredible hospitality and workspace to test and work on the ATI, and for serving up the best coffee and homemade bread I have ever had.

To Allan Robinson and Brian Guidry, for sharing your knowledge and technical assistance with electronic and mechanical aspects of the ATI.

To Ferro's Portable Welding, for fabricating the structure of the ATI.

To Bradley Engineering Ltd., the New Brunswick Innovation Fund, Mitacs, and the University of New Brunswick for funding this research.

Table of Contents

Abstract ii

Acknowledgments iii

Table of Contents v

List of Tables viii

List of Figures ix

Abbreviations and Acronyms xii

1 Introduction 1
- 1.1 Problem Statement . . . 3
- 1.2 Objectives . . . 4
- 1.3 Scope . . . 6
  - 1.3.1 Assumptions . . . 6
  - 1.3.2 Limitations . . . 8
- 1.4 Significance . . . 10
- 1.5 Motivating Case . . . 11
  - 1.5.1 Limitations in Previous Image Collection Methods . . . 11
- 1.6 Readers' Guide . . . 14

2 Literature Review 16
- 2.1 Bradley Engineering Ltd. History . . . 16
- 2.2 Motivation for Technological Innovation . . . 19
  - 2.2.1 Safety and Accessibility . . . 19
  - 2.2.2 Financial Benefit . . . 20
  - 2.2.3 Quality and Consistency . . . 21
- 2.3 Inspection Technologies . . . 21
  - 2.3.1 Unoccupied Underwater Vehicles . . . 22
  - 2.3.2 Unoccupied Aerial Vehicles . . . 22
  - 2.3.3 Terrestrial Vehicles . . . 24
- 2.4 Navigation and Positioning . . . 27
  - 2.4.1 Relative Localization . . . 28
  - 2.4.2 Absolute Localization . . . 30
- 2.5 Model Predictive Control Implementations . . . 32

3 Methodology and Theory **33**
3.1 Research Methodology . . . 33
3.1.1 Formulation and Design . . . 33
3.1.2 Construction and Assembly . . . 34
3.1.3 Testing . . . 35
3.2 Robotics Theory . . . 36
3.2.1 Serial Manipulator: Spatial Relation . . . 37
3.2.2 Serial Manipulator: Kinematics and Dynamics . . . 37
3.3 Vehicle Dynamics Theory . . . 38
3.3.1 Dynamic Model of Vehicle Motion . . . 39
3.3.2 Rolling Resistance . . . 40
3.3.3 Grade Resistance . . . 41
3.3.4 Maximum Tractive Effort . . . 41
3.4 Controls Theory . . . 42
3.4.1 Proportion-Integral-Derivative Control . . . 43
3.4.2 Model Predictive Control . . . 44

4 Conceptualization and Design **47**
4.1 Design Considerations and Criteria . . . 47
4.2 Concepts Considered . . . 49
4.2.1 Cantilever Concept . . . 49
4.2.2 Double-Mast Concept . . . 50
4.2.3 Stewart Platform Concept . . . 52
4.2.4 Boom Truck Concept . . . 52
4.3 Evaluation and Decision Rationale . . . 54
4.3.1 Evaluation . . . 54
4.3.2 Decision Rationale . . . 55

5 Detail Design and Analysis **57**
5.1 Arm Manipulation . . . 58
5.1.1 Arm Rotation . . . 59
5.1.2 Arm Radial Extension . . . 59
5.1.3 Orientation Control . . . 60
5.2 Boom Manipulation . . . 61
5.2.1 Simulation Analysis . . . 62
5.2.2 Analytical Analysis . . . 64
5.2.3 Specifications and Components . . . 69
5.3 Base Maneuvering . . . 71
5.3.1 ATI Drive Control Concept . . . 71
5.3.1.1 Translation . . . 71
5.3.1.2 Curve Following and Rotation . . . 72
5.3.2 Components and Simulations . . . 74

6 Control Systems **76**
6.1 General Control . . . 78

6.2 Arm Radius Synchronization 79
6.3 Drive Controls 83

7 Continuous Spiral Photogrammetric Image Network 88
7.1 Image Sequencing 88
7.2 Image Density 91
7.3 Continuous Image Capture Rate Analysis 94
7.3.1 Motion Blur Limitation 94
7.3.2 Image Capture Rate Limitation 95
7.3.2.1 Flash Refresh Rate 96
7.3.2.2 Orientation Change Timing 97

8 Implementation at the Grand Falls Hydroelectric Generating Station 99
8.1 Grand Falls Generating Station Overview 99
8.2 Acquisition Process Discussion 100
8.3 Results and Comparisons 107

9 Conclusions and Recommendations 111
9.1 Conclusions 112
9.2 Recommendations 114
9.2.1 Researchers 114
9.2.2 Bradley Engineering Ltd. 115
9.2.3 Industry 117

Bibliography 122

A Robot Kinematic Calculations 123

B ATI Details and Visuals 127

C Additional Control Data 132

Vita

List of Tables

1.1 Mactaquac and Grand Falls Tunnel Comparison 12

4.1 Concept Relative Evaluation Table 55

5.1 Arm Manipulation Simulation Summary 58
5.2 Boom Manipulation Simulation Summary 63
5.3 Modified Denavit-Hartenberg Parameters of the ATI. 66
5.4 Parameter definitions for driving actuators of the lift and tip joints. . 69

7.1 Flash Refresh Rate Test Results 97

8.1 Work Day Itinerary Breakdown 101
8.2 Grand Falls Tunnel Scan Comparison 108

A.1 Modified Denavit-Hartenberg Parameters of the ATI. 123
A.2 Parameter definitions for driving actuators of the lift and tip joints. . 124

B.1 Linear Actuator Summary 131

C.1 Summary of estimated model data from open loop data 135

List of Figures

1.1 Grand Falls intake tunnel, steel-lined distribution section. 2
1.2 Entrance to penstock through side of scroll-case in Mactaquac. 13

2.1 Model of TIA, capture rig used for Mactaquac and Grand Falls. [5] . 17
2.2 Example of resulting Grand Falls model, including a wireframe view on the left and textured model on the right. [5] 18
2.3 Micro Aerial Vehicle used in [42, 41, 40]. 24
2.4 Monorail-based visual inspection system [46]. 26

3.1 Dynamic model of a vehicle moving up a sloped surface. [14] 39
3.2 Representation of the effect of rolling resistance. [14] 40
3.3 Block Diagram of general Proportional-Integral-Derivative (PID) system. [11] 43
3.4 General MPC architecture [20] 45

4.1 Cantilever Concept 50
4.2 Double-Mast Concept 51
4.3 Stewart Platform Concept 53
4.4 Boom Truck Concept 54

5.1 Simulation of arm manipulation components: orientation rotation, arm extension, arm rotation 59
a Start position (t=0s) 59
b Mid-operation (t=17s) 59
c End position (t=30s) 59
5.2 Arm rotation simulation dynamic response. 60
5.3 Arm extension simulation dynamic response 61
5.4 Camera orientation rotation simulation dynamic response. 62
5.5 Simulation of boom manipulation components: boom extension, boom inclination, tip inclination. 63
a Starting lowered position (t=0s) 63
b Mid-operation (t=16s) 63
c End elevated position (t=32s) 63
5.6 Arm frame elevation simulation: Inverse kinematics and dynamics . . 64
5.7 ATI joint frame and DH parameter definitions. 65
5.8 Defining parameters relating driving actuator of boom inclination joint. 68
5.9 Defining parameters relating driving actuator of tip inclination joint. 68

5.10 Properties defining wheel direction and velocity when rotating or following a curve. . . . 73
5.11 Resulting wheel torque requirements from simulations of increasing surface slope at speed of 10 m/min. . . . 75

6.1 Schematic of component layout and connectivity. . . . 77
6.2 Schematic diagram for general ON/OFF control system. . . . 79
6.3 Schematic diagram for general PID control system. . . . 79
6.4 Schematic diagram for synchronized position and velocity control of the radial arm extensions. . . . 80
6.5 Open loop data of the analytical model compared with experimental data of the arm actuators. . . . 81
6.6 Closed loop data of the analytical arm model. . . . 82
6.7 Closed loop data of the physical arm system. . . . 82
6.8 Schematic diagram for drive system controlling wheel velocities. . . . 83
6.9 Open loop experimental and analytical drive responses from various input percentages. . . . 84
6.10 Closed loop MPC response with varying control horizon. . . . 85
6.11 Closed loop MPC response with tuned parameters. . . . 86
6.12 Closed loop experimental MPC response with tuned parameters. . . . 87

7.1 Piece-wise image sequence camera paths, black and green differentiating each camera. . . . 89
7.2 Continuous image sequence camera paths, purple and green differentiating each camera. . . . 90
7.3 Camera capture locations on flattened surface projection for the example image network. . . . 92
7.4 Image density heat map on a flattened surface projection for an example image network. . . . 93

8.1 ATI assembled upstream from equipment hoist location. . . . 102
8.2 Example of water sprays within tunnel. . . . 103
a Water spray and deterrent method. . . . 103
b Close up of spray source. . . . 103
8.3 Gorge - large pothole defect at the invert of the tunnel. . . . 105
8.4 Elbow at intake end of the tunnel. . . . 106
8.5 Long exposure photo of the ATI scanning the tunnel. . . . 109
8.6 Snapshot of model created from the images captured during this scan. 110

A.1 ATI joint frame and DH parameter definitions. . . . 125
A.2 Defining parameters relating driving actuator of boom inclination joint. 126
A.3 Defining parameters relating driving actuator of tip inclination joint. 126

B.1 ATI in the Grand Falls tunnel. . . . 127
B.2 ATI actuation definitions. . . . 128
B.3 ATI in the shop and testing environment. . . . 129

B.4 ATI model in different extensions. 130
B.5 Boom tip system: tip inclination actuator and arm rotation platform. 130

C.1 Experimental stroke response of the lift actuator from various inputs. 132
C.2 Experimental responses showing the effect of load on speed and stroke of the arm extension actuators. 133
C.3 Open loop drive wheel responses at various inputs. 134
C.4 Open loop drive wheel responses at various low range inputs. 134
C.5 Simulated responses from each wheel's estimated analytical model at various mid range inputs. 135

List of Abbreviations and Acronyms

AGV	Automatic Guided Vehicle
ATI	Automated Tunnel Inspector
BE	Bradley Engineering Ltd.
CAD	Computer Aided Design
DOF	Degree(s) of Freedom
DSLR	Digital Single Lens Reflex
FRR	Flash Refresh Rate
Grand Falls	Grand Falls Generating Station
GSD	Ground Sampling Distance
GUI	Graphical User Interface
ICR	Image Capture Rate
IMU	Inertial Measurement Unit
Mactaquac	Mactaquac Generating Station
MAV	Micro Aerial Vehicle
MIMO	Multiple-Input-Multiple-Output
MPC	Model Predictive Control
mDH	modified-Denavit-Hartenberg
nMPC	nonlinear Model Predictive Control
NB Power	New Brunswick Power Corporation
OL	Overlap

PID	Proportional-Integral-Derivative
ROM	Ranges of Motion
ROV	Remotely Operated Vehicle
SISO	Single-Input-Single-Output
TIA	Tunnel Inspection Assistant
UAV	Unoccupied Aerial Vehicle
UWB	Ultra-Wide Band

Chapter 1

Introduction

High-resolution visual and spatial models are enhancing traditional methods of inspecting large-scale structures. Data collection for these models can be accomplished with lidar; however, photogrammetry can produce RGB point clouds that can be inspected visually. These improved models overcome the inaccuracy and uncertainty of traditional inspection methods and enable better understanding of infrastructure condition and deterioration trends.

Typical hydroelectric generating stations have multiple penstocks, and many have additional associated tunnels as well. These tunnels are often kilometers long and upwards of 10 m in diameter; the Grand Falls Generating Station (Grand Falls) intake tunnel is 7.5 m in diameter and the concrete-lined section is 822 m long for example. Traditional walk-throughs of these large tunnels can be time consuming as is, and the collection of photogrammetric data throughout only increases that issue. Current photogrammetric data acquisition methods are primarily manual and have been generally developed to only capture a specific tunnel diameter. Figure 1.1 shows the distribution section of the Grand Falls intake tunnel, providing an example visual of the size and conditions of these tunnels.

Figure 1.1: Grand Falls intake tunnel, steel-lined distribution section.

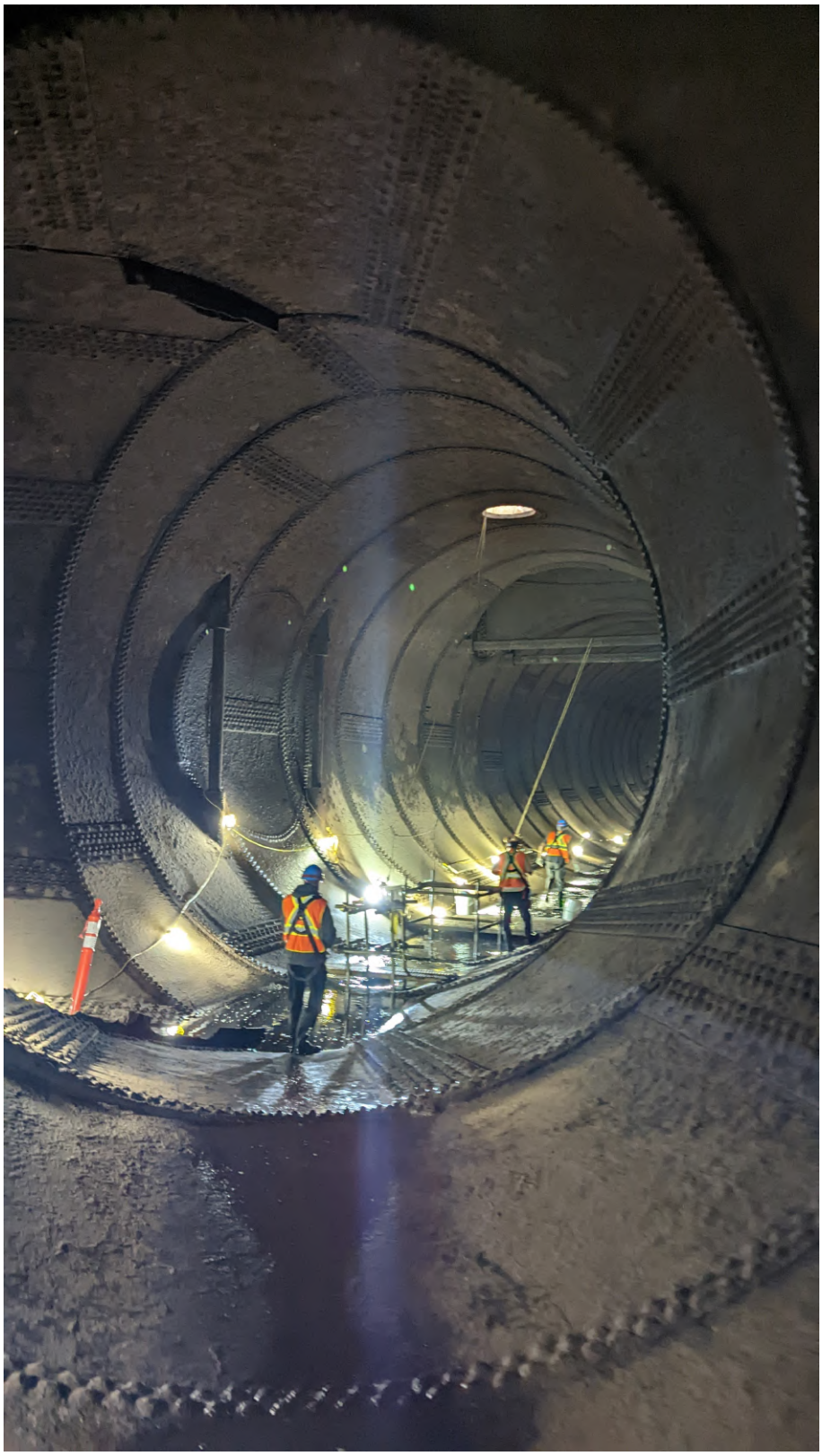

1.1 Problem Statement

The current methods of collecting photogrammetric data at the high quality and resolution that is desired consist of primarily manual tasks that demand great labor efforts especially in large tunnels. This process is time intensive and takes longer than a traditional walk-through by an inspector. With individual generating stations having different diameter tunnels or multiple different stations being inspected by the same equipment, tunnel-specific image capture methods are inefficient, costly and require substantial modifications to capture unique locations.

The shutdowns come at a significant expense as replacement electricity must be outsourced during the downtime. In New Brunswick, the Mactaquac Generating Station (Mactaquac) has a 670 MW capacity, and the Grand Falls generating station is 66 MW. For example, the cost of replacement electricity for the smaller Grand Falls station was estimated as $38,000 per day [5] and lasted for 10 days in 2017. The cost increases for larger generating stations and can be substantially higher for unplanned shutdowns. The image collection process consumes a significant portion of these downtimes, signifying how impactful the data collection speeds are to the overall maintenance expense. The two stations mentioned are only a small example of the over 100 hydroelectric power stations in Canada that have a capacity over 100 MW [10], with numerous others of smaller size.

Identifying these limitations and challenges in the process led to the understanding that introducing robotic and automated elements to the image acquisition process could allow a wide range of tunnels to be inspected with a single system while maintaining consistent model quality and properties. Evaluating potential image collection sequences to optimize the speed and manual efforts of the process while maintaining an effective density of images and overlap to create quality models can lead to a more optimized process. Three elements of research evolved from the

understanding of the image collection process demands and robotic system design, including the collection procedure, robotic systems, and efficient intuitive design.

The overarching research question for this work is:

What data acquisition system design is best suited to improve the efficiency of the photogrammetric data collection process in a tunnel, and accounts for tunnel diameter variability and transportability?

Which is expanded to three key questions, which are:

- What image acquisition and sequence is best suited to improve the efficiency of the photogrammetric image collection process.
- How could the proposed image collection system be automatically adjustable to account for the variability in tunnel diameters.
- How could the system be designed to be modular and transportable to allow the operators to complete the transportation, assembly, and disassembly without the need of external support.

1.2 Objectives

The goal of this research was to develop a mobile robotic camera positioning system that improves the efficiency of the tunnel image collection process, while prioritizing adaptability and transportability through a variable and modular design. The system developed in this work will herein be referred to as the Automated Tunnel Inspector (ATI). The term automated in this context refers to the system being made to be operated by the combined electromechanical and control systems to reduce the effort and work done by humans, based on the Cambridge definition in [8].

The specific key objectives of this research are:

- To identify and evaluate the optimal image capture sequence to minimize the time required to complete the collection process while maintaining consistent and sufficient image overlap and density.
- To develop a automated robotic image collection system capable of adapting to a range of tunnel diameters and allow for easy independent transportation into, and out of, the confined tunnels.
- To collect a complete set of images for photogrammetric analysis of the Grand Falls Generating Station intake tunnel.
- To evaluate and demonstrate the use of advanced control techniques in unique environments and applications.

Maintaining correct and consistent image properties is critical for ensuring the subsequent photogrammetric analysis is effective. This sets strict constraints on where the images must be captured. Therefore, optimizing the sequence and method whereby these image locations are navigated, significantly influences the time required to move throughout a complete network of images.

Transportability in the context of this project pertains to the limited access presented by these tunnels, including a small-sized access point within a close-quarter environment and the manual ferrying of the system in and out of the tunnel. In the case of the Mactaquac penstocks, access is via a small access point located on the side of the scroll-case which is only large enough for a person to squeeze through. The path to get to this access point porthole involves multiple levels of stairs, the use of hoists and the need to climb down an enclosed ladder into the confined location of the porthole. Therefore, addressing this goal includes a design with the ability to be modularly reduced into compact components capable of being transported manually by operators into the limited-access tunnels. The adaptability that is required stems from the variations that are present among the large number of hydroelectric tunnels currently in use. Not only are the diameters of different tunnels unique, but some

individual tunnels also contain varying diameters and profiles to be followed. Hence, adapting to these tunnel variations was a key aspect of the research objectives.

The hydroelectric generating station in Grand Falls was the target infrastructure for this project. Conducting the complete image acquisition process in this tunnel was be used for the demonstration and evaluation of the designed system.

These hydroelectric tunnels pose a unique set of constraints and that require high performing controls to effectively operate in these conditions. The implementation and evaluation of various control methods in this environment demonstrates the versatility and robustness of these control techniques in harsh dynamic environments.

1.3 Scope

1.3.1 Assumptions

Throughout the stages of the project, assumptions had to be made due to potential variability in elements such as environmental aspects or instrument performance. The project defining assumptions are identified below.

As there is significant variability in the tunnels that could be considered, assumptions have been made on the applicable tunnels to construct the framework of the project. The tunnels being considered are primarily cylindrical with diameters ranging from 4.5-9 m. The longitudinal profiles can also vary significantly, therefore it has been assumed that the typical range of slopes is between a 0% and 10% incline, and do not include abrupt discontinuities. Additionally, access to these areas change from location to location, therefore a baseline must be set. Based on the porthole size in the scroll-case at the Mactaquac generating station, and the definition that a human must be able to access the area, the assumed entrance is a 0.7 m diameter porthole.

A key aspect that influences the mobility of the system is the tunnel surfaces, including material type, texture, and condition. The tunnel surface is generally either concrete such as at Grand Falls, or steel-lined such as the penstocks at Mactaquac. After draining, the tunnels are often still wet and the presence of a small water stream at the invert of the tunnel is common. Naturally, the collection of silt throughout the tunnel after draining is also expected; although measures can be taken to reduce this such as pressure washing of some surfaces which occurs in Mactaquac, it is assumed that silt may affect the system's interactions with the surface.

The environmental variability posed the need for a range of assumptions. This begins with the ambient temperatures within the tunnels being within the range of 5°C to 20°C; considering this will ensure the selected components are operable within that range. Another influence on component selection is the environmental conditions, including the presence of water and dust. While not measured, rather based on experience in the tunnels, consideration must be given to protection against water drops and splashes, but garden hose-like sprays or submersion scenarios are assumed to be avoided during operation. Regarding air quality, the degradation of image quality due to airborne dust or fog interference is the limiting factor during operation. However, non-photography components may remain in the tunnel overnight or for an extended period while other activities are occurring. Therefore, moderate protection from dust and humidity is required for mechanical and electrical components.

A fundamental element of this research is the capture of images with high-resolution cameras. Specifications and properties of the camera equipment such as focal length and sensor dimensions are used in determining the capture positions required. However, it was assumed based on the experience of Bradley Engineering Ltd. (BE) that the cameras will operate as expected when properly instructed if stably positioned and calibrated by an experienced operator during set up.

1.3.2 Limitations

In the early stages of this project, the problem definition was broad and included a wide range of potential areas of investigation. To narrow the scope of the project to one that was feasible for successful completion within the time frame, various aspects of the problem were excluded or constrained based on importance and practicality. The defined scope and notable limitations based on the assumptions made are identified in the following.

The underlying task fueling this project of photogrammetric analysis of a tunnel is a long multistage process involving planning, data acquisition, photogrammetric analysis of the acquired data, and the effective formulation and presentation of information. This research targets the elements of the data acquisition process, and more specifically, the relationship between image requirements and camera positioning within the tunnel. Therefore, the photogrammetric analysis aspect is not within the scope of this research; however, it is a significant influence on limitations and constraints of the system. It has direct influence on the number of images required and the location of each. Photography equipment and properties themselves are not a direct part of this project scope, although the impact they have on the collection procedure, such as constraints on image capture while in motion, is critical and studied throughout.

To summarize the limitations and the previously outlined assumptions which have been placed on the scope of the project, the tunnels that are considered within the scope are:

- Are generally of a cylindrical shape,
- Have diameters ranging between 4.5 m and 9 m,
- Include a continuous longitudinal profile,
- Have a maximum longitudinal slope of 10%,

- Have an access point of 0.7 m or larger in diameter.

Tunnels that do not meet all these specifications are not considered in this project.

While navigation and positioning of the system within the tunnel environment is a key aspect of the research, due to the complexities presented by the tunnel environment and the time frame available, automation of localization and navigation have been excluded from the scope. While the idea of having a fully automated system was considered, a high-level human-in-the-loop inclusion is an effective solution to advancing the process at this stage.

In a large system that integrates mechanical structures, electro-mechanical actuation components, and various sensors, the underlying control system can be complex. While advanced control schemes will be implemented and tested on the system, the complete optimization and stability analysis of the control will not be investigated as it is beyond the scope of this work. The effect of this will be mitigated in the more conservative approach taken when implementing the controls but is not a detriment to the results. Integrating an effective overarching user control and interface is an important part of a fully functional image collection system, optimizing this aspect was not critical for the current stage of this project.

A key aspect to identify is this project's focus on the design and advancement of the hydroelectric tunnel image collection process. While including general elements of mechanical and structural analysis in the design, this is not a primary aspect of this work. This means that exhaustive analysis of elements such as joints and welds, material and component life cycle, and finite element analysis, are not specific details of this project's scope. Focus is on addressing and overcoming the outlined process challenges and limitations, along with demonstrating the use of various control techniques in the hydroelectric environment and advancing the foundation for automation in this field.

1.4 Significance

This work builds on previous and current research being done around the world with the focus of improving and automating the image collection process of photogrammetric inspections for tunnels and infrastructure with similar environments and constraints. This research demonstrates the integration of mechanical, electrical and software elements applied in a unique environment; but also provides means for a range of potential research opportunities.

In the most direct sense, the work of this research impacts the data acquisition process and results at the Mactaquac and Grand Falls hydroelectric generating stations, where BE previously and currently performs photogrammetric analysis. New Brunswick Power Corporation (NB Power) can see great benefit from improvement of the image collection speed as it reduces the amount of time required to be spent capturing data within the tunnels; allowing for a reduction in tunnel downtime or allowing a greater portion of the downtime to be allocated to maintenance. This time and effort savings during the acquisition process can have an immediate economic impact on NB Power and thereby enhance its maintenance program overall. The adaptability proposed by this system will allow BE to inspect areas of Mactaquac that were previously more difficult to capture, such as the scroll-case. This also facilitates the opportunity to easily adapt to other generating stations without the need to build another custom system.

While this research is being explored and implemented in these New Brunswick hydroelectric generation stations, the implementation of faster methods and technologies supporting high-quality photogrammetric inspections can be directly applied to hydroelectric tunnels in any location with the expectation of similar results. Effective demonstration of this research's primary objectives may eventually lead to a widespread adoption of these inspection practices in the hydroelectric industry.

Furthermore, this innovation has potential for adaptation as the image acquisition method for other hydroelectric infrastructure (such as turbine chambers and rectangular draft tubes), as well as the inspection of tunnels in highway, railroad, and subway systems.

1.5 Motivating Case

The current methods of collecting images in the Grand Falls intake tunnel and penstocks at Mactaquac are limited in their application and efficiency which affects the overall inspection process. Analysing the image collection process presented an opportunity for an advanced image collection system to overcome the limitations and improve the collection process.

1.5.1 Limitations in Previous Image Collection Methods

The current photogrammetric data collection methods being applied, as outlined in Section 2.1 of this thesis, provide leading edge results at resolutions and accuracy that are not achieved in many scenarios, let alone in the constricting environment and atmosphere of a hydroelectric tunnel. However, the method and equipment used for collecting the required data are limited and leave much to be desired. The key limitations of the process are:

- Camera positioning rig has been rigidly built for each specific tunnel and is not applicable to tunnels of other or varying diameters,
- The incremental image scan approach demands significant manual effort and time; an inefficient procedure,
- Difficulty transporting equipment into the confined tunnel as it requires alternative entrance point and assistant from site workers.

At the time of this study, this form of photogrammetric image collection has been implemented in two areas of two different generating stations: the penstocks at Mactaquac and the intake tunnel at Grand Falls. The properties of these tunnels are outline in Table 1.1. To capture images that are equivalent quality, maintain camera properties, and ensure correct overlap between images, these tunnels require the camera to travel through unique trajectories and therefore required the construction of two, slightly different, assistive rigs to move the cameras about the tunnel. Extending this to the vast range of potential hydroelectric tunnels that could be inspected, becomes a significant barrier for application of the photogrammetric inspections.

Table 1.1: Mactaquac and Grand Falls Tunnel Comparison

	Mactaquac	Grand Falls
Tunnel Type	Penstock	Intake
Diameter	8.8 m	7.5 m
Length	65 m	921 m
Slope	25%	1%
Features	Reducing diameter in the scroll-case	Horizontal curve near distributor

The previous image collection procedure itself was effective at obtaining the required images at the required locations. However, the process of doing so requires significant manual efforts as the assistive rig is pushed or pulled by the operators between each capture station. As well, at each station as the cameras are rotated around the tunnel, they must stop and allow time for the arm to settle at each capture angle around the path, all before accelerating to continue the process. The combination of manually moving the rig between stations and pausing rotation at each capture angle leads to a single capture rotation taking many minutes to complete. This incremental sequence becomes a significant limitation on the potential overall image acquisition speed.

Figure 1.2: Entrance to penstock through side of scroll-case in Mactaquac.

Gaining access to these tunnels can be a challenge. Entrance often involves passing through confined spaces including ladders, hoists, and portholes frequently as small as 0.7 m in diameter, merely large enough for the average person to pass through. Ferrying equipment through these passages is an effortful task. In Grand Falls, personnel enter the tunnel by descending a ladder through an access hatch at the crest of one of the scroll-case unit's tunnel and traverse up the manifold to the main intake tunnel. Equipment and materials are lowered in through a 1 m square hatch located upstream from the distributor. Access at Mactaquac is similarly through a small 0.7 m access hatch in the side of the scroll-case at the base of the penstock, as shown in Figure 1.2. The current assistive rig is not able to fit through this and demands an alternative access point that requires site personnel and a crane

to lower it down the penstock intake to then be guided down to the scroll-case. These methods of accessing the tunnel apply significant size and weight limitations on equipment to be used within the tunnel and are not unique to these stations.

1.6 Readers' Guide

For convenient reference, this thesis is organized as follows:

- Chapter 2 explores the many influencing factors in the demand for advanced and automated inspection and data acquisition methods. It covers the current state of the art of inspection methods and technologies for similar infrastructure and applications. The technology reviewed includes both Unoccupied Aerial Vehicle (UAV) and terrestrial based vehicles used for collecting a range of data types, various aspects of localization and navigation, and examples of Model Predictive Control (MPC) being implemented within related systems.
- Chapter 3 provides a theoretical background on the concepts and methodologies that formulate the work in this project. The general principles of vehicle dynamics relating to the systems mobility are outlined. Along with the robotic kinematics of serial manipulators that define the camera articulation from the base. Fundamental and advanced control theories of Proportional-Integral-Derivative (PID) and MPC are described as the implemented control techniques.
- Chapter 4 details the complex set of criteria and considerations for conceptualizing designs for this application. A set of concepts that were considered in the process are described and critiqued, and the evaluation process and decision rationale are outlined as well.
- Chapter 5 documents the design and analysis of all aspects of the data ac-

quisition system. The design and subassemblies are described in detail. The process of modelling and kinematic and dynamic analysis is detailed, providing the specifications for actuating components.

- Chapter 6 covers the interfacing of all electromechanical and control components. The concepts and formulation of the control techniques and analytical models applied are outlined before demonstrating a range of open and closed loop data in a simulated and experimental environment.
- Chapter 7 discusses a set of studies relating to the photography and image network that support the data acquisition process. The analysis of image capture sequences and the relations with image density and operation speeds are outlined. The identification of factors limiting the operation speed are detailed.
- Chapter 8 details the experience and results from the implementation of this technology at Grand Falls. The image collection procedure, obstacles, and results are discussed and compared to the experience of a previous operation in the same environment.
- Chapter 9 outlines the conclusions of this research work and provides recommendations on potential future improvements, how researchers can expand on this foundation work, and how the technology can be commercialized and integrated for adoption in the industry.

Chapter 2

Literature Review

2.1 Bradley Engineering Ltd. History

The Grand Falls Generating Station (Grand Falls) in New Brunswick, owned by New Brunswick Power Corporation (NB Power), has been in operation for nearly a century and has a total output capacity of 66 MW. The intake tunnel for this station diverts water from the Saint John River and is approximately 921 m long, which includes an 822 m concrete tunnel as well as the manifolds and additional steel lined sections. Traditionally the inspection of this tunnel has been completed visually with an inspector viewing from the tunnel invert with observations documented by location (longitudinal and clock location), size, and inspector comments on deterioration. Bradley [5, 6] identified major limitations in this process; the difficulty of visualizing deterioration trends throughout the tunnel, the low accuracy of defect descriptions,the low accuracy of the defect locations, and the overall subjectivity of the documentation due to interpretations.

Bradley developed a photogrammetric inspection system capable of providing high resolution visual imagery as well as high spatial accuracy. Capture of these images

requires positioning a camera in difficult to reach places throughout the tunnel. To aid in positioning the camera, a Tunnel Inspection Assistant (TIA) was created specifically for the Grand Falls tunnel and incorporated associated photogrammetric features. It consists of a three-wheeled triangular frame and a boom used to rotate the camera a set radius around the center of the tunnel and can be seen in Figure 2.1. The TIA is manually maneuvered with one steerable wheel. The rotating boom is motor driven and pre-programmed to follow a set incremental routine. The process of scanning the tunnel involved positioning the TIA in the center of the tunnel, checking for level and alignment, capturing images through a planar rotation perpendicular to the tunnel axis, and incrementing along the tunnel a set distance to the next station to repeat the process. The initial capture of the 822 m concrete-lined section of Grand Falls took a total of seven days to complete. The result of the process was a 3D model of the tunnel with a spatial accuracy of approximately 5 mm and a ground sampling distance of 1.3 mm.

Figure 2.1: Model of TIA, capture rig used for Mactaquac and Grand Falls. [5]

The resulting model from Grand Falls (See Figure 2.2) proved to NB Power through

demonstration the concept and effectiveness of this photogrammetric inspection system. NB Power had also been monitoring the Mactaquac Generating Station (Mactaquac) with traditional methods. This station suffers from concrete expansion of the dam due to alkali aggregate reaction. The measurement precision required to assess the condition of this effect make Mactaquac an opportune area to further assess the abilities of the photogrammetric inspection system.

Figure 2.2: Example of resulting Grand Falls model, including a wireframe view on the left and textured model on the right. [5]

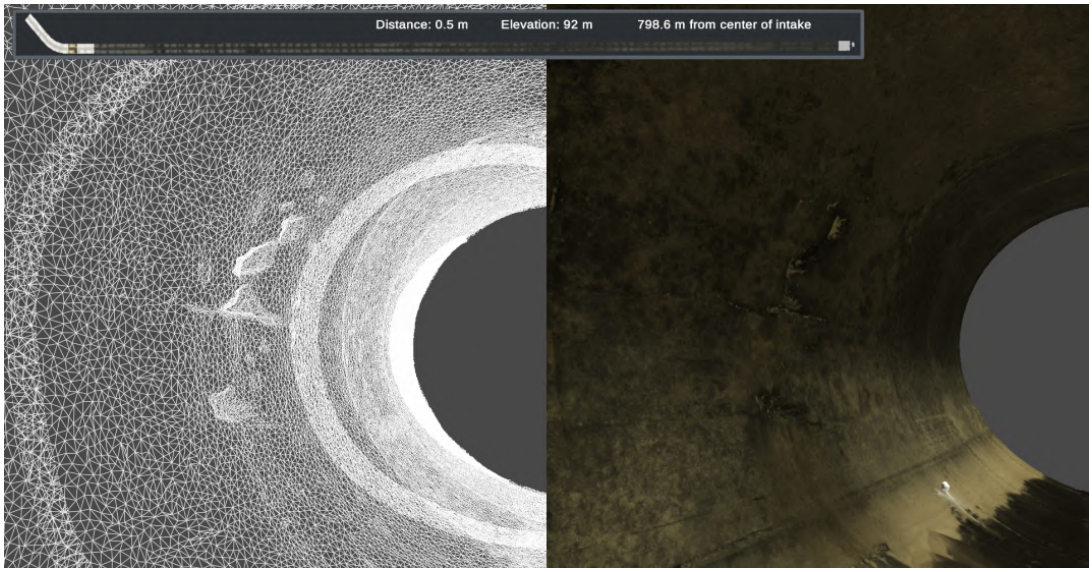

However, TIA was a one-off design made specifically for assisting with image capture of the Grand Falls intake tunnel and therefore a modified version of TIA was developed for the penstocks in Mactaquac [7]. Throughout this time, the inspection process developed by Bradley et al. [5, 6, 7], fueled the launch of Bradley Engineering Ltd. (BE) in 2018, a company which conducts these photogrammetric operations in New Brunswick. The extensive experience acquired by BE in performing these operations has led to the identification of additional opportunities for improvement in the previous image capture process. As experienced when moving from the Grand Falls tunnel to the Mactaquac penstock, the customized design for a specific tunnel's dimensions hinders the applicability of the capture system. The manual efforts

required to transport and utilize the TIA systems limit the speed of the data acquisition process. Study of this work led to the identification of the opportunity for a multipurpose automated data acquisition system that can adapt to various tunnel dimensions and configurations.

2.2 Motivation for Technological Innovation

The interest in exploring automated methods of data acquisition has grown as the abilities of technology and computers have been rapidly expanding. While the demand is growing generally across many industries, the reasoning for this piqued interest varies through different applications and environments. These unique influences have and continue to be motivating factors in the surge of automated inspection practices in today's world. Acknowledging the motivations of many is beneficial in placing this work in a larger context and identifying the following key factors that may have gone underappreciated.

2.2.1 Safety and Accessibility

It has been a common practice for routine infrastructure inspections to be conducted manually by a trained inspector or technician who must physically move throughout the target area and assess the state of the infrastructure. In a lot of environments, this is a significant safety concern as these areas are often dark, confined, elevated spaces, or contain potentially hazardous chemicals and equipment [36]. While safety precautions are implemented, the highest level of safety is achieved by removing the need for the inspector to enter the area at all; this is one of the most prevalent motivations for adapting to an automated process.

Stent et al. [46] were investigating a low-cost robotic system for efficient visual in-

spections of large utility tunnels. They noted the dark, dusty, and often hazardous tunnels as a significant health and safety risk to inspectors whose traditional inspection methods were based on manual walkthroughs of the tunnels. Lim et al. [28] found robot use to be an opportunity in the inspection of bridge decks where passing traffic was a constant concern for the inspectors. By implementing a self-navigating robot that could cover the same at-risk area that a regular manual inspection would, they could greatly reduce the safety risk of human inspectors. Hosotani and Yamamoto [22] stated the desire to alleviate the stress that these environments place on the laborers during inspections. Eschmann et al. [16] and Ellenberg et al. [15] concur that the safety and accessibility benefits of autonomous inspection systems are also driving factors in their research efforts. The ability to safely explore structures and areas that are complex, dangerous, or inaccessible by humans is of great demand. Comprehensive documentation of the tunnel status also allows for better planning of maintenance and therefor reduces the time workers are in the tunnel which improves their safety.

2.2.2 Financial Benefit

Along with the accessibility and safety of inspecting infrastructure, a financial element is commonly a defining factor in many decisions. Automation of the inspection practice addresses this concern with the ability to reduce the time and labor required to complete the inspection. Eschmann et al. [16] described the opportunity of autonomous inspections performed by an Unoccupied Aerial Vehicle (UAV) as an improvement to the timely and costly approach of human assigned inspections. Hosotani and Yamamoto [22] identified a need to reduce the amount of labor required to conduct small tunnel inspections.

2.2.3 Quality and Consistency

Although there can be advantages to having an expert in the tunnel completing the inspection firsthand, automated processes can streamline the inspection to produce more objective results. A distinctive element of inspections centered around humans is the inconsistency and prevalence of human error associated with them. Lim et al. [28] and Stent et al. [46] both agreed that the risk of human error at any point throughout the inspection process is common and a drawback of any manual steps in the process. The subjectivity of the individual or individuals completing the inspection can lead to discrepancies and misinterpretations of the inspection records. Ellenberg et al. [15] also identified the dependence on the experience of the inspector as a significant source of assessment variance. Maintaining a standard in the inspection process is critical for ensuring effective results, an obstacle for which technology supplies an improved solution.

2.3 Inspection Technologies

There are many types of inspections; one type is a visual inspection which can encapsulate a broad range of methods and technologies. With advancing photographic technology and image processing techniques, visual inspections are an opportune area for advancements in automation. The following subsections examine some of the current technologies and methods used to automate portions of the visual inspection process. After reviewing the factors that influence researchers to explore automation in the inspection field, it is apparent that the data acquisition process is the primary phase that demands automation.

2.3.1 Unoccupied Underwater Vehicles

Researchers and infrastructure owners have investigated means of improving the inspection process. Testing began on underwater robots several decades ago [21]. These robots avoid the need for draining a tunnel and are currently useful to identify significant structural movement, as noted in the exploration of utilizing an underwater Remotely Operated Vehicle (ROV) in the monitoring of a hydroelectric tunnel in [9, 1]. This was used in combination with a range of acoustic sensors for identifying potential deformations, cracks, or debris within the tunnel, which could then be further analyzed during the next dewatered manual inspection. While this demonstrates effective preliminary identification of potential areas of concern through spatial monitoring, the visual inspection and documentation is still done manually by an inspector during shutdowns. The quality of images collected underwater is significantly vulnerable to the underwater conditions [55], although recent studies have demonstrated effective photogrammetric results in various environments [47].

2.3.2 Unoccupied Aerial Vehicles

UAVs are being seen more frequently in exploration and inspection applications; acquiring high resolution data from a UAV is achievable under favorable circumstances. Pertaining to exterior infrastructure, Eschmann et al. [16] produced millimeter precision for 3D reconstruction and visual inspection with a Digital Single Lens Reflex (DSLR) attached to a large octocopter platform with various positioning sensors. Results are represented in an ultra-high resolution 2D reconstruction which can be mapped to accurate 3D models for full building reconstruction. Considering the outdoor environment with sufficient natural lighting, the need for onboard illumination is unnecessary. With exterior infrastructure, there are significantly fewer obstructions allowing for a larger aircraft capable of carrying a heavier payload.

These ideal environment characteristics are not applicable to the interior of hydroelectric infrastructure, making the use of a UAV system more challenging to obtain similar results.

Due to increased constraints and complexities, autonomous indoor use of UAV's has been limited. However, work from Özaslan et al. [42, 41, 40] has progressed towards automating the image capture process for visual inspections of penstocks and tunnels with a Micro Aerial Vehicle (MAV) with the goal of collecting stitched 360-degree panoramic images from incremental sections along the tunnel for 3D reconstruction. The initial system was based around a hex-rotor platform with four cameras directed evenly around the cross section of the tunnel, as shown in Figure 2.3. To account for the typical darkness of these types of tunnels, an arrangement of onboard LED was used to ensure effective image capture. While utilizing a complete onboard lighting system helps ensure consistent and sufficient lighting throughout the process, this does increase the space and weight requirements which can be a limiting factor in flight capabilities. With a loaded flight time of 10-15 minutes, the proposed system is limited in the size of infrastructure that can be captured quickly, a common drawback of UAV systems. The resulting panoramic images provide little to inspect due to the low-resolution VGA cameras with poor lighting, as well as the distortions resulting from stitching the images. The compact placement of the cameras also leads to interference from the MAV's rotors in the images. The underlying limitation of this type of system is the aerial vehicle's load capacity; this hinders the flight times and the ability to utilize larger, higher quality cameras and lighting systems.

An important aspect to consider when selecting a vehicle type for a specific application is the amount of controllability required. In general, UAVs have more agility and maneuverability than terrestrial vehicles. However, the additional Degree(s) of Freedom (DOF) associated with UAVs bring further complications to the positioning and navigation of these vehicles [42].

Figure 2.3: Micro Aerial Vehicle used in [42, 41, 40].

2.3.3 Terrestrial Vehicles

Ground based or terrestrial vehicles are more familiar and have been adapted to a larger range of applications than UAVs, making them an obvious option to implement automation in the inspection process. Comparatively, terrestrial vehicles have increased load capacity and a reduced complexity of maintaining stability and control under loads, however the terrain being traversed is an additional element not faced by UAV's. This aspect was a limiting factor in the work done by Hosotani and Yamamoto [22] who attempted to create a self-propelled image capturing robot to reduce effort in the inspection of free flow tunnels. The goal was to capture panoramic images of the wall surface from the center of the tunnel. It was designed with two front driven wheels with motion controlled by a Proportional-Integral-Derivative (PID) based feedback control, data from an ultrasonic sensor that monitors the distance to the wall, and a reed switch to monitor mileage through wheel rotations. Panoramic images are captured by an onboard hemispheric camera, while a VR camera also allows an inspector to wear a head-mounted display to visualize the environment in 3D. After testing in a 100 m tunnel, the image results were un-

satisfactory for current inspection standards as distortions and inconsistencies were present due to meandering and instability of the robot on the rough tunnel floor surface. Although conceptually this type of system has the potential to be an effective solution for many types of tunnel infrastructure, the design in its current state does not present itself as feasible for quality inspections without stability improvements. Expanding on the position sensing system to extract more data from the environment than a single ultrasonic sensor could make this design much more effective in the future.

A visual inspection for crack detection of concrete structures was trialed by Yu et al. [54] based on a small mobile robot. It used a differential drive configuration to maintain a constant distance from the wall, with an image capture system including a high-power illuminator, a shock absorbing device, velocity sensors, and a camera. The system could capture resolutions of 0.3 mm/pixel at 5 km/h, however the crack detection system experienced erroneous crack identification making it impractical in its current state. A similar mobile robot was used [52, 53] that included an array of ultrasonic sensors to detect deformations in tunnels. Though experiments of these systems were performed in multiple environments (indoor, road and subway tunnels) [52, 53, 54], they all had generally flat floor surfaces; the small frames of these mobile robots are likely unable to effectively move through the curved, rough and sloped terrain of many hydroelectric tunnels.

With the comparable goal of collecting high quality images around a tunnel, Stent et al. [46] explored a more stable and rigid approach to solving this task. As maintaining centricity within the tunnel is critical for consistent image data, the capture system was mounted to a monorail that runs the extent of the tunnel, see Figure 2.4. This is a much more effective approach to maintaining the camera position within the tunnel but significantly limits the areas in which it can be utilized. The capture process involves two high quality DSLR cameras that rotate around the center of the

tunnel. The system enables the option of having each camera capturing a 180-degree half of the tunnel or the ability for each camera to capture the complete tunnel at different resolutions. This selective option addresses one of the important elements of influence identified as it increases the speed of a standard capture and can also remove the redundancy of image capture if multiple resolutions are required. The result of the inspection is a highly detailed 3D reconstruction of the tunnel with a list of tunnel positions with cracks identified. The high level of detail produced allows for sub-0.3 mm cracks to be identified, which is a resolution that is not attained by many systems in this environment.

Figure 2.4: Monorail-based visual inspection system [46].

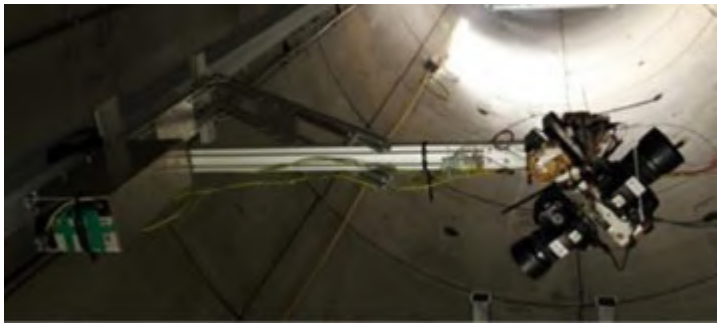

A crawler teleoperation robot system was implemented in [48] to perform a range of image and video collection within diversion tunnels. Using convolution neural networks, locations of seepages and repair defects could be classified. While the inspection covered the entirety of the tunnel surfaces, data acquisition occurred at 5 m intervals, where each interval took 5 hours to complete; in tunnels potentially kilometers long where downtime is expensive, this rate of acquisition is not feasible for many dam applications. A crawler type robot was also the foundation of the autonomous inspection system developed by Kamiyama [24], in which construction site embankments were inspected. The crawler robot was able to climb slopes of 45 degrees and surmount walls upwards of 450 mm, demonstrating the capabilities and maneuverability benefits of crawler technology for this application.

Standard images and model reconstructions are an effective and versatile approach to assessing the visual condition of infrastructure. However, this can be advanced to examining non-visual elements such as temperature properties by utilizing a thermal camera. Borrmann et al. [4] developed a fully automated system to create a 3D thermal model of indoor environments. By merging the information provided by a 3D laser scanner, an RGB camera, and a thermal camera, a complete 3D point cloud model can be constructed with thermal and color properties. Mounting this on a self-exploring vehicle allows a complete indoor environment to be explored autonomously. This system and technology demonstrate the advantages and ability to incorporate different types of data, such as thermographs, into the visual inspection process.

2.4 Navigation and Positioning

Many different localization and navigation methods are available and have been reviewed. In general, there are two main forms, referred to as relative and absolute localization. Relative localization is the more common type and refers to identifying the position in relation to a known origin, whereas absolute localization uses features from the surrounding environment to estimate a vehicle's pose and location [17]. Each has its own advantages and disadvantages regarding the applicability to various environments. The collection of options leads to the question of what method, or combination of methods are best suited to handle the task at hand. Answering this question requires consideration of the specific limitations of the target environment and the expected level of information required to effectively control the vehicle to the level desired. The following section will explore some of the methods and technologies used for localization or navigation and compare the performance and applicability of each.

2.4.1 Relative Localization

Visual odometry is an alternative form of odometry compared to more common methods, such as wheel encoders or Inertial Measurement Unit (IMU). Using a visual-based approach, Patruno et al. [43] have been able to determine the relative pose of an omnidirectional Automatic Guided Vehicle (AGV) in an indoor environment. They've implemented this as a simple system with a single monocular camera directed perpendicular to the ground; the captured images are used to monitor the planar translation and rotation of the robot. Using feature-detection based image analysis techniques such as the Speeded-Up Robust Features descriptor, the relationship between key points in consecutive images can be correlated and used to determine the displacement between captures. Cumulatively tracking this process can localize a vehicle's position and orientation from a known reference. The accuracy and reliability of this method are strongly dependent on the consistency of lighting between images surface textures and accuracy of the feature matching algorithm used. The system underwent multiple tests. Tests of an average distance of 17.2 m and a longer test of 80 m were completed which resulted in a final positioning error of 0.21% and 0.94% respectively. The average relative positioning error was found at approximately 3% which is comparable to the industry standards. The need for a textured and consistent surface is a limitation to the areas where this can be applied; flowing water or debris within a hydroelectric tunnel could cause inconsistencies in the results, particularly at the tunnel invert.

Nourani-Vantani et al. [39] explored a less computationally intensive approach to visual odometry on car-like vehicles in an outdoor environment. Using a similar camera set up and template matching as opposed to feature detection, this simplified approach was able to achieve position errors below 4% for distances up to 100m, considerably better than wheel-based odometry. A significant consideration for con-

sistent results was identified as the need for uniform and consistent lighting within the images.

This type of odometry was also used within the work done by Özaslan et al. [42, 41] described earlier. The most significant contribution of this work was the localization of the MAV within a dark and featureless environment. With a low-resolution (5 cm) 3D occupancy grid of the tunnel available, the MAV was equipped with two lidar sensors which provide an estimate of the vertical and lateral coordinates of the robot. These sensors in combination with the onboard IMU can also estimate the three DOF orientation of the MAV. However, the lack of distinct features in a penstock makes determining the position along the tunnel difficult for a lot of common measurement technologies. Therefore, this final DOF is obtained with the use of visual odometry and optical flow, similarly described in Patruno's [43] work. Images captured from the MAV identified salient features on the tunnel walls which were used to determine incremental estimations of the MAV's displacement between frames. In testing, this system was able to maintain a positioning error of less than 2.5% due to drift. Improvements were made to the system [40] to replace the two lidar sensors with a single 3D lidar sensor capable of estimating the five DOF pose along the tunnel's center axis, fitting the data to a segment of the grid map. This system and algorithm could align the drone in the center of the 5.5 m tunnel within a 5% error.

In the approaches discussed previously, the visual odometry was based on details within the surface of the structure. Alternatively, features within the environment are also able to provide similar information. Using machine vision techniques, displacements between successive image captures can be estimated by comparing key point coordinates from target objects within the environment. Lins et al. discusses this type of system in [31, 32] which was able to monitor robot velocities with an uncertainty of +/- 1.74%. In common with other visual based approaches, uncertainty

and inconsistencies can present themselves due to image quality and illumination properties within the environment. Tests of this method were shown to provide results 45% faster while demanding 14% less computational resources as compared to the optical flow approach. A requirement of this system is that the environment must have sufficient lighting throughout to ensure effective and consistent feature detection within the image. Practical application of this system has been demonstrated in further work from Lins et al. [30, 29] in combination with crack inspection methods.

2.4.2 Absolute Localization

A form of absolute localization can be implemented using a variety of triangulation approaches. These methods utilize beaconing technology to measure the distance between the robot and a set of beacons whose locations are identified within the environment. This can provide an estimate of the robot position at any point in time. One approach has been proposed by Shi et al. [45] who have taken a minimized cost approach to implementing a high accuracy solution to indoor AGV localization. They proposed the use of Ultra-Wide Band (UWB) technology in which a receiver on the vehicle and at least three transmitters placed strategically within the environment can triangulate the location in the environment. This was designed for a planar scenario simplifying the approach to a 2D localization solution. A gradient decent method in cooperation with a least square method are used to process the data to determine the optimal localization estimation. The UWB technology on its own is effective in determining the 2D position of the vehicle but is unable to determine to the pose of the vehicle itself. The UWB system was tested against a real-time kinematic system that has a precision of 2 cm. The test results showed an average localization error of 20 cm with a peak error of 40 cm, with the error being minimal

in the central region of the transmitters. The need to have the transmitters spaced tens of meters apart and ideally in an equilateral triangular shape centered around the general position of the receiver makes this method more challenging in the more confined environments of hydroelectric infrastructure.

An aspect of autonomous robot navigation that has not been as thoroughly explored is the consideration of sloping or unstructured areas, defined generally as areas without complete knowledge of the surroundings [25]. Rosas-Cervantes et al. [44] have investigated a robot navigation system for uneven and unstructured indoor environments. Utilizing a combination of wheel odometry, an IMU sensor, and a 3D lidar sensor, their proposed system builds a 3D map and performs 3D simultaneous localization and mapping. Laser scan data was used to identify local horizontal distances and 2D features to create an occupancy map of the environment, that is, a discretized grid identifying the presence of obstacles in the environment. The adaptive Monte Carlo localization algorithm used this information to allow the robot to determine its global position (2D) as it moved to the local goal. The IMU provided robot orientation and speed information. The 3D lidar information provided the benefit of identifying slopes and other features that are neglected from 2D information such as openings in the floor, ground obstacles and the overhead clearance in areas. The approach was tested against a generalized iterative closest point and lidar/odometry mapping. This proposed method had significantly lower localization error, peaking at 0.15 m as opposed to 0.54 m and 1.23 m from the other methods respectively, without a considerable increase in time to completion. The ability to identify obstacles and terrain changes in a 3D space provides a significant benefit over other systems which are limited to a 2D view.

2.5 Model Predictive Control Implementations

Research into the application and implementation of Model Predictive Control (MPC) and other advanced control techniques has been greatly expanding in the past few years with the number of papers growing. However, MPC has not been commonly found in robotic systems of the scale or application that is covered in this work. The demonstration of an MPC methodology for defining energy-efficient and agile controls for a Mecanum-wheeled robot navigating among various environments and obstacles is explored by Moreno-Caireta et al. [37]. The robot's equation of motion, electrodynamic and frictional effects formulate the dynamic model. Additional elements included in the controller include the respective motor voltage limits, avoidance of collisions with obstacles, and attempts to minimize energy consumption. Simulations in free movement, narrow corridors, and moving obstacle avoidance scenarios show how this methodology can account for nonlinear dynamics and the saturation of actuators along with inconsistent environments [37]. MPC was a critical element in the two-dimensional translation and one-dimensional rotation of a multi-legged robot. Hybrid control is based on MPC and sliding mode control at the body level which defines the kinematic relationship between the body's stride length, relative and absolute pose. The MPC-based control incorporates stride constraints which relate to the mechanical structure and component dimensions [18].

Adaptive nonlinear Model Predictive Control (nMPC) and variations of this control including a novel simplified nMPC and a PID based nMPC has been demonstrated on a two-link vertical robot manipulator [49]. Both theoretical simulations and experimental results show the effectiveness of these control techniques. The closest closed-loop control was provided by nMPC while the simplified version invoked the smoothest response [49]. Additional examples of the current research and applications of MPC can be seen in [20, 27, 50, 51]

Chapter 3

Methodology and Theory

3.1 Research Methodology

Attaining the goal outlined in this work is a challenge that encompasses several multidisciplinary fields. This section details the general methodology used for completion of the required objectives. It has been generally divided into three sections corresponding to the high level tasks required: formulation and design, construction and assembly, and overall testing.

3.1.1 Formulation and Design

With the functionality and motion requirements thoroughly defined, Computer Aided Design (CAD) software was used for a visual design comparison and consideration of several Automated Tunnel Inspector (ATI) design concepts. The final selection was made for stability, compactness, ease of assembly, weight optimization, maneuverability, and effective image capture abilities. Detailed structural and assembly design were then conducted using CAD software. Applying principles of mechan-

ics and machine design, robot kinematics and dynamics, vehicle theory and other general engineering principles as outlined further in this chapter were key aspects of understanding and finalizing the design.

A key element to the development of the ATI design has been the simulations that are driven by the formulation of the theoretical physics-based model. The ATI system is complex and the use of MapleSim™ [34] software has greatly enhanced the accuracy of the derived models and its simulation. The initial simulations were able to determine and illustrate the 3D kinematic motions of each degree of freedom and joint. This visualization was crucial in examining the ATI's spatial motion for challenges associated with the tunnel curvature and variabilities along the path. Further simulations were able to provide significantly more data and information about the dynamic relationships between each joint and driving actuator throughout several Ranges of Motion (ROM) and actions. Chapter 5 discusses the procedure and results from these simulations and analysis.

With simulations of the physical model being executed, control strategies were formulated to define the controller parameters of each driven joint. The ATI has multiple actuated joints relying on several inputs, some of which are independent while others are not and can occur simultaneously. This defines the ATI as a multi-variable or Multiple-Input-Multiple-Output (MIMO) system, however for simplicity, the control strategy was represented as a set of Single-Input-Single-Output (SISO) systems. The controller was developed and tested in simulation using a combination of MapleSim™ and MATLAB® [35].

3.1.2 Construction and Assembly

With a fully designed system, procurement and construction of the structural framework and specific actuation components could begin. The major fabrication of the

structural assemblies has been contracted out to specialized fabricators and machinists based on the manufacturing documents developed throughout the design process. Simultaneously, the procurement of actuation and automation components such as motors, bearings, sensors, and the complete range of components was completed in coordination with various suppliers.

As the electro-mechanical components arrived, they have been individually tested in the lab environment to ensure proper functionality and give insight into the controller integration requirements. Confirmation of functional components led to the integration of subsystems and the implementation of corresponding automation routines to have proper and smooth operation. Development of a foundational user interface was implemented to manage all individual and combined components, allowing for tests of the user's input targets, along with fundamental start/stop functions and other safety considerations.

3.1.3 Testing

The component testing was a sequential process beginning with open-loop tests of components followed by the inclusion of feedback in closed-loop tests. This was expanded from single components, to subassemblies of components, before finally being completed on the entire system. This process identified the need for any adjustments to the structure or connections, and the incremental approach streamlined the problem identification and troubleshooting process. This conservative and thorough approach to control system development and integration with the electro-mechanical components helped limit the risk of undesirable large transients in the closed loop dynamic response when the controller integration on the complete ATI was tested.

With the individual systems being fully formulated and tested in a lab environ-

ment, the next phase moved into field tests to determine various performance factors in real-world environments. These tests were used to validate the system's mobility, functionality, and mechanical stability on comparable terrain such as a rough pavement. A conservative approach was taken when setting the test velocity and acceleration profiles for instructing the ATI to execute various operations, actions, and maneuvers. A cyclical and gradual increase of the setpoint profiles was used to assess the performance and data collected. This phase of the process was critical in identifying and addressing minor issues in the system's operations that needed adjustment before being implemented in a real tunnel environment. Following the ATI's implementation in Grand Falls Generating Station (Grand Falls), further testing was conducted to collect additional closed loop data for better representation and presentation of system performance.

3.2 Robotics Theory

Robotic systems are seen in a wide range of applications and industries varying greatly in size, power, and abilities resulting in many uniquely appearing systems. Mechanical manipulators of robotic systems are described as either a serial or parallel manipulator depending on their configuration. Serial manipulators are the most common in industry and are defined as a set of links and joints connected in series that provide relative motion of adjacent links. This type of manipulator applies to aspects of the system outlined in this project, and the general principles of kinematics and dynamics for this manipulator are defined within this section.

3.2.1 Serial Manipulator: Spatial Relation

The kinematics and dynamics of n-DOF serial manipulators have been studied extensively for adaptation into the system selected for manipulating the camera position. The spatial description of the system can be defined using the homogeneous transformation matrices (${}^{n}_{n+1}T$) as shown in Equation 3.1, defining the position and orientation of successive joints based on the modified-Denavit-Hartenberg (mDH) convention as defined in [12], where x_n, y_n, z_n are unit vectors describing the frame axes of joint n and combined to create the rotation matrix expressing frame n+1 to frame n. Additionally, ${}^{n}p_{n+1_{orig}}$ depicts the location of the origin of *n+1* relative to n, broken down into vectors ${}^{n}p_i$.

$$
{}^{n}_{n+1}T = \left[\begin{array}{ccc|c} x_{n+1}\cdot x_n & y_{n+1}\cdot x_n & z_{n+1}\cdot x_n & {}^{n}p_x \\ x_{n+1}\cdot y_n & y_{n+1}\cdot y_n & z_{n+1}\cdot y_n & {}^{n}p_y \\ x_{n+1}\cdot z_n & y_{n+1}\cdot z_n & z_{n+1}\cdot z_n & {}^{n}p_z \\ \hline 0 & 0 & 0 & 1 \end{array}\right] = \left[\begin{array}{ccc|c} & ({}^{n}_{n+1}R) & & {}^{n}p_{n+1_{orig}} \\ \hline 0 & 0 & 0 & 1 \end{array}\right] \tag{3.1}
$$

Compounding these transformations through n joints relates the pose of the camera on the ATI to the base as follows in Equation 3.2.

$$
T^{base}_{cam} = {}^{base}_{1}T * {}^{1}_{2}T * \cdots * {}^{n-1}_{n}T * {}^{n}_{cam}T \tag{3.2}
$$

3.2.2 Serial Manipulator: Kinematics and Dynamics

The outlined spatial description is used in the derivation of the Jacobian matrix (J, 6 x n) of the manipulator, which defines the relationship between the camera velocity

(ν, 6 x 1) and the joint velocities ($\dot{\Theta}$, n x 1) as follows (3.3):

$$\nu = J * \dot{\Theta} \tag{3.3}$$

Furthering the analysis to include the mass and inertia of the system members, along with the frictional effects on moving joints and surfaces, the torques and forces can be evaluated. By defining desired motion profiles of the driving joints, dynamic responses of the joints can be analyzed throughout the defined trajectory. MapleSim™ can be used to demonstrate the 3D motion and analyze the dynamic response more thoroughly. The general dynamic equations for an n-DOF manipulator as derived from the Newton-Euler equations [12] is represented in Equation 3.4.

$$\tau = M(\Theta)\ddot{\Theta} + V(\Theta, \dot{\Theta}) + G(\Theta) + F(\Theta, \dot{\Theta}) \tag{3.4}$$

Here τ is the n x 1 vector of joint forces/torques, $M(\Theta)$ is the n x n mass/inertia matrix, $V(\Theta, \dot{\Theta})$ is an n x 1 vector collecting centrifugal and Coriolis terms, $G(\Theta)$ is an n x 1 vector of gravity terms, $F(\Theta, \dot{\Theta})$ is the inclusion of viscous and Coulomb friction effects. Θ depicts the position of each joint, with $\dot{\Theta}$ and $\ddot{\Theta}$ being the first and second derivatives respectively.

3.3 Vehicle Dynamics Theory

Traditional vehicles are immensely complex systems integrating many mechanical and electrical components while interacting with the ever-evolving dynamic environment. The mobile robotic system that is being explored in this project may not resemble a typical road vehicle, but the generic electro-mechanical principles remain applicable, nonetheless. Understanding the fundamental operation and stability of

such system demands knowledge and study of the theories and mathematics behind dynamic vehicles, which are detailed and presented in the following section.

3.3.1 Dynamic Model of Vehicle Motion

As the system discussed within this project is not a traditional vehicle, being limited in speed, application, and complexity; a simplified, one-dimensional description of vehicle dynamics will be discussed and applied for this portion of the work. A vehicle's motion can be understood by analyzing the power and forces exerted against the external forces applied onto the vehicle, which can be dynamically modelled as shown in Equation 3.5 based on Figure 3.1.

Figure 3.1: Dynamic model of a vehicle moving up a sloped surface. [14]

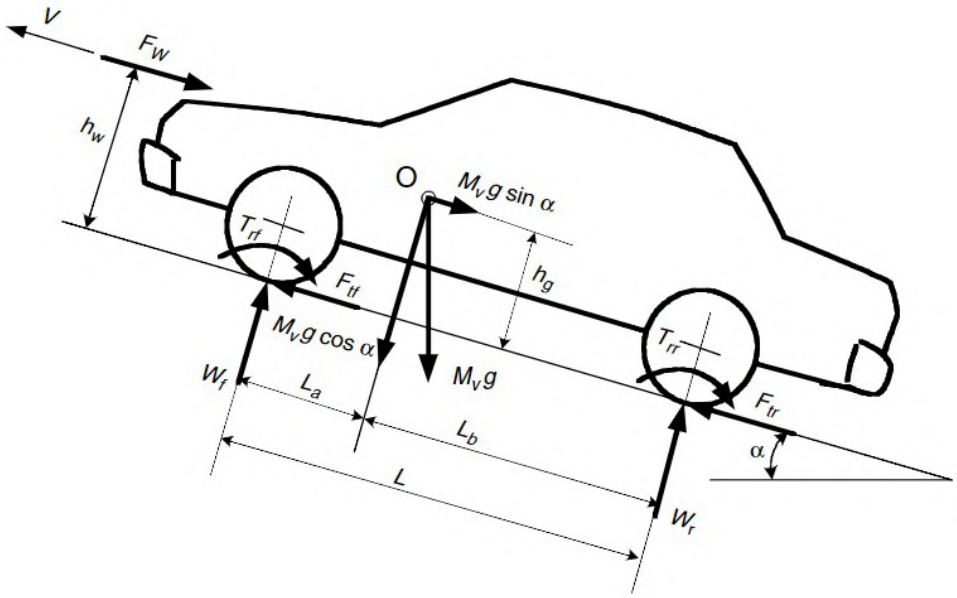

$$M_v \frac{dV}{dt} = \sum F_{Tractive} - \sum F_{Resistive} = (F_{tf} - F_{tr}) - (F_{rf} + F_{rr} + F_D + F_g) \quad (3.5)$$

The element M_v is the total mass of the vehicle, $\frac{dV}{dt}$ is the linear velocity, or rate of change of the vehicle's velocity, $F_{Tractive}$ is the net tractive effort provided by the

wheels of the vehicle, which includes the efforts of both the front (F_{tf}) and rear (F_{tr}) wheels. The total resistive force ($F_{Resistive}$) experienced by the vehicle incorporates rolling resistance of each wheel (F_{rf}) and (F_{rr}), aerodynamic drag resistance (F_D), and grade resistance (F_g) [14]. As the system developed in this project operates in a confined indoor space, at very low speeds, with a skeletal structure, the effect of aerodynamic drag can be ignored for this analysis.

3.3.2 Rolling Resistance

Figure 3.2: Representation of the effect of rolling resistance. [14]

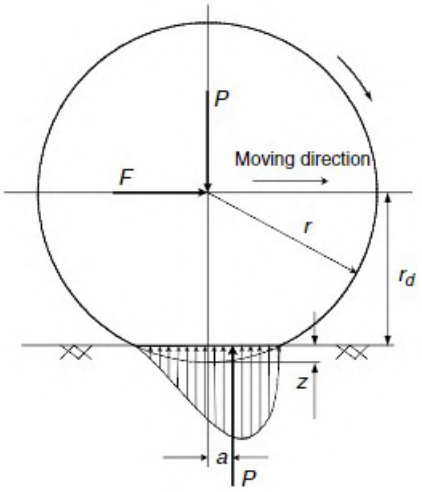

Rolling resistance is a factor of the ground reaction force causing a resistive force on the rotation of the tires due to the deflection of the tire. It varies depending on the type of tire and material, tire pressure, and type of surface being driven on. The tire deflection causes the ground force to shift towards the leading edge of the tire, imposing an eccentric load on the tire and therefore creating a counter moment on the tire as seen in Figure 3.2. This resistive moment (T_r) on the tire is calculated in Equation 3.6 and must be applied to each tire in contact with the surface [14]. The impact that this has on the overall motion of the vehicle can be represented as a force (F_r) directed opposite the direction of vehicle motion as calculated in Equation

3.7. The variable P is the normal load on the tire, r_d is the effective tire radius, f_r is the coefficient of rolling resistance as a function of the tire and surface properties and can be approximated by Equation 3.8 for most common applications.

$$T_r = Pa \tag{3.6}$$

$$F_r = \frac{T_r}{r_d} = Pf_r cos\alpha \tag{3.7}$$

$$f_r = 0.01(1 + \frac{V}{100}) \tag{3.8}$$

3.3.3 Grade Resistance

When moving along sloped surfaces the mass of the vehicle imposes a force acting downward in correlation with the force of gravity. While ascending a slope this acts against the vehicle motion, referred to as grade resistance, whereas it acts as a supporting force on motion while descending a slope; however, for analysing the functional ability and performance of a vehicle, this aspect will be neglected as this scenario demands significantly less effort from the driving system as compared to the upward slope case. Equation 3.9 depicts this component relating the vehicle mass (M_v), gravitational acceleration (g), and the slope angle of the surface being climbed (α) [14].

$$F_g = M_v g sin\alpha \tag{3.9}$$

3.3.4 Maximum Tractive Effort

Determining the minimum tractive effort required to properly operate the vehicle and overcome the resistive efforts have been detailed above, and subsequently the

following details the upper limit of the tractive efforts to avoid slipping during operation. The maximum tractive effort (W_i) is defined in Equations 3.10 and 3.11 giving the maximum tractive effort that can be applied while maintaining traction. Any additional force beyond this limit will result in the tire beginning to slip on the surface. The calculation of this varies based on the drive system (front-wheel drive or rear wheel drive) [14].

$$W_i = \frac{L_i}{L} M_v g cos\alpha \pm \frac{h_g}{L}[F_t - F_r(1 - \frac{r_d}{h_g})] \tag{3.10}$$

$$F_{tmax} = \mu W_i \tag{3.11}$$

The variable L is the distance between the front and rear axle, L_i is the horizontal distance between the center of gravity and the applicable axle, h_g is the height of the center of gravity, μ is the coefficient of road adhesion between the tire and surface, and W_i is the effective normal load on the corresponding axle.

3.4 Controls Theory

A significant aspect of this project is effectively and accurately controlling the velocity and displacement of various motors and linear actuator. This section details the control theories that have been implemented throughout the control of the overall robotic system. It combines simple control schemes with more advanced model predictive schemes for efficient control of independent subsystems of the ATI's various actuated joints.

3.4.1 Proportion-Integral-Derivative Control

The Proportional-Integral-Derivative (PID) controller, and derivatives of it, (P,PD,PI) are fundamental closed-loop feedback control methods. Each element of the PID controller contributes to improving the overall response of the system. Figure 3.3 demonstrates the general block diagram and transfer function of each element of the PID control [2, 33].

Figure 3.3: Block Diagram of general PID system. [11]

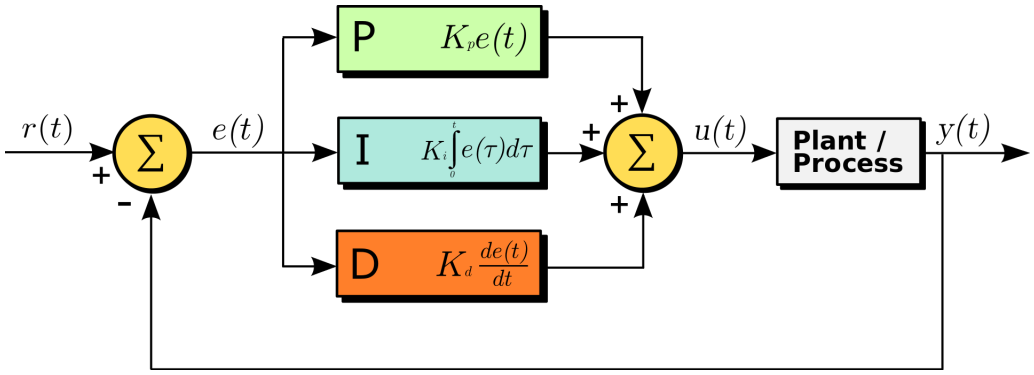

Proportional control applies a gain constant that is proportional to the current error of the system. This proportional gain constant (K_p) is multiplied by the error to adjust the response [2, 38, 33]. This control method alone is limited as the response never truly reaches the exact steady state value (within a tolerance) of the plant.

Integral control accounts for the accumulation of error over time and adjusts the rate at which the response moves towards the setpoint. The integral gain constant (K_i) is multiplied by the accumulated error and added to the output of the controller [2]. This overcomes the lingering steady-state error that is seen with solely proportional control, however, introduces the risk of overshooting the setpoint [38].

Derivative control multiplies the rate at which the response error is changing with the derivative gain constant (K_d). This element uses the error change rate to predict the behavior of the system and improve the settling time and stability of the system[2, 38].

Different combinations of these elements are used to improve different aspects of the response; a PI controller improves the steady-state error, increasing the system type and drive the response error to zero. Alternatively, the PD controller improves the transient response by feeding the error, and the derivative of the error to the plant to create a very fast response at the cost of additional noise risk [38]. The complete PID controller encapsulates all aspects to improve both the transient response and steady-state error. The PID controller's simple implementation and versatile application make these controllers one of the most common control methods used in industry.

3.4.2 Model Predictive Control

Model Predictive Control (MPC) is an advanced method for optimizing the control actions of a system by minimizing the response errors. Unlike the previously described PID method, the MPC method considers more than just the previous response and error values; MPC makes model-derived predictions of the system response to better adjust the control action (u) for current and future time steps. It does this based on the concept of minimizing an objective cost function (J) which primarily includes the tracking of the response error [20, 13]. Additional elements may be added into the cost function to consider variation of the nominal control variables, and violation of applied constraints [26, 20]. Figure 3.4 displays the flow of the general MPC architecture, illustrating a multivariable system.

The MPC architecture works on the premise of the creation of a dynamic matrix (A), with dimensions P x n_u as can be seen in Equation 3.12, equivalent to the prediction horizon (P) and the control horizon (n_u). The prediction horizon is determined through collecting the open loop response from the system model reacting to a step input and is the number of discrete time steps required for the response to reach within 95% of the steady state value. Analytical approaches can also be used. The

Figure 3.4: General MPC architecture [20]

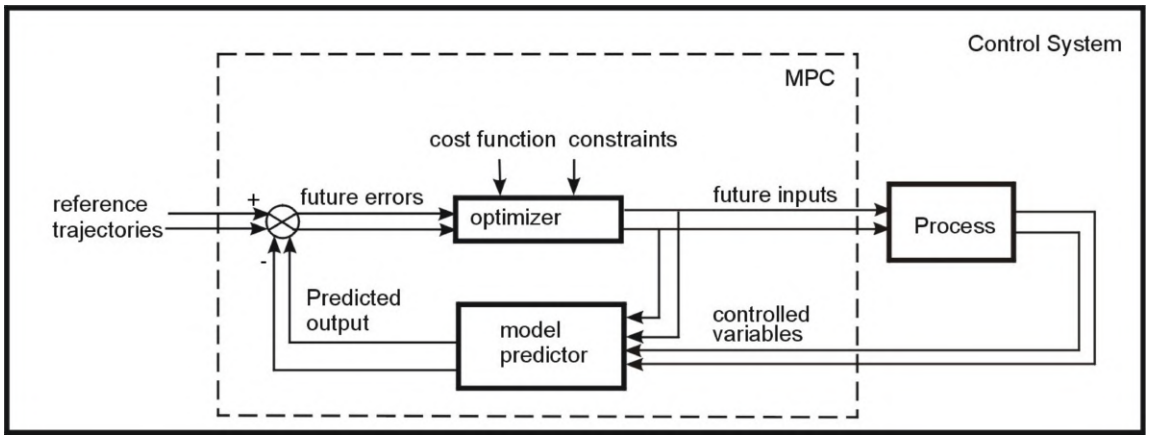

dynamic matrix is then filled with the corresponding open-loop response values (a_i) at discrete time steps up to the prediction horizon. The control horizon represents the number of future control actions being considered in the evaluation [20, 49].

$$A = \begin{bmatrix} a_1 & 0 & \cdots & 0 \\ a_2 & a_1 & \cdots & 0 \\ \vdots & \vdots & \ddots & \vdots \\ a_P & a_{P-1} & \cdots & a_{P-n_u} \end{bmatrix} \tag{3.12}$$

The cost function in Equation 3.13 represents the function used to optimize the control action, including the addition of a move suppression factor λ applied to the control action used to ensure a non-singular solution.

$$J = \sum_{i=1}^{P} (\hat{Y}_{t+i} - R_{t+i})^2 + \sum_{i=1}^{n_u} \lambda(\Delta U_{t+i-1}) \tag{3.13}$$

The variable $\hat{Y}_{t+i}$ is the prediction vector produced from the system model and dynamic matrix, R_{t+1} is the reference trajectory, both being considered i time steps ahead of the current time step (t).

The least squared method is used to optimize the cost function and determine the control action as shown in Equation 3.14, with the current predicted error vector ($\vec{E}$) of the system in relation to the reference trajectory vector ($\vec{R}$) noted in Equation 3.15.

$$\Delta U = (A^T A + \lambda I)^{-1} A^T E \tag{3.14}$$

$$\vec{E} = \vec{R} - \hat{Y} \tag{3.15}$$

The predicted response of the subsequent time step is then calculated as in Equation 3.16 using ΔU and a correction factor (ϕ_m) adjusting for the variance between the prediction of the model and the actual measured value of the plant output (y_m), as seen in Equation 3.17.

$$\hat{y}_t = \hat{y}_{t-1} + A\Delta U + \phi_m \tag{3.16}$$

$$\phi_t = y_{meas} - \hat{y}_{t-1} \tag{3.17}$$

The MPC provides a robust feedback control technique for controlling SISO and MIMO systems that are highly coupled and subject to unique constraints of the systems. It is traditionally not as frequently used in industry when compared to the PID, due to the increased computational efforts required, the unfamiliarity and additional theoretical knowledge required, and the barrier to adopting a technological change on a mass scale [26, 49]. Extensive details on MPC can be found in [26].

Chapter 4

Conceptualization and Design

4.1 Design Considerations and Criteria

The process of conceptualizing a set of potential designs first involved developing a concrete understanding of the fundamental requirements of the camera positioning system. In this case, this refers primarily to the system's ability to collect the required images for the purpose of an inspection. In detail, this includes:

- Maneuvering the camera throughout the cylindrical grid of image capture locations.
  - The two-dimensional planar circular path around the tunnel axis and the rotation required to remain perpendicular to the surface.
  - The advance along the tunnel length.
  - The orientational control of each camera.
- Transporitng the system into the tunnel through a 0.7 m porthole and being ferried through any path to the access location.
- Maneuvering the photography equipment safely and stably, while avoiding motion blur caused by shaking and instabilities.

- Fabricating the system in a reasonable time frame and budget.

Expanding on the fundamental requirements to consider factors that would lead to a more optimal design provides differentiating elements of the design selection process. Some factors that extend beyond the fundamental application of the system include:

- The level and ease of adaptability:
  - While each concept can have the fundamental ability to adapt to different tunnel diameters, a concept that can do so with ease, or has more extensive control over its position makes a more attractive solution.
- The simplicity of assembly/disassembly in the tunnel:
  - As the system is likely to be disassembled for transportation and access into the tunnel, being able to assemble the system within the tunnel with limited tools and in a reasonable time frame is important to the optimization of the entire data acquisition process time.
- The weight
  - Weight of the total assembly and individual component/sub-assembly weight impacts the manual efforts for transportation.
- The ease of manufacturing:
  - A system that can be fabricated in a local environment with limited use of specialized equipment or technicians simplifies the process.
- The accessibility and availability of the required equipment, products, and materials:
  - Easily obtainable products and equipment can be crucial for the fabrication process as lead times can often be a limiting factor in a project's timeline. This also applies in the event of a product's malfunction and need for repair or replacement parts.
- The complexity of control and operation, including hardware and software aspects:

– The control scheme can be complicated by redundancies in the control of the degrees of freedom. The need for synchronization of equipment can also increase control complexity and introduce the need for higher precision equipment.

4.2 Concepts Considered

Some key aspects that are considered in all concepts that provide the foundation for capture or are common improvements over the Tunnel Inspection Assistant (TIA) functionality include the ability to vary the elevation of the arm, adjust the rotating arm length to accommodate different tunnel diameters, incorporate control over the camera orientation, utilize a driven and steerable base, and include a second set of photography equipment to increase efficiency. The methods of achieving these elements vary throughout each design, the following section details some of the concepts that have been considered.

4.2.1 Cantilever Concept

The first design concept was derived as an expansion of the TIA, the original image collection system, that would incorporate an extensive amount of additional adaptability that the TIA did not have. A rotational arm with cameras cantilevered from each end to provide the rotation and frontal offset required for capture remains the primary element, while a linearly actuated adjustment of the arms length provides the camera radius adaptability. Elevating this arm from a vertical mast, as opposed to a rigid frame, provides the adaptability for reaching the center of different tunnels, as well as providing easier access to the camera equipment. One actuation for each degree of freedom, along with the decoupled relationship between the elevation

and rotation of the arm creates an uncomplicated method for providing the motions required. Figure 4.1 below details and illustrates this concept.

This simplistic concept comes with a noticeably front loaded and frail skeleton causing concerns of overall stability. Specifically, the frontal cantilevered load that the cameras apply to the arm suggests a need for heavy duty arm framework to counter the torsional impact. This adds to the already concerning overbearing forward moment created by the general configuration.

Figure 4.1: Cantilever Concept

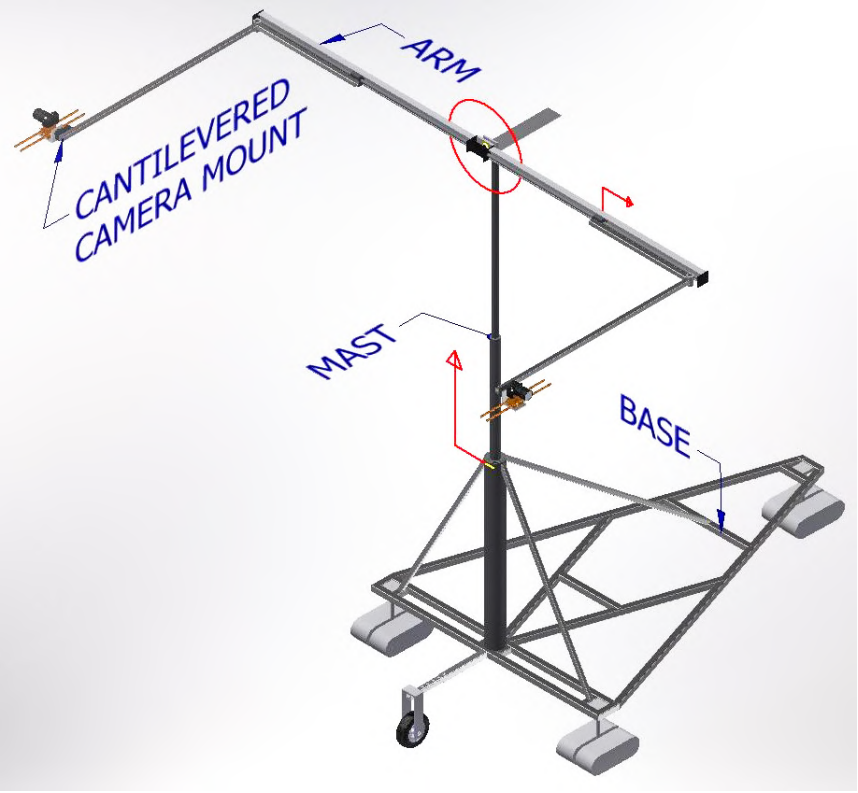

4.2.2 Double-Mast Concept

With the idea of balance and stability in mind, an alternative mast design was conceptualized utilizing two synchronized vertical masts to provide the elevating action required, see Figure 4.2 for a visual of this concept. A cross-member linking the two

masts lengthwise along the tunnel, and a rotational bidirectional arm attached to the center of this cross-member holds the pair of cameras at a variable offset from the tunnel axis. Centering the arm between two masts counters the frontal moment concern that was presented in the Cantilever concept. The symmetrical design also allows for identical operation in either direction with similar base frames on either end. Operation in a curved tunnel posed a concern for stability and contortion as significant alignment is required for the separated yet synchronized masts and quad-wheel base. Misalignment of the base ends about the curved surface, which can occur if either of the base ends shift to a different clock location about the tunnel than the other, and could invoke twisting of the cross-member, a detriment to the stability of the system.

Figure 4.2: Double-Mast Concept

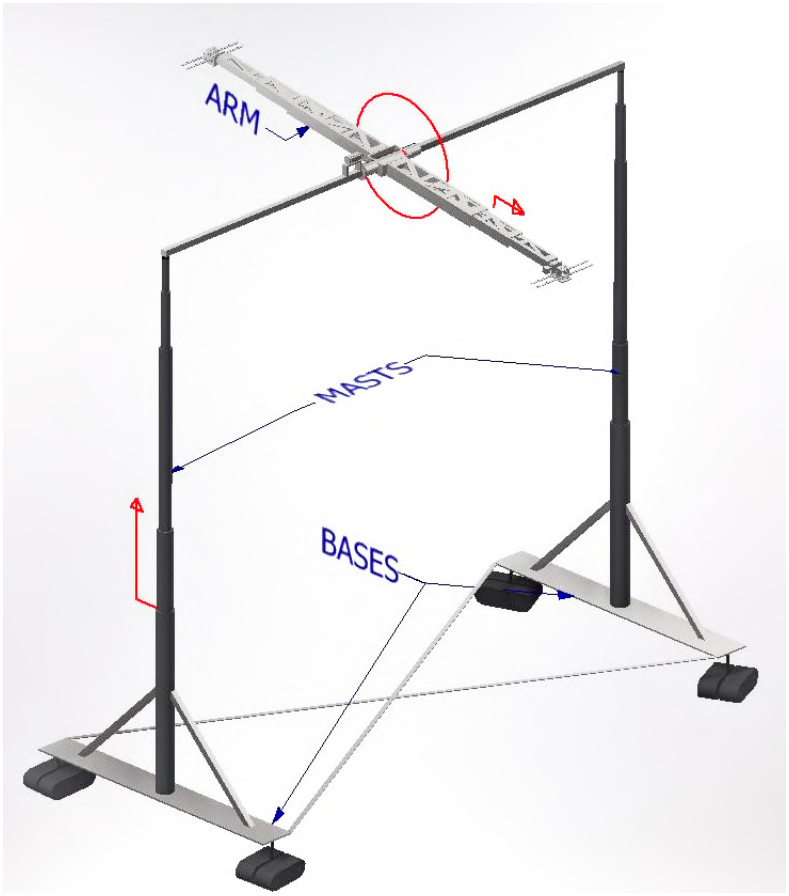

4.2.3 Stewart Platform Concept

Following the symmetrical concept, a more three-dimensional balanced system influenced by the concept of the common Stewart mechanism [3] was considered. This concept has improved articulation with four independently actuated limbs, creating six DOF in the end effector platform. Two variations of this concept are considered; one with cameras mounted directly to the end effector platform having the articulation of the limbs to follow the circular camera path. This allows for a relatively small load at the top platform but requires a significantly greater reach both vertically and horizontally. This leads to a very wide base and limb lengths that are not practical.

Alternatively, the inclusion of a variable length arm like the previous concepts that extends from the platform with the limbs sole purpose to center the platform within the tunnel. Figure 4.3 below shows a model of this concept version. This reduces the required length of the limbs and ensures the platform remains centered, balancing the load. The additional degrees of freedom between the platform and the cameras presents a level of redundancy and precision in camera positioning that is likely to create unnecessary complexities in MIMO control. Structurally, the additional load of the arm creates a strong concern for the required strength of the actuated limbs, even at the shortened length compared to the first variation. As well, actuators with these capabilities are likely to be dimensionally large, heavy, expensive, or not feasible at all.

4.2.4 Boom Truck Concept

This concept took influence from telehandlers of the construction industry and bin pilers from the farm industry. These systems work on the premise of a telescopic set of extension booms that pivot and extend from a mobile base. The angle and extension

Figure 4.3: Stewart Platform Concept

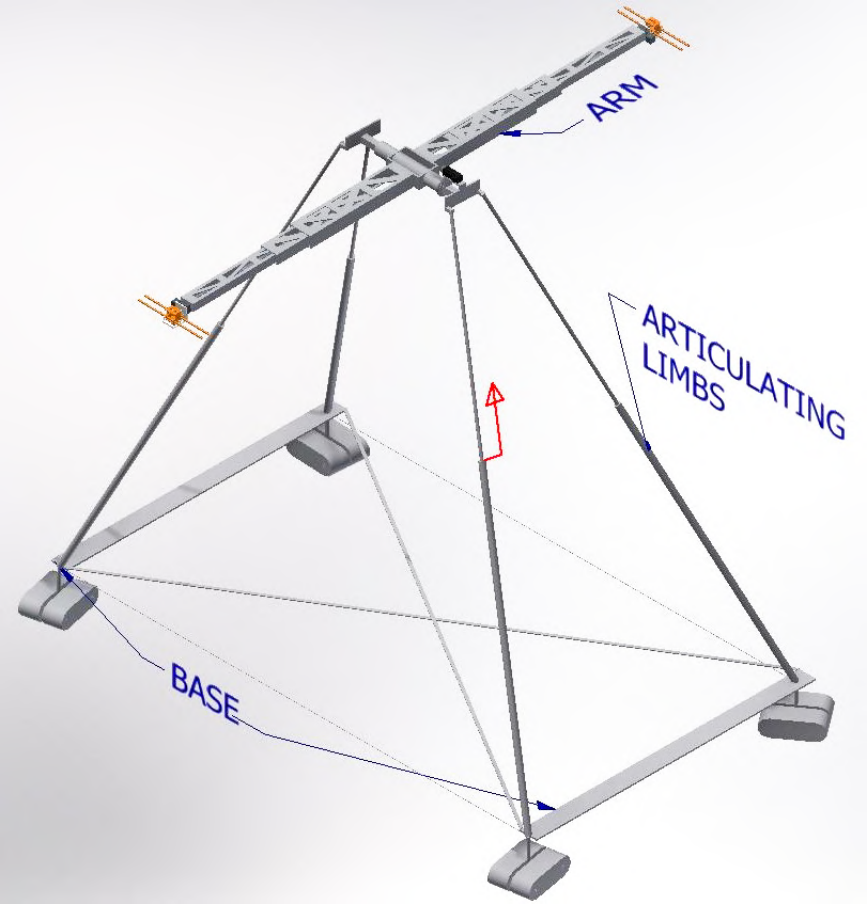

of the boom provide the elevation and forward offset of the camera, removing the need for a cantilevered arm such as in the Cantilever concept. The attached variable length arm at the tip of the boom independently provides the rotation and image capture operations. As the angle of the boom relative to the tunnel changes to account for different tunnel diameters, the arm must pivot about the boom tip to remain in a plane perpendicular to the tunnel axis. Figure 4.4 below details each of these components. With the boom elements originating at the rear of the base, an increase in stability can be obtained as compared to the Cantilever concept with a pure frontal load. This concept also decouples the image capture rotation with the elevation and offset set by the tunnel parameters. Although multiple actuations are required, variability of the frontal offset is achieved in addition to the elevation and camera rotation radius, which is not achieved by the previous concepts. Initial

concerns of this system are the overall weight and size of the system components, as well as the lateral stability concerns caused by the tall, three-wheeled system on the cylindrical surface.

Figure 4.4: Boom Truck Concept

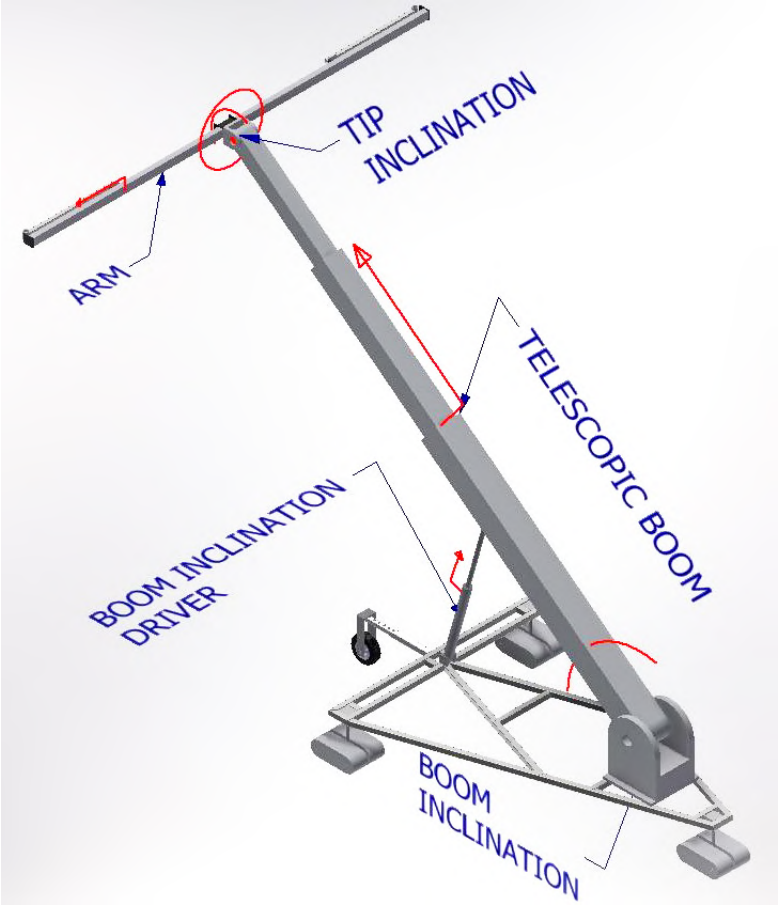

4.3 Evaluation and Decision Rationale

4.3.1 Evaluation

After detailing and understanding the functionality and abilities of each of the proposed concepts, comparisons were made based on the general functionality, the outlined considerations and aspects that influence an optimized design. For explanation purposes, these have been subjectively ranked based on their perceived foundational

performance, as well as the more well-defined factors described. The summary of this ranking is in Table 4.1. Beyond the analytical comparison, personal knowledge and experience played a significant part in the ranking and evaluation of the concepts. Additionally, familiarity of design concepts and mechanism knowledge were also influential factors in the consideration of the designs.

Table 4.1: Concept Relative Evaluation Table

Concept	Adaptability	Ease of Assembly	Overall Weight	Ease of Manufacturing	Control Complexity	Ease of Procurement	Total
Cantilever	4	2	1	1	1	2	11
Double-Mast	3	3	3	2	3	2	16
Stewart	2	4	4	4	4	4	22
Boom Truck	1	1	2	3	2	1	10

*Ranking from 1-4 relative to each other, 1 being the best rank.

4.3.2 Decision Rationale

Carefully maneuvering multiple sets of high-quality camera equipment through a cylindrical tunnel places a significant emphasis on reliability and stability, while the unique parameters that are applied by variable tunnel diameters requires a significant level of adaptability to effectively perform image data collection. These factors put the Boom Truck option at the forefront of the selection process. It has a more supported structure that is well balanced over the base compared to the Cantilever option, as well as additional variability in adjusting the forward distance between the cameras and the base. These factors, along with intuition that stems from

the collective experience within these tunnels and an understanding of the environments motivated the decision between the two closely ranked concepts. It also has a solid triangular base that has greater reliability on the cylindrical surface when compared to the multi-section base as in the Double Mast and Stewart platform concepts. Although this concept may have more structural components, the simplistic, common-shaped members are conceivably able to be disassembled into modular components that make transportation easy. The following chapter will document the further detailed design throughout continued revisions, including potential structural components and configurations.

Chapter 5

Detail Design and Analysis

The Automated Tunnel Inspector (ATI) system as a whole integrates a total of sixteen linear or rotational actuations to perform nine unique actions that achieve the camera articulation and global navigation needed to collect the required images. The following sections detail the required kinematics and dynamics as determined through simulation and calculations, the actuators and setup used to complete the actions, and the consideration and rationale for these conclusions.

A combination of robotic kinematic theory, general mechanical engineering principles, and dynamic simulation software have laid the foundation for understanding the kinematic and dynamic demands of each ATI joint. Simulations were used at various stages of the design and analysis process, initially to determine and visualize the kinematics of each joint and driving actuator throughout the entire Ranges of Motion (ROM) of the cameras. This subsequently provided the means for the dynamics of each driving member to be evaluated through that same range, providing information and specification targets for component selection. The ATI can be divided into three independent sections for these evaluations and simulations; the rotating arm components, the manipulation of the boom, and the maneuvering of

the ATI base. A collection of real and virtual images are collected in Appendix B.

5.1 Arm Manipulation

The manipulation of the arm accounts for the radial adjustment of the arm length, the orientation of the cameras, and the rotation of the complete arm. These actuations occur after the arm as a whole has been positioned and aligned with the center axis of the tunnel. For this subsystem of the ATI, the desired motion of each joint is defined and directly driven and therefore, act as the direct input for the dynamic analysis. For this dynamic simulation, the orientation change drives the rotary joint through a 90° rotation, each arm extends radially by 0.45 m, and the arm rotates and stops after 180°. The simulation spanned 30 seconds with each actuation being performed sequentially to analyze the independent response, as well as the coupled effect while others are not active. The actions performed within the simulation are set at higher velocities and accelerations than were anticipated to be applied in practice, providing conservative information and allowing for flexibility in future applications. Figure 5.1 visualizes the ATI at the start, end, and an intermediate position of the simulation, with a tracing of the camera position throughout. The corresponding set motion profiles and resulting joint dynamics are displayed in Figures 5.2 - 5.4 within the following sections, along with a summary of the key parameters and details in Table 5.1 below.

Table 5.1: Arm Manipulation Simulation Summary

Action	**ROM**	**Time**	$Load_{Peak}$
Arm Extension	0.45 m	4 sec (6-10)	145 N
Orientation Change	90°	4 sec (1-5)	5 Nm
Arm Rotation	180°	18 sec (11-29)	15 Nm

Figure 5.1: Simulation of arm manipulation components: orientation rotation, arm extension, arm rotation

(a) Start position (t=0s) (b) Mid-operation (t=17s) (c) End position (t=30s)

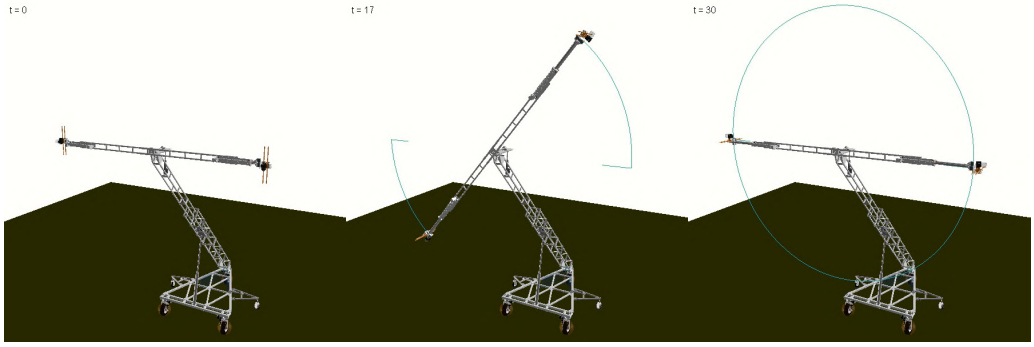

5.1.1 Arm Rotation

During operation, the rotation of the entire arm has to be a slow and steady process to maintain a stable camera. The anticipated operational rotation speed for most applications is in the range of 1-3 degrees per second, while it can also be required to move quicker in manual rotation cases. The arm was simulated through a rotation of 180 degrees to and from a stationary position over 18 seconds, resulting in peak rotational speed of 13.3 degrees per second. The oscillatory noise in the torque response at the beginning of the simulation is a symptom of the simulation software and the effect of the initial gravitational force on the ATI system as it initializes and settles onto the ground surface. This operation is performed with a geared stepper motor providing a nominal output torque of 110 Nm up to a speed of 4 rpm (24 degrees per second). Figure 5.2 shows the torque response of arm rotation throughout the defined motion profile.

5.1.2 Arm Radial Extension

Completing the radial adjustment of the ATI arm is achieved with two synchronized linear actuators driving telescopic members that hold the photography equipment.

Figure 5.2: Arm rotation simulation dynamic response.

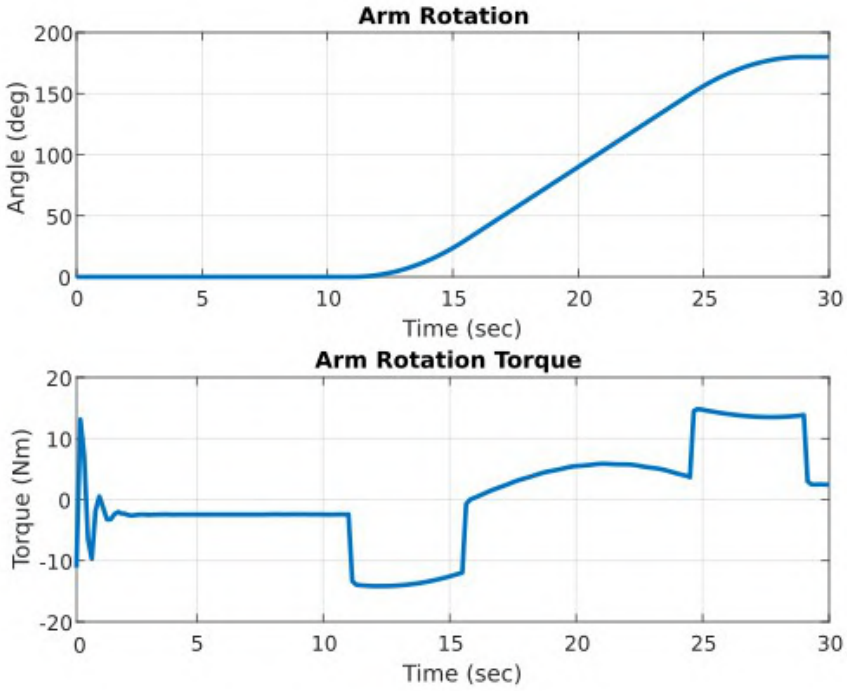

Figure 5.3 shows the dynamic response of the radial extension joint. The actuators used are the 0.45 m stroke optical feedback actuator FA-OS-240-12-18 from Firgelli® Automations, providing 890 N of dynamic force. Optical feedback of each actuator is used to match both the speed and position throughout the trajectory, Section 6.2 details the control techniques for this action. A set of square linear guide bearings are used to absorb the bending moment and torsion to reduce these loads from the actuators; these also provide smoother operation during motion.

5.1.3 Orientation Control

Toggling of the camera's orientation is a direct limitation on the rate that images can be captured, as detailed in Section 7.3.2.2. The actuators utilized for the orientation of each camera was a AY110-100-04 stepper driven rotary actuator from Optimal Engineering Solutions, Inc. [23]. A 4 second orientation toggle was simulated with

Figure 5.3: Arm extension simulation dynamic response

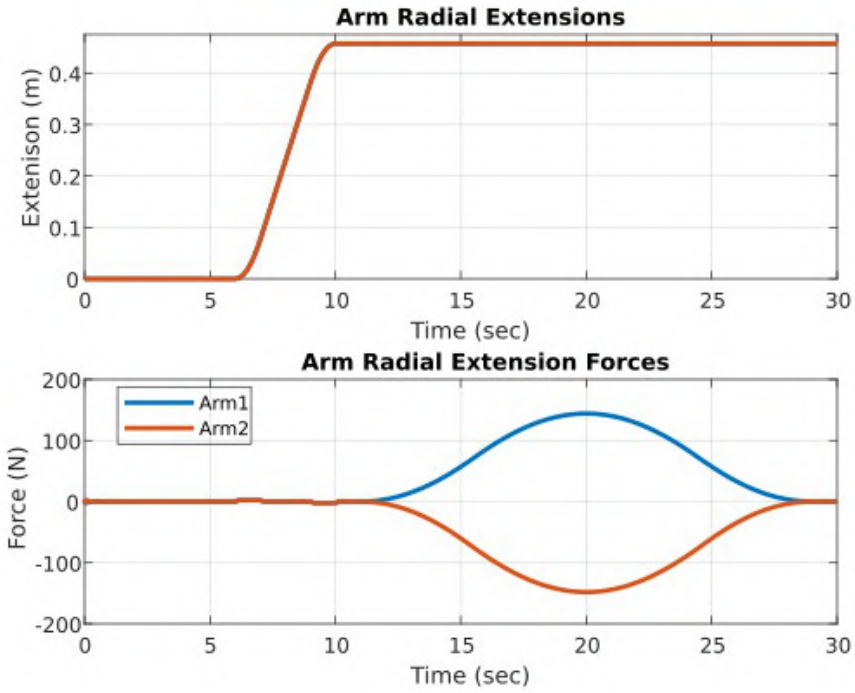

a peak speed of 30 degrees per second. This speed is faster than the rated speed of the rotary actuator used; the stepper driven rotary actuator integrates a 180:1 worm gear between the motor and where the photography equipment is mounted. Figure 5.4 shows the torque response of this actuator during the change of orientation and throughout the other arm manipulating actions.

5.2 Boom Manipulation

The centering and alignment of the entire arm is manipulated through the planar boom system consisting of three joint actuations: boom extension, boom inclination, and the tip inclination. The position of the boom tip relative to the base is altered with the extension and inclination of the boom. The rotation of the boom tip joint adjusts the pose of the arm center frame allowing for alignment with the tunnel axis to be maintained.

Figure 5.4: Camera orientation rotation simulation dynamic response.

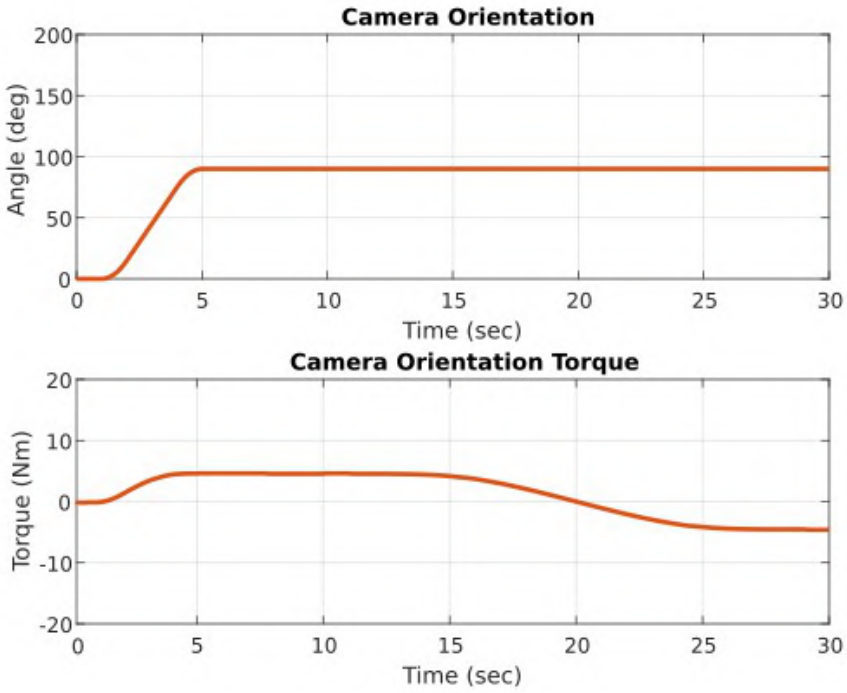

5.2.1 Simulation Analysis

The simulation performed on this section of the ATI demonstrates the manipulation of the ATI arm frame throughout a range of typical operating positions and to the extremes of its ROM as shown in Figure 5.5. A consistent frontal offset of 2 m is maintained between the base and the rotation plane of the camera arm throughout all positions. A pure vertical translation of the arm frame is completed from a fully lowered position with the arm center elevated to 2.25 m (Figure 5.5a) to full extension with the arm center at 4.5 m from the tunnel invert (Figure 5.5c). This range demonstrates the capabilities of the ATI to reach the center and align with the center axis of tunnels with diameters ranging from 4.5 m to 9 m.

Unlike the manipulation of the arm and camera components, the elevation and frontal offset of the arm are coupled and not directly controlled through single independent actuations.

Figure 5.5: Simulation of boom manipulation components: boom extension, boom inclination, tip inclination.

(a) Starting lowered position (t=0s) (b) Mid-operation (t=16s) (c) End elevated position (t=32s)

The first phase of the simulation is implemented to determine the motion requirements of each joint and corresponding driving actuators to define the position and trajectory of the arm frame. This facet is determined through an inverse kinematic analysis providing the results displayed in the kinematics portion of Figure 5.6. Subsequently, the calculated motion profiles become the input for a dynamic analysis to determine the corresponding forces and torques to produce the required accelerations to achieve the defined motions. The dynamics plot in Figure 5.6 displays the results from this analysis for the trajectory defined above. Key parameters and extracted values are summarized in Table 5.2.

Table 5.2: Boom Manipulation Simulation Summary

Action	**ROM**	$Load_{Peak}$
Boom Inclination	0.8 m	1500 N
Boom Extension	1.3 m	460 N
Tip Inclination	0.15 m	180 N

The simulations provide a detailed analysis of the kinematics, dynamics, and visualization of the ATI throughout specific trajectories and poses. It provides information on critical positions, peak load conditions, and additional information that benefits

Figure 5.6: Arm frame elevation simulation: Inverse kinematics and dynamics

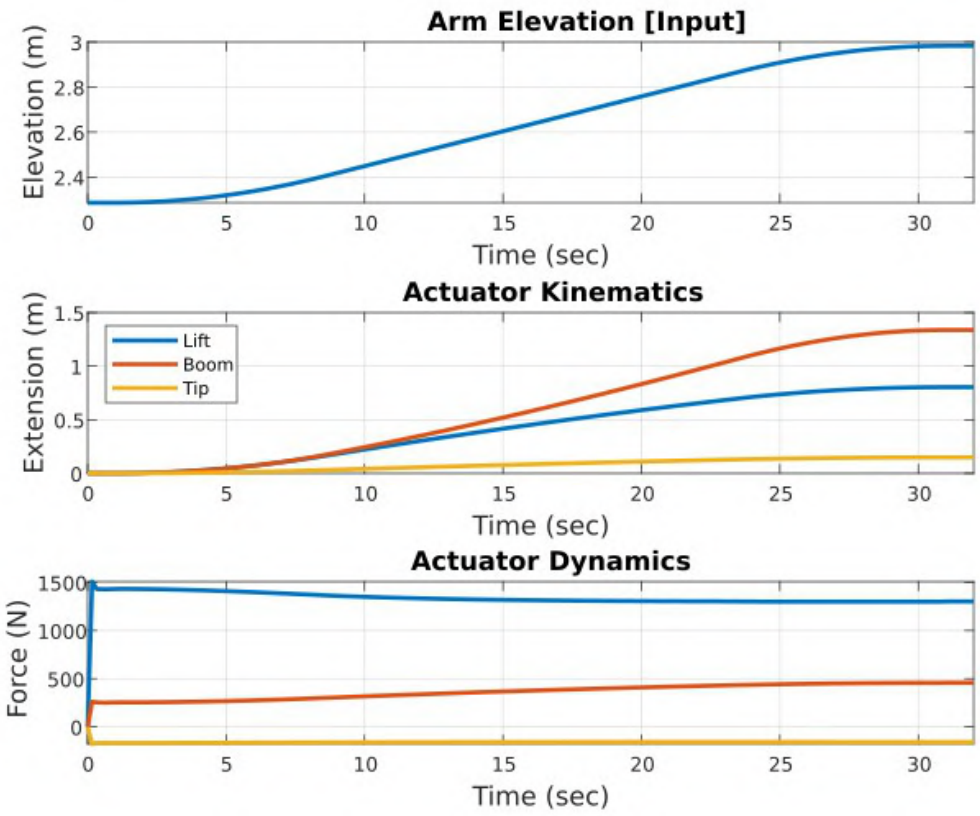

the selection and sizing of driving components.

5.2.2 Analytical Analysis

Generalizing the kinematic relationship between each driving joint and the end arm position is provided through the analytical form derived from both the simulated model and the modified-Denavit-Hartenberg (mDH) conventions. The general kinematic relationship derivation that follows is associated with the spatial description of the ATI boom presented in Figure 5.7. The parameters defining the relationship of adjacent links for this system are presented in Table 5.3, following the mDH convention [9]. This description defines the direct joints that form the Revolute-

Prismatic-Revolute planar mechanism of the boom.

Figure 5.7: ATI joint frame and DH parameter definitions.

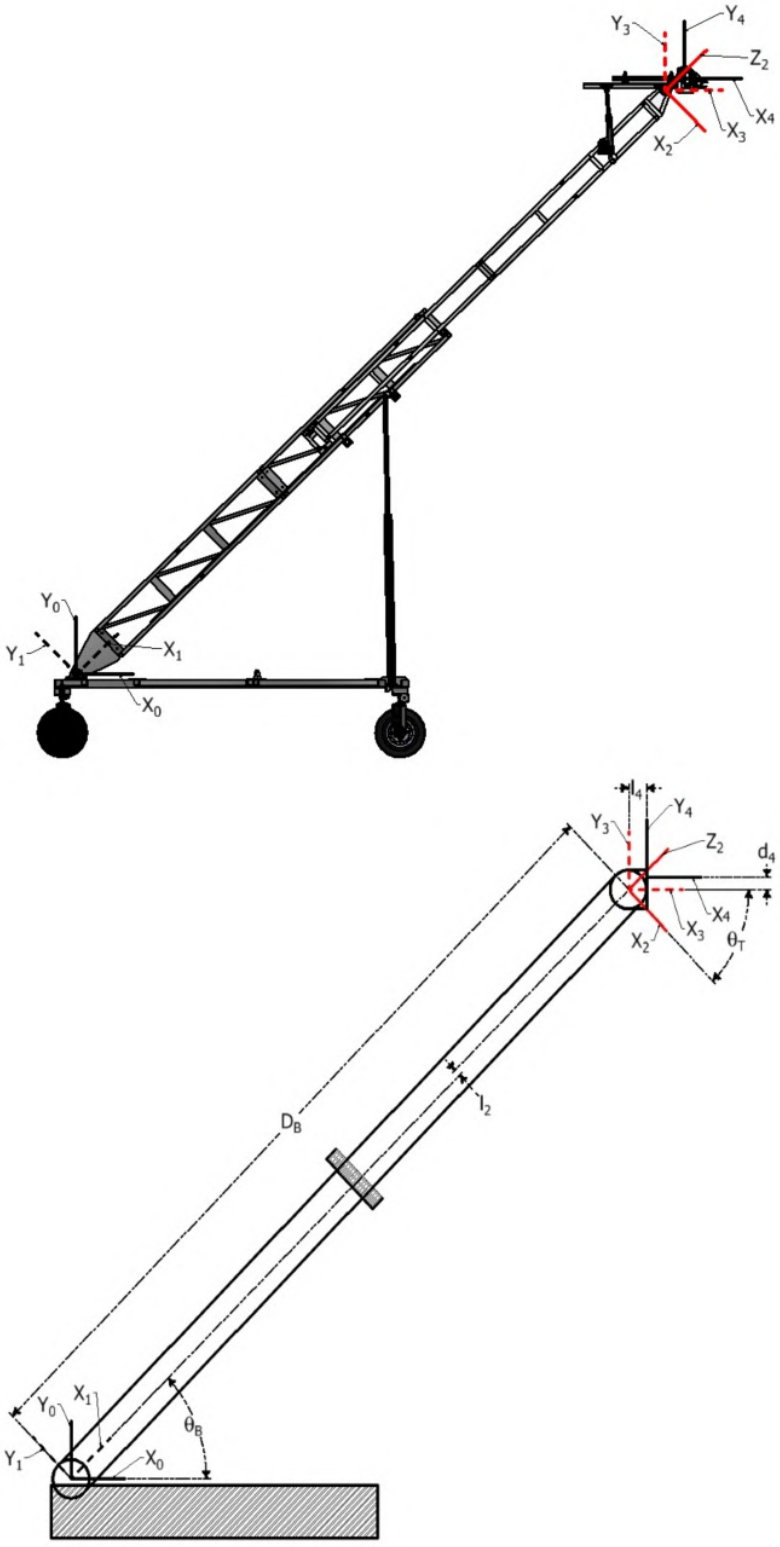

Table 5.3: Modified Denavit-Hartenberg Parameters of the ATI.

Link	α_{i-1}	a_{i-1}	d_i	θ_i
1	0	0	0	θ_B^*
2	$\pi/2$	l_2	D_B^*	0
3	$-\pi/2$	0	0	θ_T^*
4	0	l_4	d_4	0

The parameters in Table 5.3 are represented in Figure 5.7 and are used to formulate the homogeneous transformation matrices between each successive link, which, following the methods described in Section 3.2.1 are further combined to relate the arm center frame to the reference frame of the base as defined in Equation 5.1. This details the forward kinematic relationship between the arm center and base and is the basis for inversely determining the required joint positions for a defined elevation and frontal offset. This relationship can be expanded from the arm center to one of the end camera positions; however, this does not provide information relevant to this application. A more exhaustive collection of transformation matrices, joint relationships, and derivations within the process are provided in Appendix A. Notations c_i and s_i represent the cosine and sine values of θ_i respectively.

$$
{}^{Base}_{Arm}T = \left[\begin{array}{c:c:c:c}
c_B c_T - s_B s_T & s_B c_T - c_B s_T & 0 & l_2 c_B + d_B s_B + l_4 \\ \hdashline
c_B s_T - s_B c_T & c_B c_T - s_B s_T & 0 & l_2 s_B - d_B c_B + d_4 \\ \hdashline
0 & 0 & 1 & 0 \\ \hdashline
0 & 0 & 0 & 1
\end{array}\right] \tag{5.1}
$$

The angle of the boom and the tip joints, and the length between these joints as altered by the boom length are derived from the inverse displacement analysis. Equations 5.2 and 5.3 define these relationships; where, θ_B and θ_T are the angle of the boom and tip respectively, x_{Tip} and y_{Tip} depict the horizontal and vertical position of the tip frame relative to the base origin, x_{Arm} and y_{Arm} represents the same for

the arm frame. Parameter d_B defines the stroke of the boom extension actuator, with $\hat{d}_B$ representing the boom length in the fully retracted position.

$$\theta_B = -\theta_T = atan2(y_{Tip}, x_{Tip}) = atan2((y_{Arm-d_4}), (x_{Arm} - l_4)) \tag{5.2}$$

$$D_B = d_B + \hat{d}_B = \sqrt{x_{Tip}^2 + y_{Tip}^2} = \sqrt{(x_{Arm} - l_4)^2 + (y_{Arm} - d_4)^2} \tag{5.3}$$

Further expanding this relationship to incorporate the linear actuator configurations that drive the revolute joints includes the spatial representations defined in Figures 5.8 and 5.9. Equations 5.4 and 5.5 define the forward and inverse displacement relationship between the boom inclination angle and the overall length of the driving lift actuator. While similarly, Equations 5.6 and 5.7 define the forward and inverse displacement relationship between the tip inclination angle and the overall length of the driving tip actuator. These relationships are used to control the actuators through the user inputs of tunnel diameter and required frontal offset. These inputs translate to a global position of the arm center and convert to a pose relative to the base through known dimensions of the ATI base.

$$\theta_B = acos\left(\frac{-(d_L + \hat{d}_L)^2 + \alpha_L^2 + \beta_L^2}{2\alpha_L\beta_L}\right) + acos\left(\frac{\beta_L^2 - \lambda_L^2 + \rho_L^2}{2\beta_L\rho_L}\right) - atan\left(\frac{\gamma_L}{\phi_L}\right) \tag{5.4}$$

$$\begin{aligned} d_L &= \sqrt{-2\alpha_L\beta_L A_L + {\alpha_L}^2 + {\beta_L}^2} - \hat{d}_L, \\ \text{where,} \quad A_L &= cos\left[\theta_L - acos\left(\frac{\beta_L^2 - \lambda_L^2 + \rho_L^2}{2\beta_L\rho_L}\right) + atan\left(\frac{\gamma_L}{\phi_L}\right)\right] \end{aligned} \tag{5.5}$$

Figure 5.8: Defining parameters relating driving actuator of boom inclination joint.

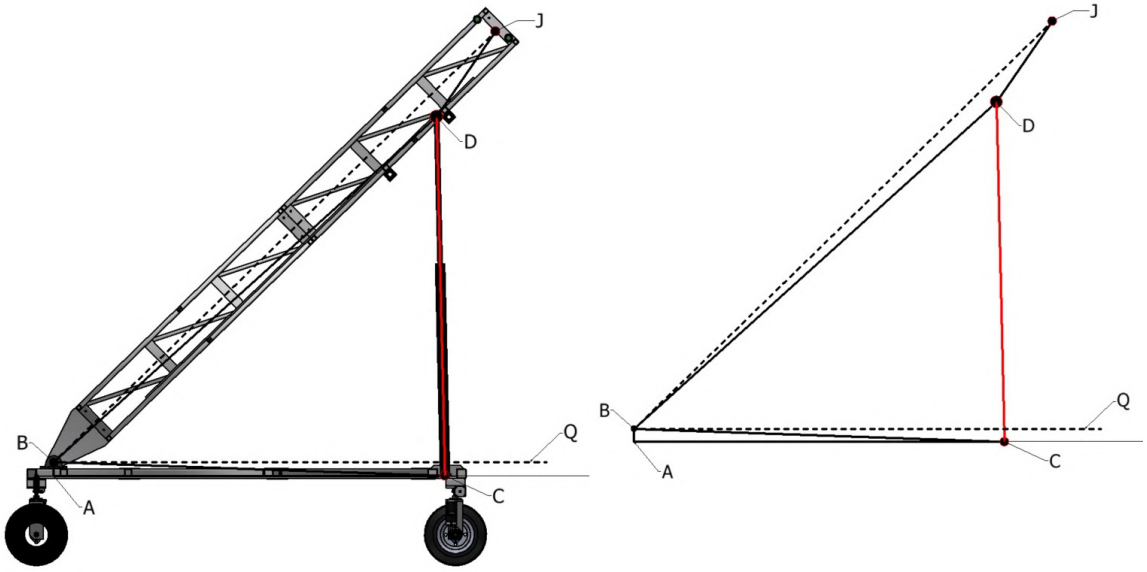

Figure 5.9: Defining parameters relating driving actuator of tip inclination joint.

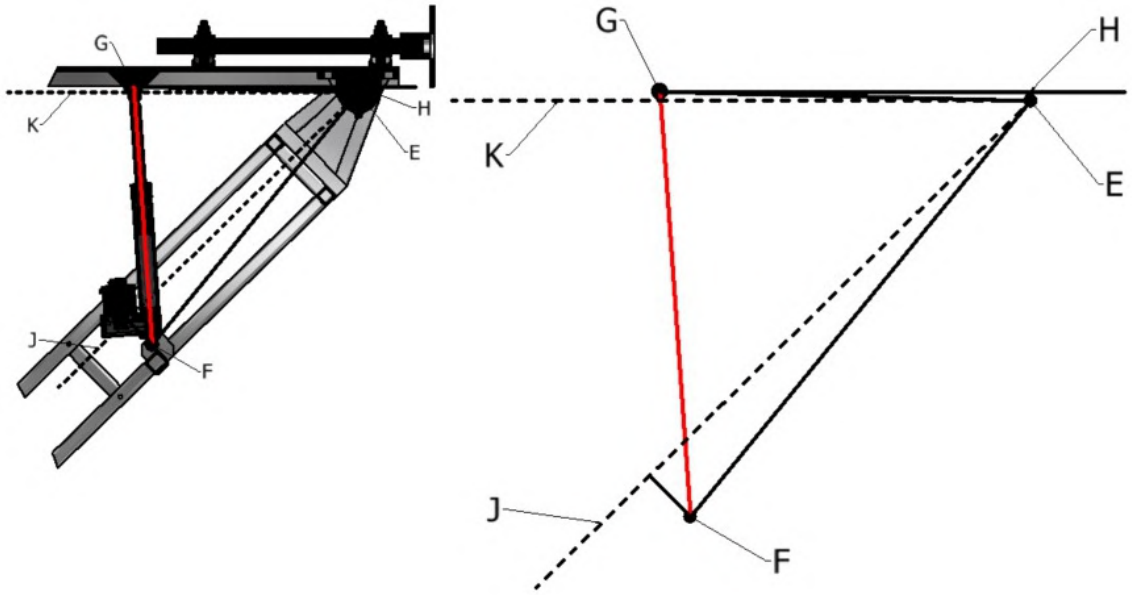

$$\theta_T = acos\left(\frac{-(d_T + \hat{d}_T)^2 + {\alpha_T}^2 + {\beta_T}^2}{2\alpha_T\beta_T}\right) - acos\left(\frac{{\beta_T}^2 - {\lambda_T}^2 + {\rho_T}^2}{2\beta_T\rho_T}\right) - atan\left(\frac{\gamma_T}{\phi_T}\right) \tag{5.6}$$

$$
\begin{aligned}
d_T &= \sqrt{-2\alpha_T\beta_T A_T + {\alpha_T}^2 + {\beta_T}^2} - \hat{d}_T, \\
\text{where,} \quad A_T &= cos\left[\theta_T + acos\left(\frac{\beta_T^2 - \lambda_T^2 + \rho_T^2}{2\beta_T\rho_T}\right) + atan\left(\frac{\gamma_T}{\phi_T}\right)\right]
\end{aligned}
\tag{5.7}
$$

Table 5.4: Parameter definitions for driving actuators of the lift and tip joints.

Lift		**Tip**	
Label	**Value**	**Label**	**Value**
α_L	BC	α_T	EG
β_L	BD	β_T	EF
γ_L	AB	γ_T	EH
λ_L	BJ	λ_T	EJ
ϕ_L	AC	ϕ_T	HG
ρ_L	DJ	ρ_T	FJ
D_L	DC	D_T	GF

Parameters d_T and d_L define the stroke of the tip and lift actuators, with $\hat{d}_T$ and $\hat{d}_L$ representing the respective actuator lengths in the fully retracted positions. Other parameters correspond to those defined in Figure 5.8 and 5.9 and are summarized in Table 5.4.

5.2.3 Specifications and Components

The extension and retraction of the boom is performed with a stepper driven linear belt and pulley system. Alternative mechanisms considered were a self contained linear actuator, a lead screw drive, and a chain and sprocket assembly. While each of these can be viable options, unique drawbacks and limitations were identified in the evaluation. The linear actuator provides a concise and direct solution with minimal components and direct application; however, obtaining an actuator that meets both the displacement and driving force requirements was not readily available and required custom ordering leading to extended lead times. The lead screw solution provides ample adaptability although requires the integration of several unique components. It would also require lubrication and additional protection from the envi-

ronment; all in all deeming it to be an over-complicated solution. The chain and sprocket assembly operates the same as the belt and pulley system, however, a chain outweighs a belt per unit length and is more difficult to compact. A belt and pulley also provides cleaner operation without the need for lubrication, which is important when in near contact with the photography equipment.

The inclination of the boom is the largest actuation of the system. Moving the large frame of the boom with the extended arm creates a substantial moment about this joint. Driving this joint with a linear actuator offers a simple way to provide sufficient torque to rotate this joint that a common direct rotary actuator could not supply. The ROM of the boom angle requires a 0.75 m displacement of the driving actuator and a driving force of 1500 N. The FA-BH50-1124-12-30 actuator from Firgelli® Automations provides this stroke with 5000 N of driving force. As such a critical component that supports the entire boom, arm and cameras, such excessive force capacity is desirable. Hall effect sensors provide high resolution positional feedback of this actuation.

The inclination of the tip joint closely resembles the operation of the boom inclination with similar configurations. Although the ROM of the rotation are alike, the driving actuator being positioned close to the joint significantly reduces the stroke requirements to 0.15 m with a peak load of 180 N. The FA-PO-150-12-6 from Firgelli® Automations supplies 667 N over the 0.15 m stroke with positional feedback provided through a linear potentiometer.

Additional imagery and drawings of the assembly of these joints and ATI components are compiled in Appendix B.

5.3 Base Maneuvering

With three independently steered and driven wheels, there is significant control over the pose of the ATI within the environment constraints. The system developed and detailed within this section emulates a planar joint between the base and the surface of the tunnel, allowing for two-dimensional translation and one-dimensional rotation.

5.3.1 ATI Drive Control Concept

Direct control of three independently controlled drive systems becomes complex for the user having two inputs required per wheel (direction and velocity) to control the ATI. Therefore, a central control system has been designed to simplify the user interface and reduce the possibility of numerous and redundant inputs. This concept is divided into two sections based on the anticipated motions required while inspecting the tunnel: a pure translation mode and a curve-following mode.

5.3.1.1 Translation

The pure translation scenario will be frequent in straight sections of the tunnel in which the ATI will move along the axis of the tunnel. It will also be prevalent in the transverse motion of centering the ATI in the tunnel invert. This pure translation can be achieved through the synchronization of each wheel's direction and velocity, with a single universal direction and velocity input of the ATI base. This creates a simplified user interface, reducing the total number of inputs required from six to just two.

5.3.1.2 Curve Following and Rotation

The curve-following or rotation mode will address the scenario in which the tunnel being inspected consists of a horizontal curve with a known radius of curvature. This also provides means for general reorientation of the ATI for alignment or general steering. The complications of following the curvature of the tunnel arise from the discrepancy between the location of each wheel in reference to the turn radius point, being the center of the ATI base. To effectively follow the curve and avoid wheel slippage, each wheel must be oriented tangential to its respective turn radius and rotate at a proportional velocity. Visualization of this is shown in the Figure 5.10. Similar to the translation mode, control in this manner reduces the number of user inputs required to just two, the desired velocity and the radius of curvature. This can be applied to the complete all-wheel drive and steer system, or reduced to a front-wheel drive system that mimics typical road vehicles.

Figure 5.10 represents the relationships between the required directions (θ_i) of each wheel based on the fixed physical properties of the base (L_{wy}, L_{wx}, L_{wBy}) and the desired curve radius of the ATI (r_{ATI}).

The direction of the front wheels can be defined as follows:

$$\theta_{wi} = arctan[L_{wy}/(r_{ATI} \pm L_{wx})] \tag{5.8}$$

The direction of the rear wheel is defined as follows:

$$\theta_{wB} = -arctan[L_{wBy}/r_{ATI}] \tag{5.9}$$

Based on the position of the wheels relative to the turn radius reference, each wheel has a unique turn radius resulting in the requirement of unique wheel velocities. This

Figure 5.10: Properties defining wheel direction and velocity when rotating or following a curve.

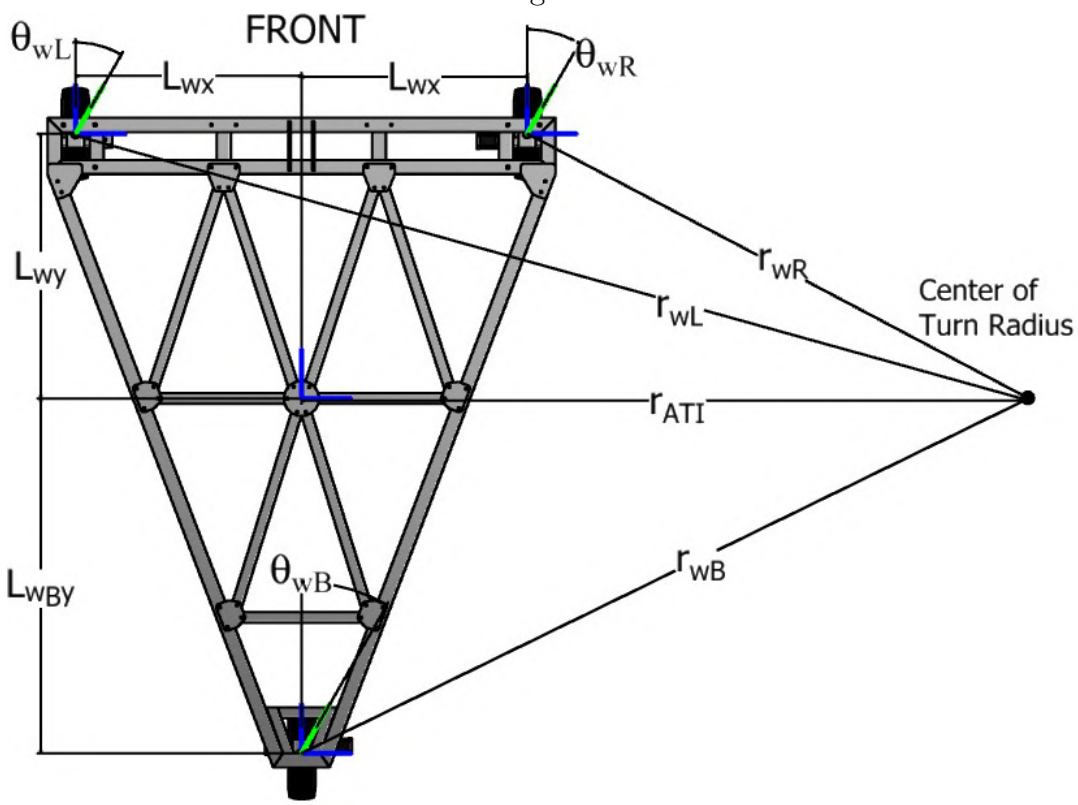

proportional relationship is defined as:

$$\omega_{wi} = (r_{wi} v_{ATI})/(r \cdot r_{ATI}) \tag{5.10}$$

Here ω_{wi} is the angular velocity of wheel i, r is the radius of the wheel, v_{ATI} is the desired linear velocity of the ATI, and r_{wi} is the artificial turn radius of wheel i, which can be defined for each wheel (Equation 5.11 for front wheels, Equation 5.12 for the back wheel) based on the relationships:

$$r_{wi} = \sqrt{L_{wy}^2 + (r_{ATI} \pm L_{wx})^2} \tag{5.11}$$

$$r_{wB} = \sqrt{(L_{wy}^2 + r_{ATI}^2)} \tag{5.12}$$

These parameters along with the user inputted ATI velocity and curve radius provide effective setpoints for each wheel to implement complete control over the independent drive systems.

5.3.2 Components and Simulations

The three drive systems consist of the same wheel, geared steer motor, and a direct-drive geared drive motor. The motors controlling the steer direction of each wheel are mounted to the base frame of the ATI, while the drive motor is directly mounted to the drive wheel chassis. Each entire chassis system gets connected to the base, coupling with each steer shaft. The analytical methods described in Section 3.3, along with the extensive simulations, formulate the foundation of the vehicle model and provide the basis for determining basic drive requirements. Simulations provide a visualization of the 3D motion and the dynamic response of the ATI while performing various driving actions at various speeds and over various slopes.

Figure 5.11 displays the resulting torque requirements for the ATI to accelerate up various slopes using the all-wheel drive configuration. Each scenario is defined with consistent parameters excluding the changing slope. Beginning from a stationary position on the sloped surface, the ATI smoothly accelerates over a three second interval to a steady state speed of 10 m/min, which is subsequently maintained for the remaining time. The front wheel torque shown is for each individual wheel.

Clearly shown and as expected, the total tractive effort required increases proportionally as the surface slope is increased. This is in response to the increased grade resistance as discussed in Section 3.3.3. As is expected due to the center of gravity

Figure 5.11: Resulting wheel torque requirements from simulations of increasing surface slope at speed of 10 m/min.

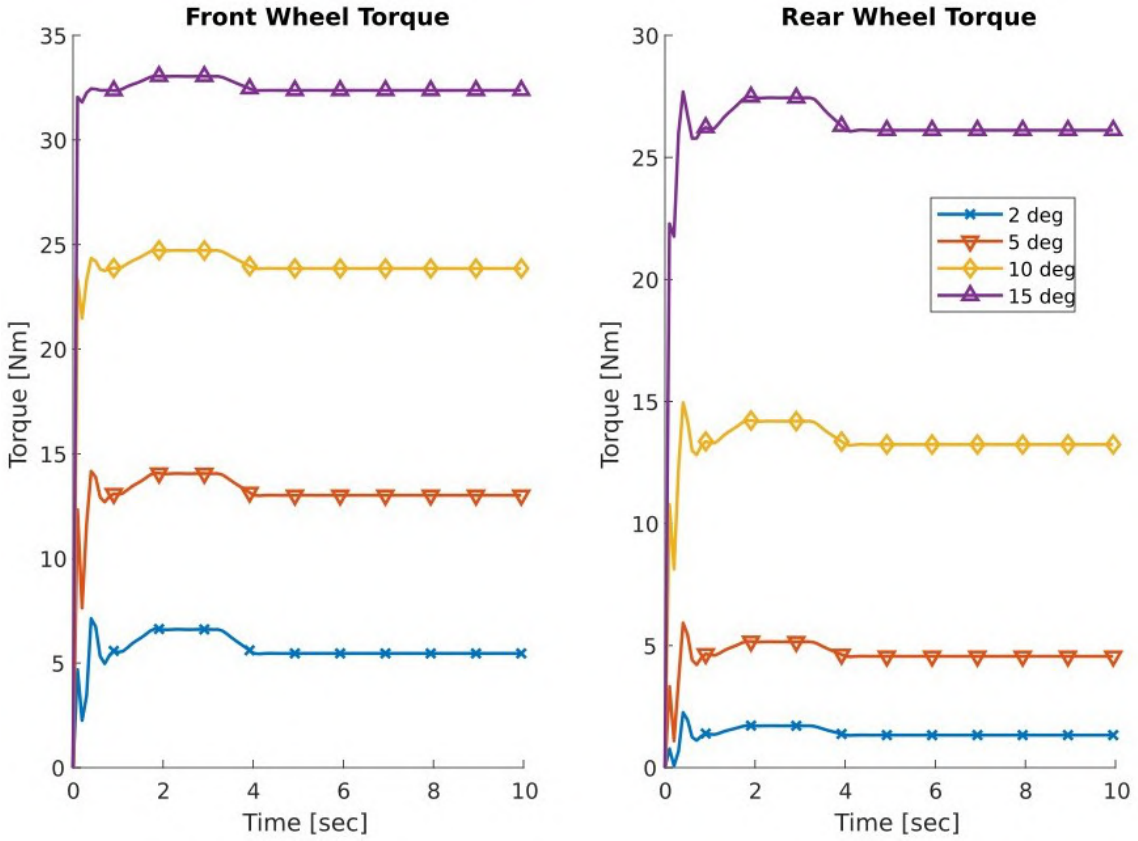

of the ATI being located towards the front axle, the front wheels provide the majority of the tractive effort to drive the ATI. The ratio that is provided relative to the rear wheel is reduced as the slope of the surface increases. Although the load requirements are not identical, the same motor-gearbox combination is used for each drive system to limit the number of unique components. This combination was sized based on the peak slope and load scenarios with a safety factor of at least two to maintain sufficient control in any anticipated environment.

Chapter 6

Control Systems

The majority of the different actuators and controlling components are divided into their own subsystems with closed loop control contained within. A high-level schematic of the layout and integration of components from the exterior actuators to the central command system and user interface is presented in Figure 6.1. These systems respond to high level control inputs that are derived from the user input parameters and the overarching Automated Tunnel Inspector (ATI) control concepts. This chapter discusses the different closed loop control techniques used for driving these systems, whether independently or synchronized with others.

A Graphical User Interface (GUI) was developed to connect the user with all elements of the ATI and the collection process. The interface provided multiple different methods of control for different scenarios and applications; manual control over each individual actuation, combined control of subsystems, different driving methods, and an operational scanning mode according to specified tunnel and capture parameters. The set up allows the user to control the ATI from a laptop mounted to the frame, as well as the option to operate through a mobile device which can be remotely connected to an onboard Raspberry Pi.

Figure 6.1: Schematic of component layout and connectivity.

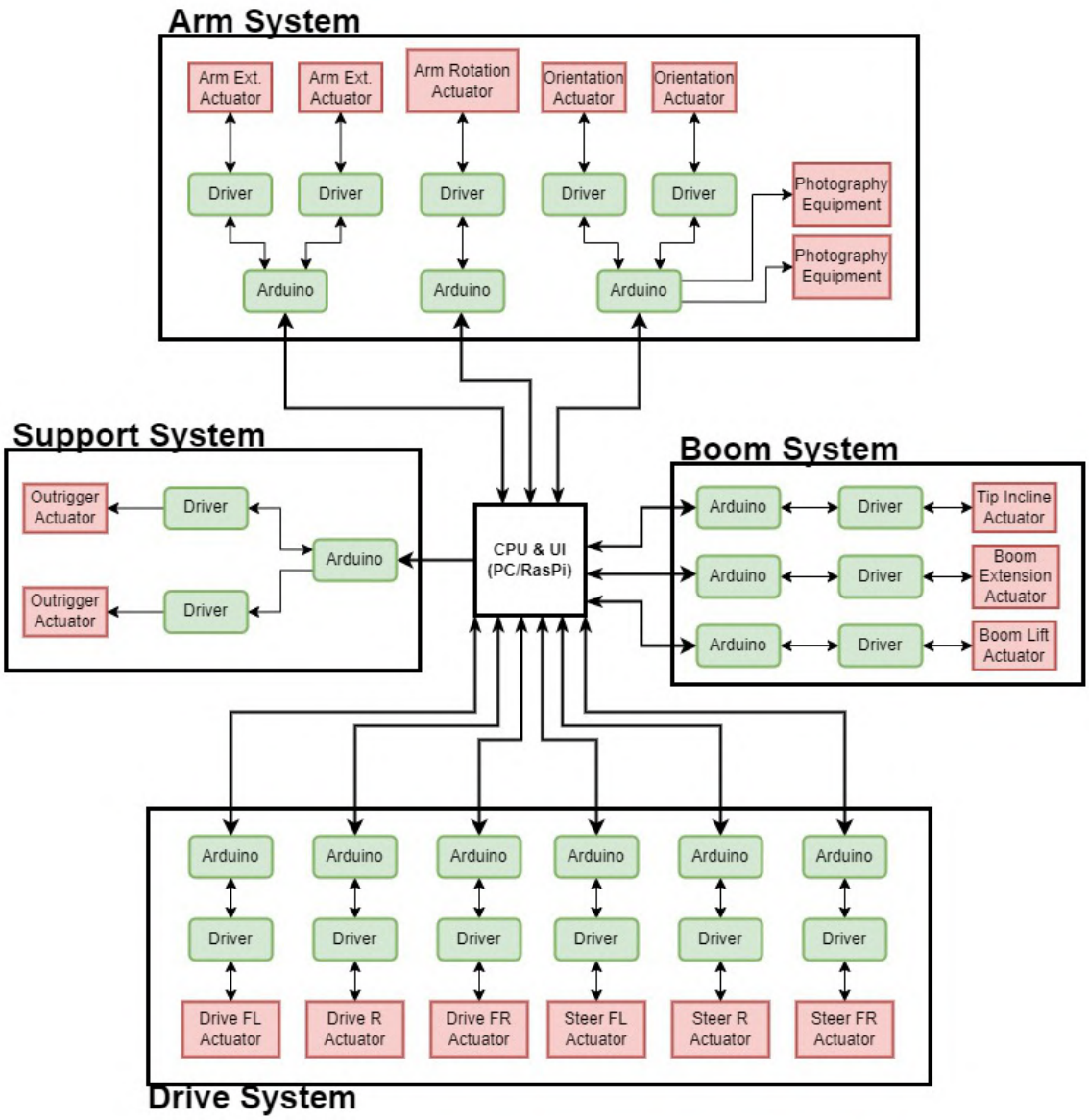

Effective system control heavily relies on the quality of the system data or analytical models that are available. Model identification of each system was conducted experimentally, by analyzing open loop data to create empirical-based analytical models of each system. This process began with the collection of open loop response data from various inputs. As the open loop responses did not show significant oscillatory behavior, first order approximations were made from this data to estimate open loop characteristics and formulate accurate models of each system. Simulations of these models in response to the same inputs from the experiments were conducted to determine their accuracy. Closed loop transfer functions for PI control or dynamic matrices for Model Predictive Control (MPC) were then developed and tested in simulation to evaluate performance and tune if needed before physical implementation. This section discusses the formulation and performance of the general control scheme, as well as the more complex control of the synchronized arm extension actuators and the drive system. A more extensive collection of experiment data and system information is attached in Appendix C.

6.1 General Control

The demands of all the ATI actuations vary significantly; some require velocity control, some positional control, and others a combination of both. Many of the actuations are performed at low speeds and only experience small accelerations resulting in gradual transients in the dynamic responses. Due to this, actuations that have low peak speeds, experience small accelerations, and require only control of the end position, perform effectively using a simple ON/OFF control strategy. This method operates the actuator at full capacity until the positional feedback identifies that it is at the desired position. A tolerance buffer is added to the setpoint to avoid undesirable rapid toggling around the setpoint. The schematic for this concept is shown

in Figure 6.2 and has been applied to the linear actuators driving the inclination of the tip and the boom as they meet the above characteristics.

Figure 6.2: Schematic diagram for general ON/OFF control system.

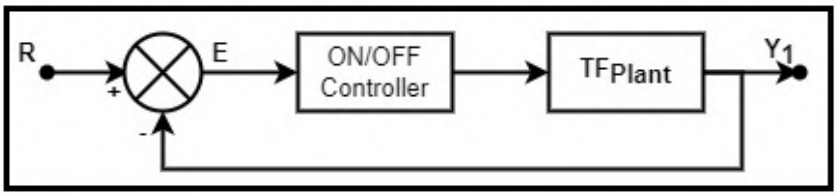

Aspects that require additional control of velocity throughout the entire motion utilize this ON/OFF strategy with an additional internal feedback loop including a PI controller. Development of the controller followed the methods outlined above utilizing open loop experiments to determine analytical models and ultimately tune the controller gains. Figure 6.3 shows the general schematic of this control method. This method was applied to the driving of the boom extension system, rotation of the arm, and also acts as a subsystem of the radial arm extension as described in Section 6.2.

Figure 6.3: Schematic diagram for general PID control system.

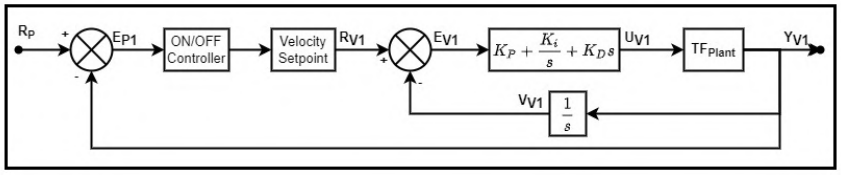

6.2 Arm Radius Synchronization

Synchronizing the extension of the radial arm actuators is key for maintaining equilibrium of the arm and avoiding a significant imbalanced load scenario. A relatively small extension discrepancy between the two actuators will create a significant moment on the arm rotation joint. This could impact the arm's ability to effectively rotate or hold its current position if the moment imposed on the rotation joint is ex-

cessive. To avoid this, the extension position of the actuators must be synchronized. Although the load carried by each of the actuators is the same, the angle at which the arm is positioned alters the driving force required to extend or retract the actuators. This in combination with internal resistances of the actuators and translating assembly could result in discrepancies between the speed of each actuator, and ultimately differing motion profiles on the way to the position setpoint. Therefore, in addition to matching the end setpoint position, the velocity throughout the extension action must be synchronized for the two translational systems as well.

The velocity control is based on a master-follower system. The master and follower systems change depending on the instantaneous relative position of each; the translational system that is lagging behind becomes the master so that the leading system can reduce its speed to match the other. The positional control is simply completed with an ON/OFF controller for each system with a single setpoint. This works by allowing the respective velocity control of the system to function until the position reaches the setpoint within a predefined tolerance. A schematic of the complete control scheme can be seen in Figure 6.4. Here, subscript Lag or Lead indicates which system is lagging or leading relative to the other.

Figure 6.4: Schematic diagram for synchronized position and velocity control of the radial arm extensions.

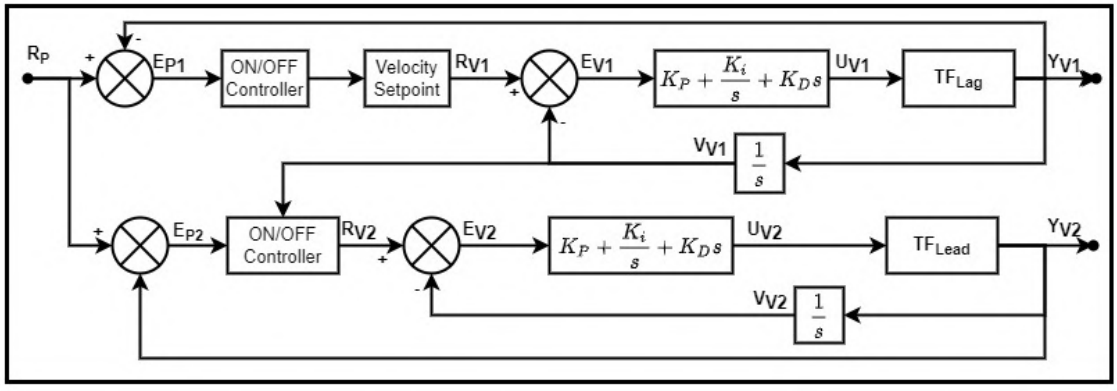

Through the system identification methods described earlier, analytical models of each arm were developed and simulated to determine the accuracy that they provide

in representing the physical system. A visual comparison of a simulation of these models against a set of open loop experimental data undergoing identical inputs is shown in Figure 6.5. The analytical models closely resemble the actual responses through both the transient and steady state phases. This process identified a peak extension difference between the arms of 2.49 cm (5.7%) and a steady state velocity difference of 0.041 cm/s (5.6%).

Figure 6.5: Open loop data of the analytical model compared with experimental data of the arm actuators.

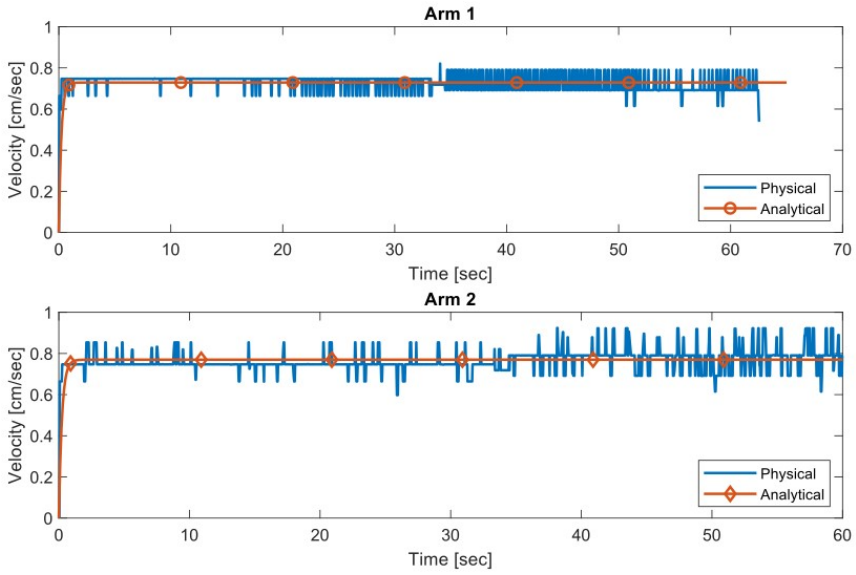

These models serve as the foundation for control development of a PI controller, chosen for the improved steady state response and simplistic implementation. Closed loop specifications of a 0.5 second settling time and an overshoot of 1% defined the parameters to determine the controller gains. A demonstration of closed control operation of the synchronized arm system in response to a setpoint of 0.28 cm/s as an analytical system and a physical experiment are shown in Figure 6.6 and 6.7 respectively. The closed loop feedback control synchronized the system responses throughout the extension maintaining a steady state error of 0.0035 cm/s (1.2%). This significantly reduces the discrepancy between the actuators position throughout and ensures a more balanced arm. Appendix C contains additional representations

of arm system open and closed loop data.

Figure 6.6: Closed loop data of the analytical arm model.

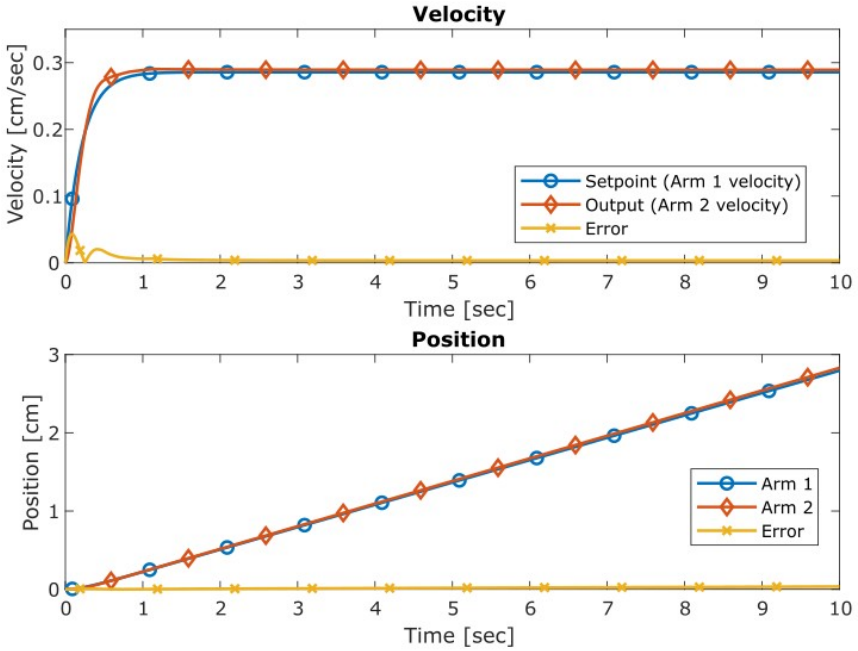

Figure 6.7: Closed loop data of the physical arm system.

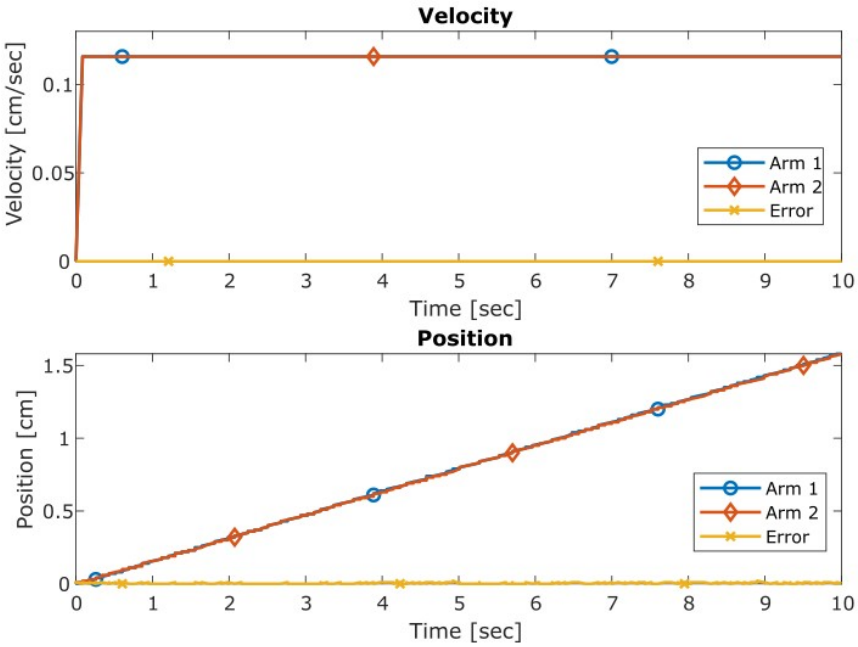

6.3 Drive Controls

Control of the ATI's drive system requires three inputs from the operator: desired drive mode, velocity of the ATI, and either direction of the ATI or the radius of curvature to be followed by the ATI, depending on the drive mode desired. The drive control mode algorithm described in Section 5.3.1 determines the individual setpoints for each drive and steer motor system based on the higher level user inputs. Subsequently, each wheel system has an independent closed loop MPC system to follow the velocity setpoint. Figure 6.8 shows the schematic of this system for controlling the wheel velocities. The control of the wheel steer motors is organized in a similar configuration, however, the ON/OFF positional control described in Section 6.1 is utilized in place of the MPC.

Figure 6.8: Schematic diagram for drive system controlling wheel velocities.

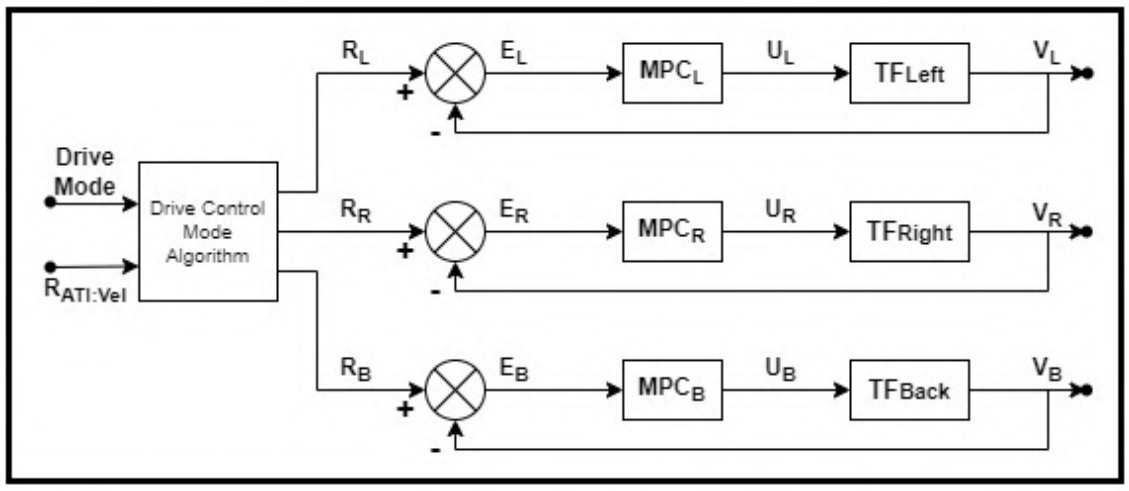

The velocity response was measured from each wheel over multiple open loop tests at varying voltage inputs. The input corresponds to a complete range of 0-100% of the rated motor speed, however, a minimum voltage is required to start up and maintain rotation. This was determined by constantly monitoring the response while incrementally reducing the input until the motor and wheel stopped spinning. Under standard loading on a typical flat surface, this was determined to be 6-7% which cor-

responds to a speed of approximately 0.45 rpm, defining a minimum wheel velocity. A set of low speed open loop responses can be viewed in Appendix C.

A set of open loop responses at various velocities was utilized to formulate analytical models to aid the development of closed loop control. Three sample experimental tests with inputs of 20%, 50%, and 100%, along with the analytical comparison, are shown in Figure 6.9. This depicts the accuracy of the analytical models, which allow for smooth representation of additional simulated responses before implementing on the physical system.

Figure 6.9: Open loop experimental and analytical drive responses from various input percentages.

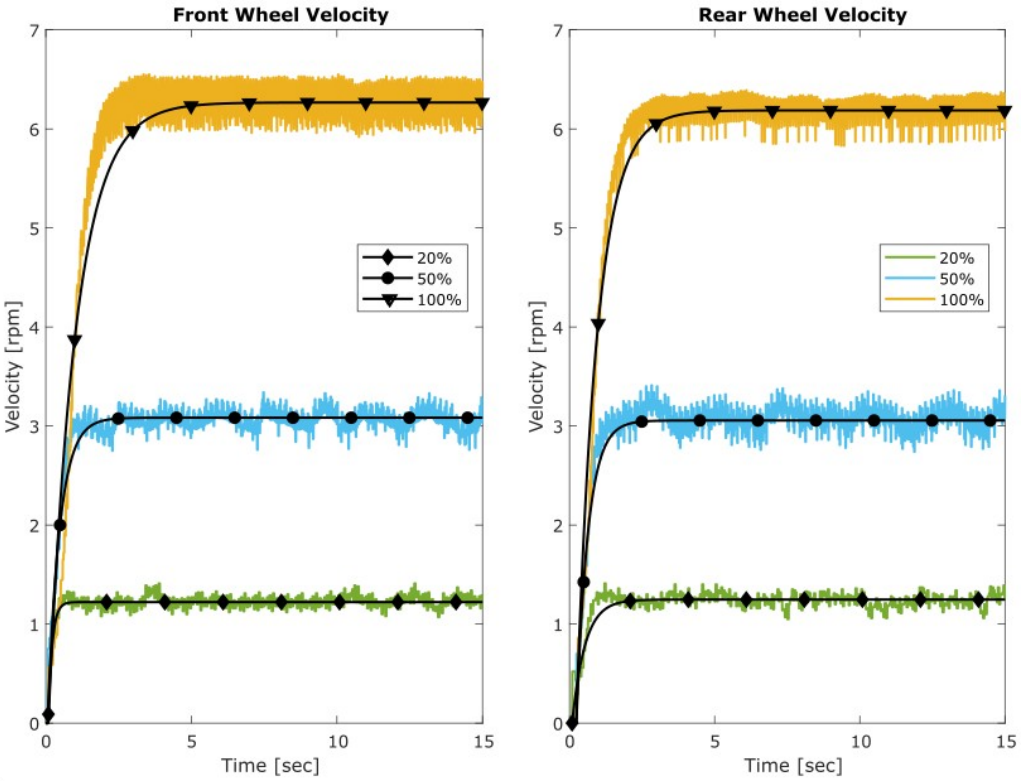

Following the methodology described in Section 3.4.2, an open loop response to a step input was used to construct a dynamic matrix to begin the implementation of MPC. Iterating through simulations while varying the control horizon allowed an optimal control horizon to be determined through a visual comparison. A set of responses from these iterations is presented in Figure 6.10, which clearly shows

that an increased control horizon experiences higher initial overshoot as a trade-off of settling on the setpoint more quickly. While oppositely, the lower horizons have reduced overshoot and a slower response time. For the application of drive velocity control, limiting undesired overshoot is important for safe control and operation, as well as ensuring the maximum linear advance is maintained.

Figure 6.10: Closed loop MPC response with varying control horizon.

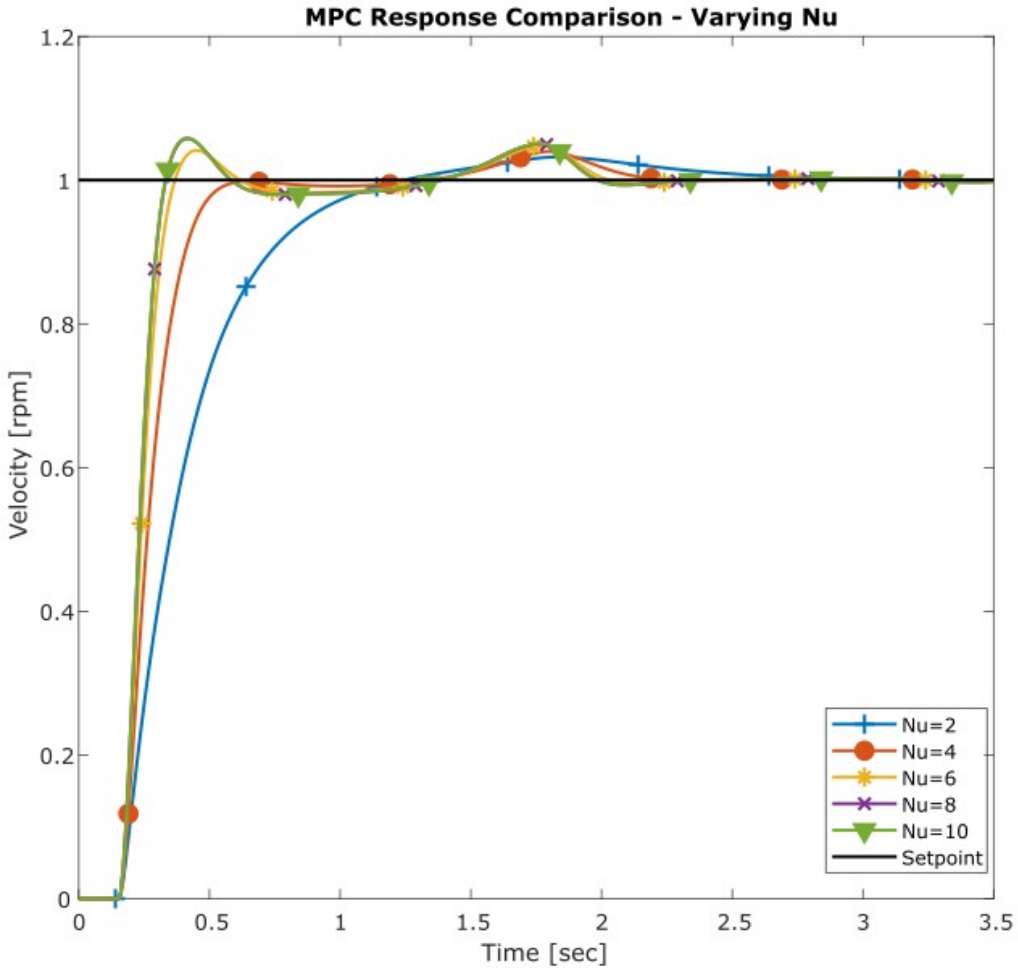

Additional tuning of the other MPC parameters further improves the response; creating a smoother transient to steady state transition and limits the volatility of the response. Iterations of simulations while varying these parameters led to the identification of an improved and close-to optimal set of parameters for driving these wheels. The optimal control horizon was determined to be four, a move suppression

factor of 0.2 was added and α was chosen to be 0.8. Figure 6.11 shows the output of the tuned response tracking multiple setpoints.

Figure 6.11: Closed loop MPC response with tuned parameters.

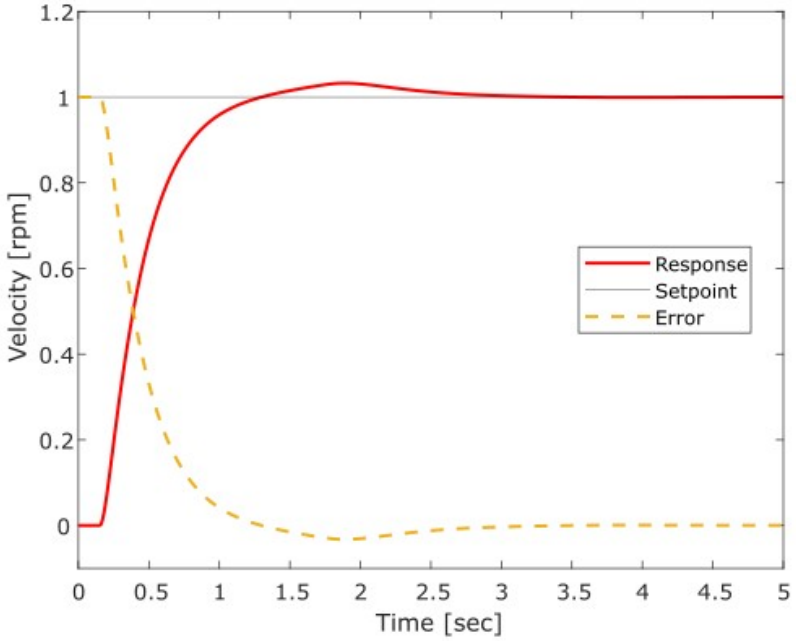

Following satisfactory close loop control simulations, experimental tests were conducted at various velocities to demonstrate effectiveness. Figure 6.12 demonstrates the response of a front wheel and the rear wheel while following different velocity profiles. A one dimensional median filtering has been applied to better present the noisy response data from these tests. The noise and volatility of the response increases proportionally with the output velocity, maintaining a relatively consistent signal-to-noise ratio. This plot shows the control technique performed effectively over the full velocity range following the set speed with minimal overshoot or significant error in most test. A minuscule yet consistent trend of the output velocity tracking slightly above the setpoint in each case; indicating a bias within the developed MPC dynamic matrix. A collection of simulated responses with different control parameters and setpoints are compiled in Appendix C, along with an exhaustive collection of closed loop experimental data from these systems.

Figure 6.12: Closed loop experimental MPC response with tuned parameters.

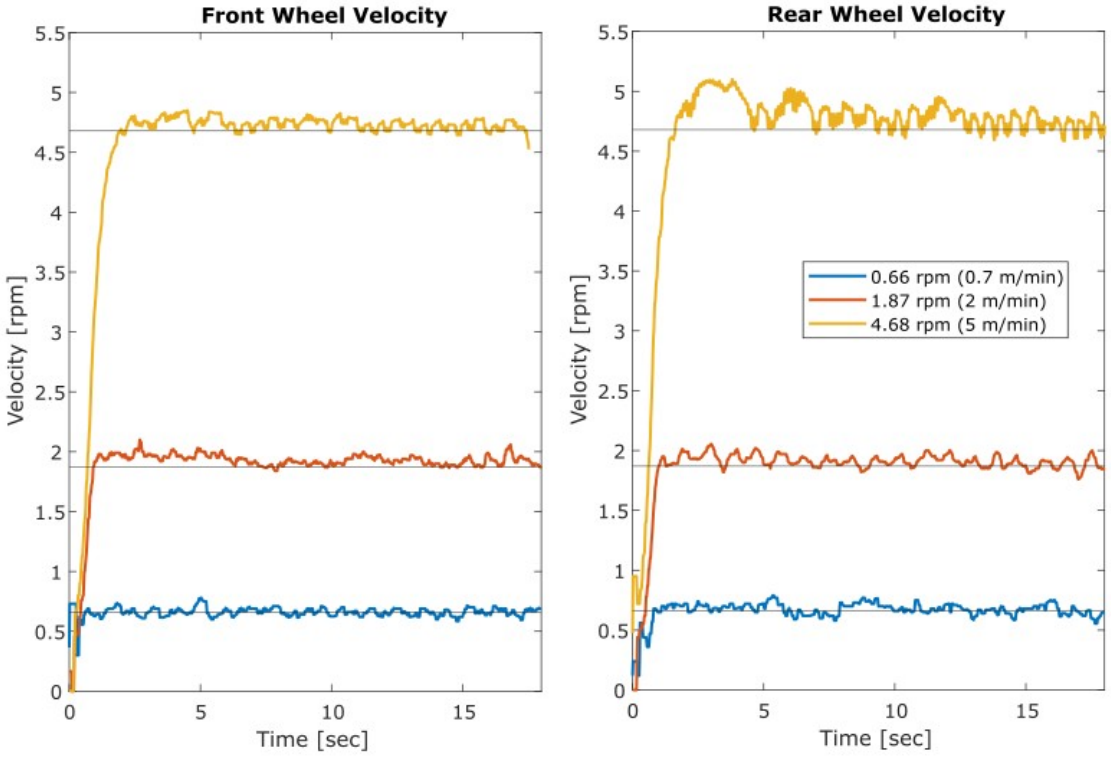

Chapter 7

Continuous Spiral Photogrammetric Image Network

7.1 Image Sequencing

Typical methods of collecting images for photogrammetric analysis, whether in tunnels or other general areas, is a uniform grid-wise approach. The previous approach by Bradley Engineering Ltd. (BE), as described in Section 2.1, navigates a single camera through the cylindrical grid in a stationary and incremental sequence to create this grid. The resulting camera path can be seen in Figure 7.1, showing the variation of a dual-camera system completing half rotations at each stage. This incremental approach of stopping at each lengthwise station and capture angle during the rotation imposes significant delays in the process. Stopping at each angle to capture an image includes the additional time to slow down the arm, pause for the camera to settle and capture the image (t_{Cap}), and accelerate back to speed. The parameter t_{RotAdv} encapsulates the net time to rotate between each capture angle and n defines the number of images per rotation. Stopping to manually move the rig to the next capture station and begin another rotation consumes significant time, ($t_{StatAdv}$). The general equation for the time to complete one full station (t_{Inc}) is defined in Equation 7.1 below.

$$t_{Inc} = n(t_{RotAdv} + t_{Cap}) + t_{StatAdv} \tag{7.1}$$

Figure 7.1: Piece-wise image sequence camera paths, black and green differentiating each camera.

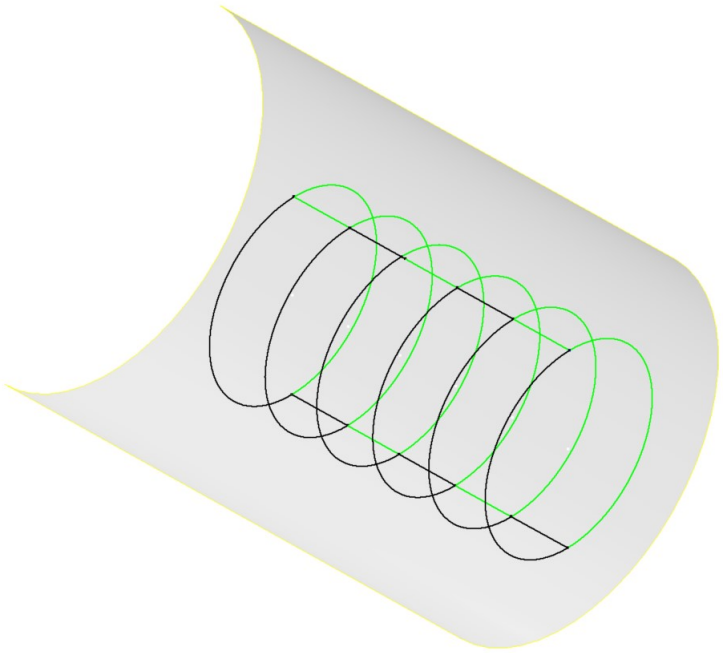

$$t_{StRot} = t^*_{Rot} + t_{StaAdv} \tag{7.2}$$

The most obvious way to improve this method is to avoid the need for stopping at each capture angle throughout the rotation. This means capturing images while the camera is in motion, which imposes additional constraints not present when the camera is stationary; these are detailed in Section 7.3.2. The improved time required to complete one station using this modified approach (t_{StRot}) is defined in Equation 7.2. The camera-limited rotation speed defines the time required to complete a full rotation at constant speed (t^*_{Rot}). t^*_i indicates that the particular parameter is affected by the defined constraints of capturing while in motion.

Capturing images during rotation while stationary does not require significant alter-

Figure 7.2: Continuous image sequence camera paths, purple and green differentiating each camera.

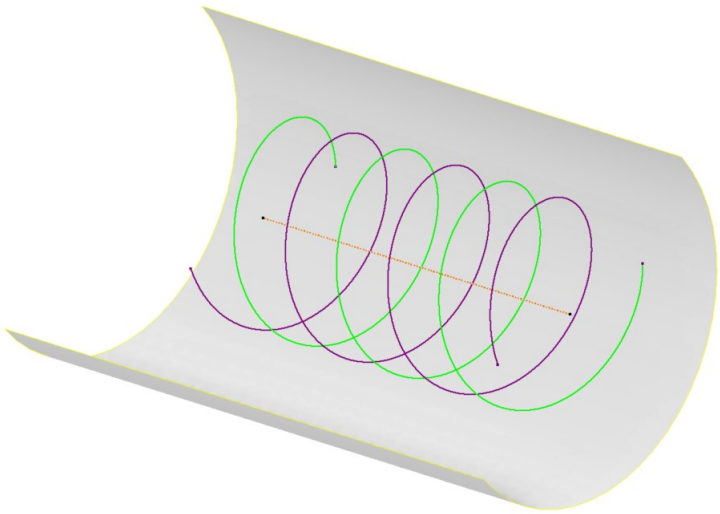

ations to the process, maintaining the piece-wise path shown in Figure 7.1. However, taking the capture while in motion one step further to include continuous capture and rotation while moving along the length of the tunnel, changes the sequence of moving between images completely. The continuous capture results in a spiral like sequence as shown in Figure 7.2. The delays contributing to the time required to complete one stage (rotation and linear advance) are significantly reduced in this method as it becomes continuous throughout, termed t_{Cont} and defined in Equation 7.3. Expanding on the constraints imposed from continuous rotation, additional motion blur details are discussed in Section 7.3.1. The linear advance time is matched to the rotation time to ensure the cameras are at the same clock location when the correct linear advance is made.

The length of the Automated Tunnel Inspector (ATI) arm and therefor the radius of the camera path set the distance between the camera and the surface. This parameter is a function of the desired Ground Sampling Distance (GSD), the tunnel diameter dimension, and the camera's focal length. These parameters also alter the surface coverage captured within each image, subsequently changing the possible advance

between images. However as outlined in Section 1.3.2, adjusting these parameters for more optimal or alternative properties was not part of this work, and a predefined distance between the camera and surface was set to 2 m to provide the target GSD with the set equipment.

$$t_{Cont} = t^*_{StRot} = t^*_{StatAdv} \tag{7.3}$$

Advancing to this continuous spiral image capture sequence was possible as the systems are fully actuated. The avoidance of pauses and delays in the sequence allows for the most efficient image capture process via automated equipment.

7.2 Image Density

The image density (defined as κ) has been defined as the number of images that capture a single point, and is critical for ensuring that the quality of the resulting photogrammetric model is maintained. For an image network of a single orientation and a uniform image grid, the average image density is calculated based on the linear and rotational advances between successive images in the respective directions as shown in Equation 7.4. This can alternatively be related to the image Overlap (OL) as the complementary percentage to the image advance.

$$\kappa = \frac{100}{\%Adv_{Lin}} \times \frac{100}{\%Adv_{Rot}} = \frac{100}{100 - \%OL_{Lin}} \times \frac{100}{100 - \%OL_{Rot}} \tag{7.4}$$

The simple linear grid that a piece-wise sequence creates decouples the linear and rotational OL of images. Modifying the image capture sequence to the continuous spiral alters the resulting image grid network, resulting in a skewed grid around the tunnel. The grid that results from the continuous image sequence outlined above

resembles that with the center of captured images as displayed in Figure 7.3, which shows the result for an example image network of a 35 m long section of a 7.5 m diameter tunnel being captured with a rotational and linear OL of 80% and 60% respectively.

Figure 7.3: Camera capture locations on flattened surface projection for the example image network.

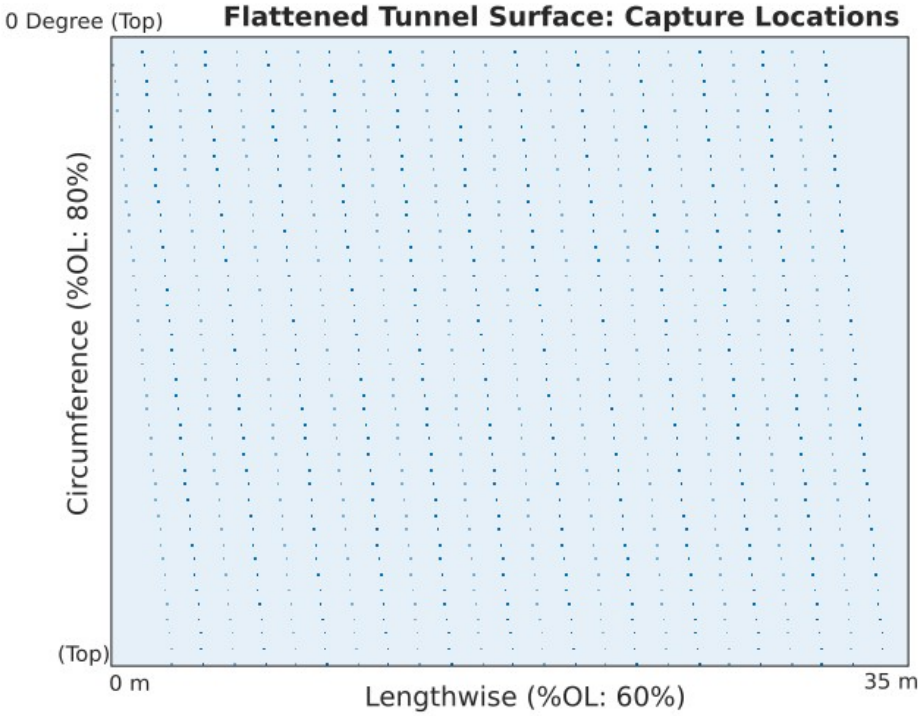

Although the layout of the resulting grid is altered, the relationship between the defined image OL and resulting image density is maintained. Figure 7.4 displays a heat map of the resulting image density for the same example image network displayed above; The figure shows the full frame of the tunnel surface over the example range, with further details of the image density pattern through an extracted section of consistent capture. Extracting this section allows for the image density to be explored, identifying the minimum, maximum, and average density values. Visualizing the outcome in this form helps to identify patterns of fluctuating density or pockets of outlying densities which may arise from the overlaps or orientation

variations present.

Figure 7.4: Image density heat map on a flattened surface projection for an example image network.

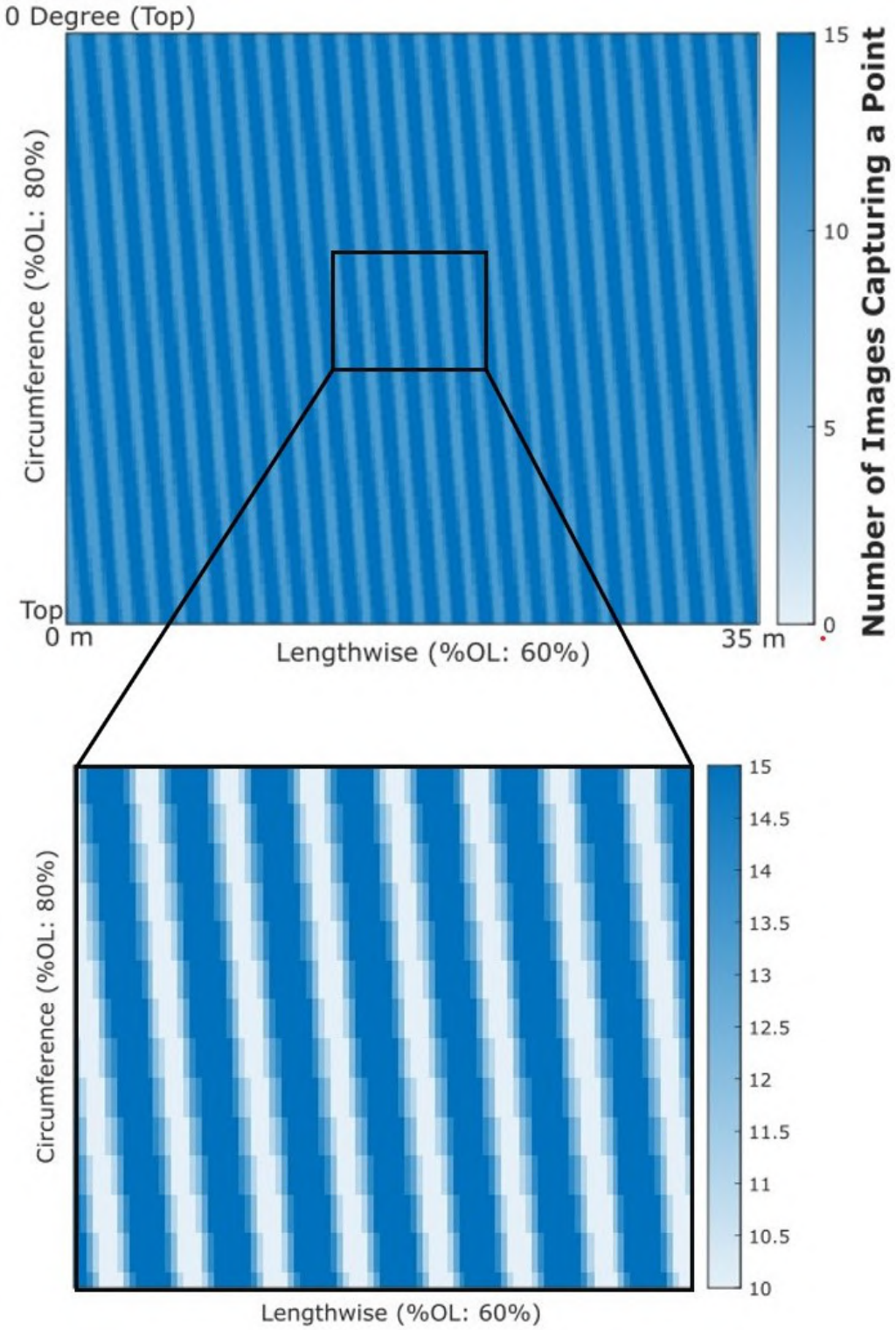

A prominent waveform pattern in the direction of motion appears in the resulting heat map as a symptom of the overlaps applied. Due to the linear advance (40%) not being an even factor of the lengthwise dimension of an image. This is not prevalent in the rotational direction as the advance (20%) evenly captures the rotational dimension of an image. Varying the OL in each direction can alter the possible collection speed and impact the photogrammetric analysis. Analysing and comparing data from these image density heat maps can be used for identifying the ideal OL combination and orientation sequence for a particular tunnel.

7.3 Continuous Image Capture Rate Analysis

7.3.1 Motion Blur Limitation

The capture of images while moving imposes an additional element of complexity that must be accounted for when collecting images within the tunnel. The motion of the camera creates risk of induced blur in the images; motion of the camera has the same effect as motion of an object within the camera's view. There is an allowable amount of motion that can be observed without blur being seen in the image. The motion is in terms of the number of pixels moved while the shutter is open, and the flash is active. Transforming this relationship into physical terms to be related to the tunnel is a function of the GSD and the active shutter or flash speed; the faster of the two is the image exposure rate, $\nu_{Exposure}$, as shown in Equation 7.5.

$$\nu_{Blur} = \frac{\text{GSD} * \delta_{Pixel}}{\nu_{Exposure}} \tag{7.5}$$

The GSD refers to the size of a pixel at the surface [mm/pixel], the $\nu_{Exposure}$ is listed in fractions of a second of exposure [seconds/exposure], and ν_{Blur} is the resulting

velocity limit in mm/second. The parameter δ_{Pixel} is the quantity of pixels allowed to move during exposure to avoid blur [pixels/exposure]; as a rule of thumb, this is half of the GSD. This velocity relates to the velocity of the image on the surface itself and therefore when compared to motion speed of the ATI system, results in the magnitude of the combination of the ATI's linear drive velocity and tangential velocity of the rotational arm translated to the tunnel surface as defined in Equation 7.6. The parameter ν_{ATI} defines the linear velocity of the ATI system, ω_{AR} is the rotational velocity of the ATI arm, r_T is the radius of the tunnel, and ν_{IMG} is the resulting magnitude of the net image velocity as projected to the surface.

$$\nu_{IMG} = \sqrt{\nu_{ATI}^2 + (\omega_{AR} * r_T)^2} < \nu_{Blur} \tag{7.6}$$

Equation 7.7 defines the ratio between linear velocity and rotational velocity translated to surface ν_{Ratio}, which relates the linear displacement of the ATI while the arm makes one complete rotation ($\delta_{Lin/Rot}$) with the projected circumferential surface displacement of the images throughout that rotation ($2\pi r_T$). Maintenance of this relationship is critical for ensuring the spiral camera path and required OL between successive images are obtained.

$$\nu_{Ratio} = \delta_{Ratio} = \frac{2\pi r_T}{\delta_{Lin/Rot}} \tag{7.7}$$

7.3.2 Image Capture Rate Limitation

In addition to the direct limitations on the physical motion speed of the cameras, additional constraints are placed on the Image Capture Rate (ICR) due to aspects of the photography system and the orientation actuation. The fastest allowable ICR as defined in Equation 7.8 becomes the minimum rate as constrained by the

orientation of the cameras and the performance of the flashes as detailed in the following sections. The FRR_{max} is the maximum allowable flash refresh rate as detailed in Section 7.3.2.1 and ICR_{Orient} is the minumum time require to change orientation as defined in Section 7.3.2.2. The resulting capture rate subsequently imposes a constraint on the overall arm rotation, which varies with the number of images required per rotation or the resultant angle between successive images as defined in Equation 7.9.

$$ICR_{Limit} = min(FRR_{max}, ICR_{Orient}) \tag{7.8}$$

$$\omega_{ICR} = \frac{\phi_{inc}}{ICR_{Limit}} \tag{7.9}$$

7.3.2.1 Flash Refresh Rate

As each camera has a set of two flashes that operate at close to full power to provide sufficient lighting for the images, image capture frequency significantly affects the power consumption and life cycle of these flashes. As the frequency of image capture increases, the risk of overheating these flashes increases as well. Although the flashes have built in over-temperature protection that slows down the recycle time up to ten seconds to compensate for the heat produced [19], if a fast flash rate is sustained for an extended period, the Flash Refresh Rate (FRR), the rate at which the flash can take successive images, will be automatically reduced, or completely halted for a period of cool-down. The flashes used were the AD400Pro from GODOX© Photo Equipment Co. Product manual documentation lists the number of flash actions that will activate over-temperature protection for a particular output power; at an output power of $1/4^{th}$ of full power (originally estimated as the required flash power

for capture in Grand Falls), is 200 flashes [19]. However, the rate that is deemed "fast succession" is not specifically defined in the documentation.

To identify an acceptable capture rate that would allow the flashes to continuously operate at that rate without any deviance in the flash performance, experimental tests were conducted. Capturing images for extended periods of time at differing capture rates allowed for the performance of the flashes to be monitored. Table 7.1 summarizes the information collected from four tests, which provided an acceptable rate estimate for initial implementation. Although there is room for determining an exact critical rate as the flashes did not experience any overheating at a rate of five seconds, their operation limit was reached shortly after 200 images were captured at a rate of four seconds. A conservative decision to use a minimum capture rate of five seconds was concluded to ensure this would not be a source of downtime during the operations.

Table 7.1: Flash Refresh Rate Test Results

Test	Capture Rate (sec)	Images	Over-Temperature Protection Activated?
1	6.0	∞	No
2	5.0	∞	No
3	4.0	~ 250	Yes - Soft stop: flash recycle time increase
4	3.3	200	Yes - Full stop: flash halted for cool-down

7.3.2.2 Orientation Change Timing

If orientation changes are desired during the continuous capture and rotation, the time required to perform that operation is considered as an additional constraint on the capture rate. A single orientation change throughout the continuous operation limits the complete operation due to the constant velocity throughout the entire rotation. The possibility of slowing down between the images where the orientation change is required and moving faster elsewhere was considered. However it was

deemed to be not feasible or reliable enough to synchronize such a frequent and important change between the arm rotation, wheel speeds, orientation actuators, and cameras within the framework of this project.

The constraint due to the orientation changes is defined in Equation 7.10, where ω_{Orient} is the rotation speed of the actuator in degrees per second, considered with the predefined 90° rotation required to toggle between portrait and landscape. The actuators utilized have a rated speed of 12° per second, which allows for a 90° orientation change to be completed in 7.5 seconds [23]. After testing these actuators, noticeably quicker speeds were possible and dependent on the drive controller implemented.

$$ICR_{Orient} = Time_{Orient} = \omega_{Orient} * 90^{\circ} \tag{7.10}$$

Chapter 8

Implementation at the Grand Falls Hydroelectric Generating Station

8.1 Grand Falls Generating Station Overview

The powerhouse at the Grand Falls Generating Station (Grand Falls) houses four Francis turbines with a total capacity of 66 MW. Water is diverted to this station from the Saint John River through an intake tunnel running under the town center. This tunnel is approximately 920 m in length, consisting primarily of an 822 m long concrete lined section with the remaining length attributed to shorter steel-lined sections at the intake, distribution, and penstock regions.

This station typically operates on a four-year shutdown cycle for inspection and general maintenance of the tunnel and powerhouse facilities. This instance of the cycle was extended to five years due to COVID-19 restrictions. Visual walkthrough inspections have been the primary method of inspection for decades and continue to be conducted to identify current defects and areas for caution or immediate repair. The first photogrammetric scan of this tunnel was completed by Bradley Engineering Ltd. (BE) in 2017 [5]. This scan captured about 5,000 images over 7 days using the Tunnel Inspection Assistant (TIA) system and methodology as described in Section

2.1. These images were captured at a visual resolution of 2mm with 80% rotational and 60% longitudinal Overlap (OL) [5]. The details and experience of the updated scan completed this year is discussed within this chapter.

8.2 Acquisition Process Discussion

Although the precise date was unknown from the origin of this project, the project timeline was inversely developed to have the Automated Tunnel Inspector (ATI) system fabricated and tested in time to complete the image acquisition of the Grand Falls intake tunnel during the scheduled shutdown in 2022.

The complete duration of the trip to Grand Falls spanned over nine days (September 8^{th}–16^{th}), with the site being open for work six days per week (Sundays off), for ten-hour days (7:00am-5:00pm). The nine-day trip was reduced to just over six days of available work due to the Sunday off and a collection of setbacks. It began with NB Power experiencing difficulties dewatering the tunnel delaying the initial access to the tunnel by over a day. An unexpected thunderstorm during the week made access to the tunnel unsafe forcing an additional loss of over half of a day. This time frame considers the time from equipment being unloaded from the transport van into the tunnel to the time it was extracted and repacked to return home. The general timeline for a typical work day has been outlined in Table 8.1. The general tailboard meetings, safety discussions, and uncontrollable time spent waiting for entrance to the tunnel allowed for approximately seven working hours in the tunnel per day, which were broken into two sessions. Actual scanning time was further reduced due to the daily set up and tear down of camera equipment and preparation of the ATI.

The first working day consisted of unloading equipment from the van into the tunnel through a manually worked rope hoist, assembling, and wiring of the ATI within

Table 8.1: Work Day Itinerary Breakdown

Time	Activity	Description
7:00-8:30am	Daily Preparation	General tailboard and preparations
8:30-11:45am	Operational Time	ATI set up and scanning
11:45am-12:45pm	Lunch Period	Lunch and safety
12:45-4:30pm	Operational Time	ATI scanning
4:30-5:00pm	Extraction	Equipment and personnel exit tunnel

the tunnel, setting up and preparing the camera equipment and an initial test of the assembled actuations and cameras. This process primarily required three persons, with the assistance of onsite workers operating the hoist; one person taking components from the truck to the hoist, and two persons collecting the components and assembling the ATI approximately 25 meters upstream from the hoist location. Figure 8.1 shows the ATI being assembled with reference of the hoist location in the background. The ability to bring and set up equipment in the tunnel through the main access port simplified the process compared to the special treatment that was required to transport TIA into the tunnel in 2017; validating a benefit of the new modular design of the ATI. To avoid leaving equipment laying on the muddy tunnel surface for extending periods of time, components were lowered in a logical and orderly sequence that optimized the assembly process. Base components (wheels and base frame parts) were delivered and assembled first, then while these were being assembled the inner and outer boom components were delivered and assembled separately before being added to the base frame. The arm, outriggers, and electronic components were then assembled completing the main set up of the ATI. The final step being the attachment and set up of the camera equipment including two cameras and four flashes. These latter components were removed from the tunnel at the end of the day to avoid the risk of any damage from moisture or humidity. Simultaneously with the set up procedure, surveyors were identifying locations for monuments to be drilled and placed at set distances along the tunnel, which had to

Figure 8.1: ATI assembled upstream from equipment hoist location.

be done before image collection could begin.

The second day on site presented the opportunity for actual scanning which began

after a morning of testing and troubleshooting. As this was the first time setting up and operating within the actual tunnel environment, behavior on the muddy, slippery, and rough tunnel surface was thoroughly tested before confidently beginning the actual scanning process. Complete scanning began and proceeded steadily for approximately four and a half working days. Much of this process was smooth and minimal interjections or interrupts were experienced, however, some locations within the tunnel required additional attention. A number of locations along the tunnel had hose-like sprays spouting from the top or sides of the tunnel which were to be avoided if possible, to protect the camera equipment. Figure 8.2 shows an example of these sprays and an approach used to avoid them. One section stood out as worse than

Figure 8.2: Example of water sprays within tunnel.

(a) Water spray and deterrent method.

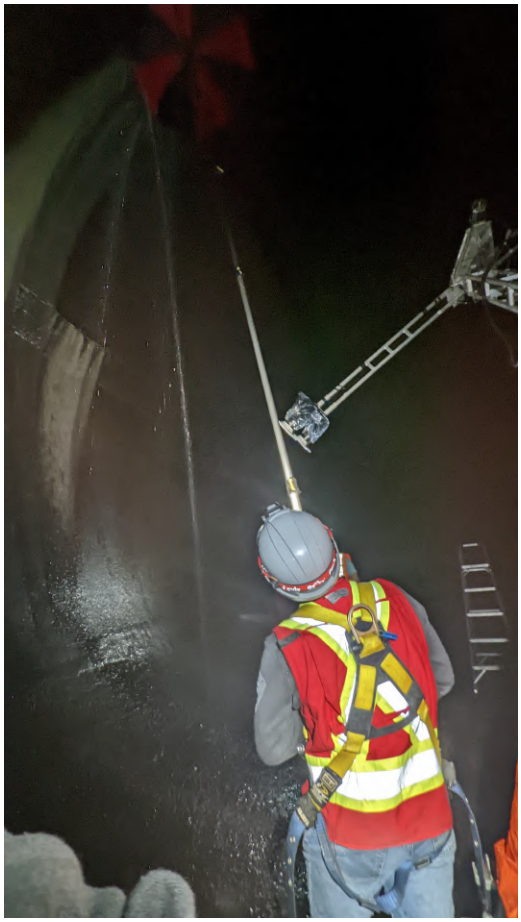

(b) Close up of spray source.

the others for a number of these sprays were collected in a single location; it was referred to as the "car wash" location. In many cases, risk of water contact with photography equipment could be mitigated by using extended umbrellas to divert the sprays away, while other cases required alteration to the spiral scan sequence. In those cases, the spiral would be brought as close to the spray as possible, then a stationary rotation scan was done, before incrementing to the other side of the spray and performing another stationary rotation. This would ensure as many images were captured around these locations as possible with sufficient OL, while still mitigating water contact with the cameras. Concerns of water contacting the ATI itself were minimized with sealed enclosures over the electronics and loomed wiring, however it was still to be avoided as much as possible. A tarp was added to cover the entirety of the base and majority of the lower boom for additional security and to allow for extra items and equipment to be safely carried on the base platform.

In addition to the presence of water, rough terrain at the invert of the tunnel required cautious attention throughout. Even though the tunnel had been dewatered for the shutdown, a steady stream approximately five centimeters deep was consistently flowing through the tunnel. Within this, the surface had a steady yet wavering groove traveling the length of the tunnel as well as a collection of defects and potholes upwards of five to ten centimeters deep that a wheel could fall into. For the most part, these were avoided if noticed, however it was not uncommon for a wheel to drop into one of these. While this may cause some jerking or skewing of the ATI, it had no issues driving back out and was therefore not a significant problem. However, one section of the tunnel was found to have a very large portion of the concrete missing, being appropriately referred to as the "gorge" (see Figure 8.3). It was slightly offset from the center of the invert and rectangular in shape measuring approximately 2.5 m long, 0.75 m wide, and over 0.5 m deep - reaching the top of a typical rubber boot when stepped into. The width of this hole was too large to straddle between

Figure 8.3: Gorge - large pothole defect at the invert of the tunnel.

a front and back wheel while driving straight. It was possible to straddle it while translating in a skewed orientation, however this would drastically affect the plane of the cameras and not allow for reliable capture. To effectively perform a spiral scan over this section, wooden planks were placed across the gorge in front of the rear wheel in a "leapfrog" method. This allowed the ATI to travel over the hole while still capturing images of the gorge and surrounding areas consistently. Scenarios like this are a prime example of the extreme complexity with fully automating the motion of

the ATI in these types of environments.

At the end of the main tunnel section the tunnel sharply bends upwards towards the intake, referred to as the "elbow" (see Figure 8.4). This section is a steep, steel-lined curve and has a large amount of water spray. This area was omitted in the 2017 scan. The ATI was able to drive up a portion of the slope to extend the spiral sequence; ropes and anchors were used as an additional safety measure. This concluded the ATI scanning task; additional sets of images of this elbow were capture with a tripod and mast, but the presence of water limited the quality of images in this area. While the tripod was being used, the ATI was driven towards the tunnel entrance. Scaffolding was put in place for maintenance around 100 meters from the tunnel entrance and therefore, the ATI had to be disassembled and extracted from that point. The disassembly and removal of equipment was done in a similar sequence to the assembly. This elbow portion and extraction of the ATI consumed the final day of the on-site work.

Figure 8.4: Elbow at intake end of the tunnel.

8.3 Results and Comparisons

Since the first scan in 2017, the abilities of the photogrammetric analysis performed by BE have steadily improved the former methods and technologies which now allows for images to be captured at a resolution of 0.4 mm for these tunnels. This requires a camera-surface distance of 2 m. This camera offset combined with the desired 80%/60% image OL and other properties of the photography system resulted in the choice of 52 images per rotation. The Image Capture Rate (ICR) as defined in Section 7.3.2 was set to 5 seconds due to the most critical limitation imposed by the flash refresh time. Collecting this number of images at that rate sets the rotational speed to 1.34 degrees/second results in a total rotation time of 4.5 minutes.

Using a dual camera system allows for twice the linear advance to be made during one complete rotation as same-angle images will be captured by opposing cameras every half rotation. Synchronizing the linear advance (40%) with the timing of the rotation sets the linear speed of the ATI to 0.67 m/min. At this rate, the 822 m section of the tunnel was estimated to require approximately 23 hours of scanning time assuming perfect efficiency; this turned out to be a reasonably accurate estimation considering the delays and interference with the ability to scan that slowed the overall process at times. A similar estimation for the ATI to perform a scan of similar quality and resolution to the scan conducted in 2017 shows a total required capture time of 7 hours. While this assumes ideal efficiency and does not include the time for set up and any site interruptions throughout the day as described earlier, a drastic improvement from the approach taken in 2017 is evident.

Table 8.2 summarizes the key differences and improvements between the scan performed by the ATI and the previous scan in 2017. At the end of the scan, a total of approximately 28,000 images were captured throughout the tunnel, drastically higher than the number of images captured previously. While the sequence was

Table 8.2: Grand Falls Tunnel Scan Comparison

	2017	**2022**
Overlap	80%/60%	80%/60%
Number of Images	∼5,000	∼28,000
GSD	1.3 mm	0.4 mm
Camera	Canon 6D	Sony α7R III
Camera Resolution	20.2 MP	42.4 MP
Lens Focal Length	20 mm	21 mm
Camera-Surface Distance	5 m	2 m
Scan Time	7 days	4.5 days

completed with the same linear and rotational OL, the increased resolution and smaller camera-surface distance provide the explanation for the significant increase in images required to capture the same tunnel. Collecting such a large number of images, at a higher resolution and in a shorter time period demonstrates the advantages of the new ATI system and the continuous spiral sequence developed. Figure 8.5 shows a long exposure photo of the ATI during the scan of the tunnel, this image records a 180 degree rotation of each camera. Figure 8.6 shows an example of the details captured within this scan through an extraction of the model created from this can of the Grand Falls tunnel.

Figure 8.5: Long exposure photo of the ATI scanning the tunnel.

Figure 8.6: Snapshot of model created from the images captured during this scan.

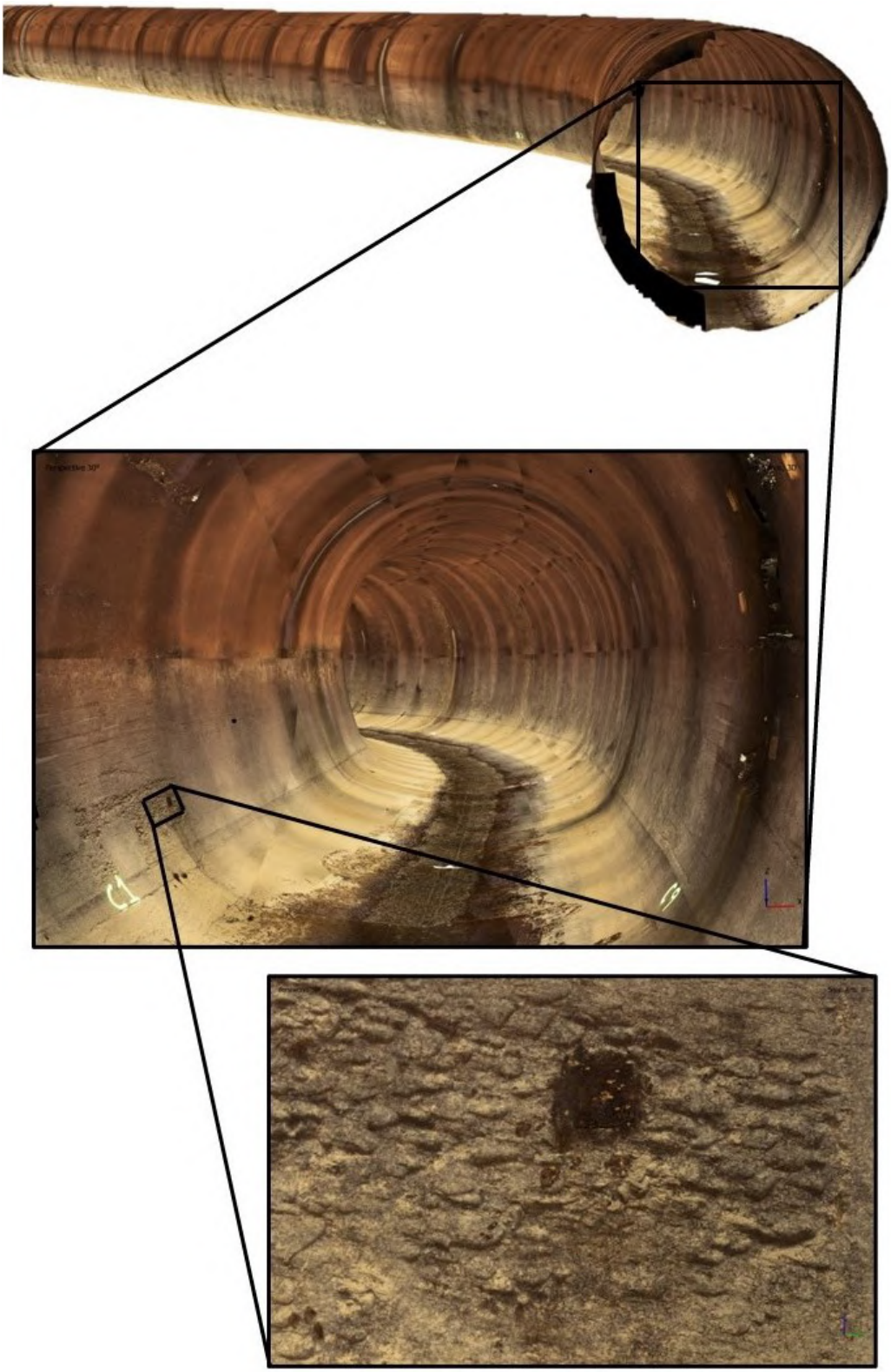

Chapter 9

Conclusions and Recommendations

A mobile semi-autonomous robotic image collection vehicle was developed to improve the data acquisition phase of the previous photogrammetric inspection process of hydroelectric tunnels. Previous image collection methods for photogrammetric analysis as studied in the Grand Falls Generating Station (Grand Falls) intake tunnel and Mactaquac Generating Station penstocks are primarily manual, tedious, and inflexible processes. The primary limitations identified in the process are:

- a tunnel specific design of the assistive inspection rig does not adapt to different or varying tunnel diameters,
- the image collection sequence is inefficient requiring significant time and manual effort,
- the construction and assembly of the assistive rig poses difficulty in accessing tunnel areas.

The collection of high quality images for photogrammetric analysis provides significant benefit to the management and maintenance of the infrastructure. However, the limitations identified in the previous methods make collecting images a time consuming and laborous process that also restricts the applicability of the photogrammetric

inspection for different tunnels. The method has significant inefficiencies as a result of the sequence that images are captured and the control of the equipment used to do so. The duration of tunnel shutdowns are minimized as halting energy production is a considerable expense; an inefficient image collection process can consume an excessive portion of the shutdown time and potentially interfere with maintenance and rehabilitation operations.

The primary goal of this work was to improve operations during the data acquisition phase of the photogrammetric inspection process for hydroelectric tunnels with the hope of identifying a data acquisition system that is best suited to improve the efficiency of the photogrammetric data collection process in a tunnel while taking transportation and the variability in tunnel diameter into consideration. Attaining this goal involved the development of an advanced semi-automated camera positioning system, the optimization of the image network to improve collection process efficiency, and the evaluation and demonstration of advanced control techniques in these unique environments. These goals led to the new data acquisition process and ATI being successfully implemented in the Grand Falls intake tunnel.

9.1 Conclusions

A semi-automated camera positioning system, referred to as the Automated Tunnel Inspector (ATI), was designed and developed to address a set of limitations identified in the data acquisition process of photogrammetric inspections in hydroelectric tunnels. ATI utilizes a variety of electromechanical components and control techniques to drive and automate elements of the image collection process. The ATI design is capable of adapting to tunnel diameters between 4.5 m - 9 m and maintaining consistent image capture parameters at any variation. Modification of the camera

to surface distance can be used to vary the image resolution and alter the total scan procedure. The ATI allows for complete driven mobility including pure translation or rotation for effective reorientation and alignment within the tunnel environment. This design was conceived from an extensive comparison and evaluation amongst various other concepts for collecting images.

The model quality constraints, photography equipment properties, and photogrammetric parameters formed the basis for the required image capture parameters throughout the tunnel. A unique spiral image network was developed that allowed the full potential of the ATI to be utilized by facilitating continuous image capture while rotating and driving along the tunnel. This sequence eliminated any idle time that creates inefficiencies in the process that had been observed in the previous, more incremental capture sequences. The rate of capture limits were quantified based on the motion limit to avoid blur in the images, the refresh rate of the flashes, and the time required to change orientation, all of which vary depending on tunnel and photogrammetric parameters. This analysis optimizes the rate of capture of the continuous approach and promotes efficiency in the collection process.

The ATI system was effectively developed to facilitate camera positioning and image capture in a wide range of tunnel diameters and profiles. The ATI's capabilities and performance was demonstrated in the Grand Falls intake tunnel over a period of six days, involving four and a half days of consistent operation. The modular design allowed all equipment and components to be transported into the tunnel through the main access port without the need for special consideration or additional assistance. Over 28,000 images were captured throughout the 822 m concrete-lined tunnel at a ground sampling distance of 0.4 mm. This resolution and number of images would not have been possible without the advancements of the ATI which significantly reduced the manual effort and time required to perform the image collection.

In the process of development and implementation of the ATI, advanced closed loop control techniques, including various PI-based and model predictive control schemes have been formulated and assessed in a unique and challenging environment on this large scale robotic system. This process particularly demonstrated the robustness of MPC systems for handling complex tasks while also identifying the limitations of individual Single-Input-Single-Output (SISO) systems compared to Multiple-Input-Multiple-Output (MIMO) systems.

9.2 Recommendations

While the direct goal of this work is to make a significant improvements to a semi-automated system, this work can serve as a foundational element for future research in the pursuit of an autonomous ATI. The following sections identify recommendations for future areas of research that build on this work, how the ATI could be improved and continued to be used by Bradley Engineering Ltd., and how the industry as a whole can advance and move towards more wide-spread adoption.

9.2.1 Researchers

- Further research into localization within GNSS-denied, dark, featureless environments should be conducted to improve the accuracy and consistency of real-time localization within a tunnel to identify the complete pose of a vehicle in these challenging environments. This area of research is foundational for other automation related applications.
- Maintaining alignment of the ATI while moving throughout the tunnel required frequent steering adjustment and although fully automating this was outside of this project's scope, it stands as an aspect for significantly reducing the efforts

and attention required of the operator. Self-navigation of a three-wheeled vehicle in a generally cylindrical tunnel with the goal of maintaining centricity, alignment, and velocity would be a significant advancement in this aspect. This would include maneuvering in dynamic environments and involving object avoidance methods would be a key element to this.

- Obstacle detection and avoidance in dynamic environments has been studied in literature, however hydroelectric environments pose additional elements that may interfere with current methods. The rapid detection of moving water, whether in a stream form on a surface or projecting out of one, and obstacles within or obstructed by such water are not common in environments in which these studies are conducted. Research into this area is recommended for advancements in these environments, and applies to many other fields and applications as well.
- Although image collection for photogrammetric inspections was the primary influence on the design choices during this research, the system developed in this work provides a base for unique tools and attachments to be alternatively investigated. This could include the use of infrared cameras for thermal imaging or acoustic emissions technologies. These alternative additional technologies greatly expand the applications and industries to which this system can apply.
- The control systems for each portion of the ATI were created as different configurations of SISO systems. Further research into the system identification of MIMO systems would formulate a more optimal control scheme, particularly in the case of the model predictive control of the drive system.

9.2.2 Bradley Engineering Ltd.

- Refinement of the structural member fabrication as well as integration of hardware for improved reliability and to extend the expected lifespan of the equip-

ment. A more industrial and standardized system will ease the deployment process and benefit the commercialization of the system.

- Improve the interface for controlling the ATI to a more intuitive and sophisticated graphical user interface to enhance the reliability and user experience. A more responsive interface will make the ATI easier to control and less prone to unintended inputs and errors.
- Optimize the assembly and disassembly procedure to minimize the time required for mobilization. This could involve modified configurations of subassemblies, alternative materials or hardware, or exploration into quick-connect components or joints.
- Perform additional image acquisition procedures with the ATI in other tunnels with different characteristics to further validate the adaptability and efficiency of the system in real environments.
- The implementation of alternative flashes with a higher flash refresh rate should be explored to increase the attainable rate of image capture. Advanced flashes could be acquired in the consumer market or independently developed for this application.
- The power source from elements of the photography systems should be integrated into the main ATI power supply to reduce the number of independent sources and reduce time spent swapping and charging individual batteries.
- Quantify the value of the ATI system for different use-cases and varying parameters from a commercialized business perspective. Evaluating the balance between image resolution and resulting model quality against the time that is required to perform the corresponding scan.

9.2.3 Industry

- The inspection data that advanced capture methods are able to collect significantly expands the attainable knowledge of tunnel operators and owners. Industry partners should consider exploring and regularly implementing advanced data collection technologies to improve the inspection practices for their assets.
- Literature relating to data collection technologies for hydroelectric tunnels has expanded in recent years, however it remains limited in quality and applicability. Academics, industry professionals, and asset owners are encouraged to continue employing collaborative efforts to advance inspection technologies in this field; including performing experiments and studies, and publishing their work to enhance the collective knowledge base.
- Industry standards and common practices should be continuously updated to account for advanced technologies to ensure the collective growth of the entire hydroelectric tunnel inspection industry. The residual impact on hydroelectric infrastructure maintenance and safety directly benefit from these updates as well.
- The growing demand and improving technologies indicate and evolutionary future for methods and technologies of automated capture of tunnel inspection data. As new and improved techniques for utilizing the captured data expand, the demands of high quality data is likely to drive the innovation of data collection methods; complete autonomous capture, practical implementation of UAVs when the technology is capable, and integration of technologies and inspection data such as photogrammetry and lidar, are potential branches that could stem from the current state of tunnel inspection methods.

Bibliography

[1] ASI Group, *Remote Inspections Surveying*, **1**, no. 905, 4–9.

[2] K Astrom and T Hagglund, *Pid controllers: Theory, design, and tuning*, 2nd ed., Instrument Society of America, 1995.

[3] Zafer Bingul and Oguzhan Karahan, *Dynamic modeling and simulation of stewart platform*, Serial and Parallel Robot Manipulators (Serdar Kucuk, ed.), IntechOpen, Rijeka, 2012.

[4] Dorit Borrmann, Andreas Nüchter, Marija Dakulović, Ivan Maurović, Ivan Petrović, Dinko Osmanković, and Jasmin Velagić, *A mobile robot based system for fully automated thermal 3D mapping*, Advanced Engineering Informatics **28** (2014), no. 4, 425–440.

[5] Cody Bradley, *Photogrammetric modelling of the grand falls hydroelectric generating station*, 2018, pp. 496–505.

[6] Cody Bradley, Lloyd Waugh, and Glen Hanscom, *Photogrammetric modelling of the grand falls hydroelectric generating station*, CSCE General Conference 2018, Held as Part of the Canadian Society for Civil Engineering Annual Conference 2018 (2018), 496–505.

[7] ———, *Advanced dam inspections with photogrammetric modelling*, Canadian Dam Association Conference (2019).

[8] Cambridge, *Cambridge academic content dictionary*, Cambridge, 4 2017.

[9] Bob Clarke and Rick Fletcher, *Surveying a Tunnel Using an ROV Monitoring of tunnel condition Objectives of ROV inspection*, (2016), no. May 2013, 1–8.

[10] Wikipedia contributers, *List of hydroelectric power stations in Canada*, 2021, [Online; accessed 01-December-2021].

[11] Wikipedia Contributors, *Pid controller*, 11 2022.

[12] John J Craig, Pearson Prentice, and Pearson Prentice Hall, *Introduction to Robotics Mechanics and Control Third Edition*, (2005).

[13] R. Dubay, *Self-optimizing mpc of melt temperature in injection moulding*, ISA Transactions **41** (2002), 81–94.

[14] Mehrdad Ehsani, Yimin Gao, Sebastien E Gay, and Ali Emadi, *Modern electric, hybrid electric, and fuel cell vehicles: Fundamentals, theory, and design*, CRC Press LLC, 2005.

[15] A. Ellenberg, L. Branco, A. Krick, I. Bartoli, and A. Kontsos, *Use of Unmanned Aerial Vehicle for Quantitative Infrastructure Evaluation*, Journal of Infrastructure Systems **21** (2015), no. 3, 04014054.

[16] C Eschmann, C.-M Kuo, C.-H Kuo, and C Boller, *High-Resolution Multisensor Infrastructure Inspection with Unmanned Aircraft Systems*, Tech. report, 2013.

[17] Josep Maria Font and Joaquim A. Batlle, *Mobile Robot Localization. Revisiting the Triangulation Methods*, IFAC Proceedings Volumes **39** (2001), no. 15, 340–345.

[18] Yong Gao, Wu Wei, Xinmei Wang, Dongliang Wang, Yanjie Li, and Qiuda Yu, *Trajectory tracking of multi-legged robot based on model predictive and sliding mode control*, Information Sciences **606** (2022), 489–511.

[19] Godox, *Ad400pro product manual*.

[20] M. Hassan, R. Dubay, C. Li, and R. Wang, *Active vibration control of a flexible one-link manipulator using a multivariable predictive controller*, Mechatronics **17** (2007), 311–323.

[21] R. E. Heffron, *Underwater tunnel inspection by Virginia Power using a submersible robot*, (1989), 62766.

[22] Kazunori Hosotani and Hirofumi Yamamoto, *Free-Flow Tunnel Inspection Support Devices Aiming at Labor Saving of Visual Checking*, Journal of Robotics and Mechatronics **32** (2020), no. 4, 832–839.

[23] Optimal Engineering Systems Inc., *Hollow core motorized rotary stage*, 11 2022.

[24] Kazuto Kamiyama, Mikita Miyaguchi, Hiroki Kato, Toshimichi Tsumaki, Keisuke Omura, and Tsutomu Chiba, *Automatic Inspection of Embankment by Crawler-Type Mobile Robot*, jul 2018.

[25] Dov Katz, Jacqueline Kenney, and Oliver Brock, *How can robots succeed in unstructured environments?*, Robotics Science and Systems (RSS) Workshop on Robot Manipulation (2008).

[26] Nassim Khaled and Bibin Pattel, *Practical design and application of model predictive control*, Butterworth-Heinemann, 2018.

[27] Jingchao Li, Zhaohui Yuan, Sheng Dong, Xiaoyue Sang, and Jian Kang, *A learning-based model predictive control scheme and its application in biped locomotion*, Engineering Applications of Artificial Intelligence **115** (2022).

[28] Ronny Salim Lim, Hung Manh La, and Weihua Sheng, *A robotic crack inspection and mapping system for bridge deck maintenance*, IEEE Transactions on Automation Science and Engineering **11** (2014), no. 2, 367–378.

[29] Romulo Goncalves Lins and Sidney N. Givigi, *FPGA-Based Design Optimization in Autonomous Robot Systems for Inspection of Civil Infrastructure*, IEEE Systems Journal **14** (2020), no. 2, 2961–2964.

[30] Romulo Goncalves Lins, Sidney N. Givigi, Arthur D.M. Freitas, and Alain Beaulieu, *Autonomous Robot System for Inspection of Defects in Civil Infrastructures*, IEEE Systems Journal **12** (2018), no. 2, 1414–1422.

[31] Romulo Goncalves Lins, Sidney N. Givigi, and Paulo Roberto Gardel Kurka, *Vision-Based Measurement for Localization of Objects in 3-D for Robotic Applications*, IEEE Transactions on Instrumentation and Measurement **64** (2015), no. 11, 2950–2958.

[32] Romulo Gonçalves Lins, Sidney N. Givigi, and Paulo Roberto Gardel Kurka, *Velocity estimation for autonomous vehicles based on image analysis*, IEEE Transactions on Instrumentation and Measurement **65** (2016), no. 1, 96–103.

[33] Araki M, *Pid control*, 2009, pp. 58–79.

[34] Maplesoft, *Maple 2022*.

[35] MATLAB, *version r2021a*, The MathWorks Inc., Natick, Massachusetts, 2021.

[36] R Montero, J G Victores, S Martínez, A Jardón, and C Balaguer, *Past, Present and Future of Robotic Tunnel Inspection*.

[37] Iñigo Moreno-Caireta, Enric Celaya, and Lluís Ros, *Model predictive control for a mecanum-wheeled robot navigating among obstacles*, vol. 54, Elsevier B.V., 7 2021, pp. 119–125.

[38] Norman S. Nise, *Control systems engineering*, 6th ed., Wiley, 2011.

[39] Navid Nourani-Vatani, Jonathan Roberts, and Mandiam V. Srinivasan, *Practical visual odometry for car-like vehicles*, Proceedings - IEEE International Conference on Robotics and Automation (2009), 3551–3557.

[40] Tolga Ozaslan, Giuseppe Loianno, James Keller, Camillo J. Taylor, and Vijay Kumar, *Spatio-Temporally Smooth Local Mapping and State Estimation Inside Generalized Cylinders with Micro Aerial Vehicles*, IEEE Robotics and Automation Letters **3** (2018), no. 4, 4209–4216.

[41] Tolga Özaslan, Giuseppe Loianno, James Keller, Camillo J. Taylor, Vijay Kumar, Jennifer M. Wozencraft, and Thomas Hood, *Autonomous navigation and mapping for inspection of penstocks and tunnels with MAVs*, IEEE Robotics and Automation Letters **2** (2017), no. 3, 1740–1747.

[42] Tolga Özaslan, Kartik Mohta, James Keller, Yash Mulgaonkar, Camillo J. Taylor, Vijay Kumar, Jennifer M. Wozencraft, and Thomas Hood, *Towards fully autonomous visual inspection of dark featureless dam penstocks using MAVs*, IEEE International Conference on Intelligent Robots and Systems **2016-Novem** (2016), 4998–5005.

[43] Cosimo Patruno, Roberto Colella, Massimiliano Nitti, Vito Renò, Nicola Mosca, and Ettore Stella, *A vision-based odometer for localization of omnidirectional indoor robots*, Sensors (Switzerland) **20** (2020), no. 3.

[44] Vinicio Rosas-Cervantes and Soon Geul Lee, *3D Localization of a Mobile Robot by Using Monte Carlo Algorithm and 2D Features of 3D Point Cloud*, International Journal of Control, Automation and Systems **18** (2020), no. 11, 2955–2965.

[45] Dongqing Shi, Haiyan Mi, Emmanuel G. Collins, and Jun Wu, *An Indoor Low-Cost and High-Accuracy Localization Approach for AGVs*, IEEE Access **8** (2020), 50085–50090.

[46] S. A.I. Stent, C. Girerd, P. J.G. Long, and R. Cipolla, *A low-cost robotic system for the efficient visual inspection of tunnels*, 32nd International Symposium on Automation and Robotics in Construction and Mining: Connected to the Future, Proceedings (2015).

[47] Daniele Ventura, Stanislas F. Dubois, Andrea Bonifazi, Giovanna Jona Lasinio, Marco Seminara, Maria F. Gravina, and Giandomenico Ardizzone, *Integration of close-range underwater photogrammetry with inspection and mesh processing software: a novel approach for quantifying ecological dynamics of temperate biogenic reefs*, Remote Sensing in Ecology and Conservation **7** (2021), no. 2, 169–186.

[48] Haoran Wang, Shuang Wang, Chuncheng Feng, Yonglong Li, Yongcan Chen, and Hua Zhang, *Diversion Tunnel Defects Inspection and Identification Using an Automated Robotic System*, Proceedings - 2019 Chinese Automation Congress, CAC 2019 (2019), 5863–5868.

[49] Jacob Wilson, Meaghan Charest, and Rickey Dubay, *Non-linear model predictive control schemes with application on a 2 link vertical robot manipulator*, Robotics and Computer-Integrated Manufacturing **41** (2016), 23–30.

[50] Zheping Yan, Haoyu Yang, Wei Zhang, Qingshuo Gong, Yu Zhang, and Luoyin Zhao, *Robust nonlinear model predictive control of a bionic underwater robot with external disturbances*, Ocean Engineering **253** (2022).

[51] Haoyu Yang, Zheping Yan, Wei Zhang, Qingshuo Gong, Yu Zhang, and Luoyin Zhao, *Trajectory tracking with external disturbance of bionic underwater robot based on cpg and robust model predictive control*, Ocean Engineering **263** (2022).

[52] Feng Hui Yao, Gui Feng Shao, Hiroaki Yamada, and Kiyoshi Kato, *Development of an automatic concrete-tunnel inspection system by an autonomous mobile robot*, Proceedings - IEEE International Workshop on Robot and Human Interactive Communication (2000), 74–79.

[53] Fenghui Yao, Guifeng Shao, Ryoichi Takaue, and Akikazu Tamaki, *Automatic concrete tunnel inspection robot system*, Advanced Robotics **17** (2003), no. 4, 319–337.

[54] Seung Nam Yu, Jae Ho Jang, and Chang Soo Han, *Auto inspection system using a mobile robot for detecting concrete cracks in a tunnel*, Automation in Construction **16** (2007), no. 3, 255–261.

[55] Michalis Zervakis, *Vehicle Architecture for Regular Periodic Fish-cage Net Inspection*, (2017), 0–5.

Appendix A

Robot Kinematic Calculations

Table A.1: Modified Denavit-Hartenberg Parameters of the ATI.

Link	α_{i-1}	a_{i-1}	d_i	θ_i
1	0	0	0	θ_B^*
2	$\pi/2$	l_2	D_B^*	0
3	$-\pi/2$	0	0	θ_T^*
4	0	l_4	d_4	0

$$ {}^{Base}_{1}T = \left[\begin{array}{c:c:c:c} c_B & -s_B & 0 & 0 \\ s_B & c_B & 0 & 0 \\ 0 & 0 & 1 & 0 \\ 0 & 0 & 0 & 1 \end{array}\right] \tag{A.1} $$

$$ {}^{1}_{2}T = \left[\begin{array}{c:c:c:c} 1 & 0 & 0 & l_2 \\ 0 & 0 & -1 & D_B \\ 0 & 1 & 0 & 0 \\ 0 & 0 & 0 & 1 \end{array}\right] \tag{A.2} $$

$$ {}^{2}_{3}T = \left[\begin{array}{c:c:c:c} c_T & -s_T & 0 & 0 \\ s_T & c_T & 0 & 0 \\ 0 & 0 & 1 & 0 \\ 0 & 0 & 0 & 1 \end{array}\right] \tag{A.3} $$

$$ {}^{3}_{4}T = \left[\begin{array}{c:c:c:c} 1 & 0 & 0 & l_4 \\ 0 & 1 & 0 & d_4 \\ 0 & 1 & 1 & 0 \\ 0 & 0 & 0 & 1 \end{array}\right] \tag{A.4} $$

$$
{}^{Base}_{Arm}T = \left[\begin{array}{c:c:c:c} c_B c_T - s_B s_T & s_B c_T - c_B s_T & 0 & l_2 c_B + d_B s_B + l_4 \\ c_B s_T - s_B c_T & c_B c_T - s_B s_T & 0 & l_2 s_B - d_B c_B + d_4 \\ 0 & 0 & 1 & 0 \\ 0 & 0 & 0 & 1 \end{array}\right] \tag{A.5}
$$

$$
\theta_B = -\theta_T + \theta_{Slant} = atan2(y_{Tip}, x_{Tip}) = atan2((y_{Arm-d_4}), (x_{Arm} - l_4)) \tag{A.6}
$$

$$
D_B = d_B + \hat{d}_B = \sqrt{x_{Tip}^2 + y_{Tip}^2} = \sqrt{(x_{Arm} - l_4)^2 + (y_{Arm-d_4})^2} \tag{A.7}
$$

$$
\theta_B = acos\left(\frac{-(d_L + \hat{d}_L)^2 + \alpha_L^2 + \beta_L^2}{2\alpha_L\beta_L}\right) + acos\left(\frac{\beta_L^2 - \lambda_L^2 + \rho_L^2}{2\beta_L\rho_L}\right) - atan\left(\frac{\gamma_L}{\phi_L}\right) \tag{A.8}
$$

$$
\begin{aligned} d_L &= \sqrt{-2\alpha_L\beta_L A_L + {\alpha_L}^2 + {\beta_L}^2} - \hat{d}_L, \\ where, \quad A_L &= cos\left[\theta_L - acos\left(\frac{\beta_L^2 - \lambda_L^2 + \rho_L^2}{2\beta_L\rho_L}\right) + atan\left(\frac{\gamma_L}{\phi_L}\right)\right] \end{aligned} \tag{A.9}
$$

$$
\theta_T = acos\left(\frac{-(d_T + \hat{d}_T)^2 + {\alpha_T}^2 + {\beta_T}^2}{2\alpha_T\beta_T}\right) - acos\left(\frac{{\beta_T}^2 - {\lambda_T}^2 + {\rho_T}^2}{2\beta_T\rho_T}\right) - atan\left(\frac{\gamma_T}{\phi_T}\right) \tag{A.10}
$$

$$
\begin{aligned} d_T &= \sqrt{-2\alpha_T\beta_T A_T + {\alpha_T}^2 + {\beta_T}^2} - \hat{d}_T, \\ where, \quad A_T &= cos\left[\theta_T + acos\left(\frac{\beta_T^2 - \lambda_T^2 + \rho_T^2}{2\beta_T\rho_T}\right) + atan\left(\frac{\gamma_T}{\phi_T}\right)\right] \end{aligned} \tag{A.11}
$$

Table A.2: Parameter definitions for driving actuators of the lift and tip joints.

Lift		**Tip**	
Label	**Value**	**Label**	**Value**
α_L	BC	α_T	EG
β_L	BD	β_T	EF
γ_L	AB	γ_T	EH
λ_L	BJ	λ_T	EJ
ϕ_L	AC	ϕ_T	HG
ρ_L	DJ	ρ_T	FJ
D_L	DC	D_T	GF

Figure A.1: ATI joint frame and DH parameter definitions.

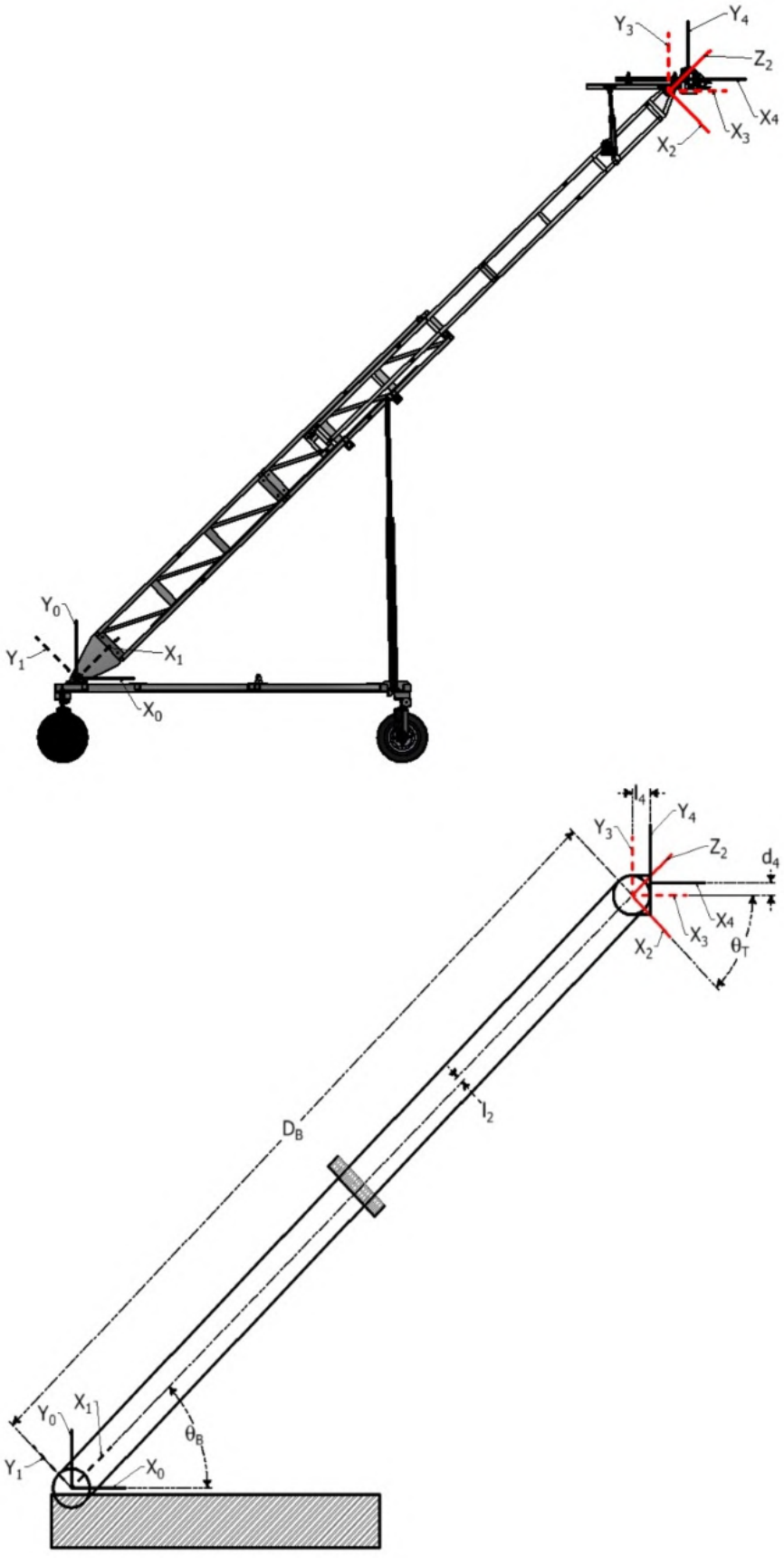

Figure A.2: Defining parameters relating driving actuator of boom inclination joint.

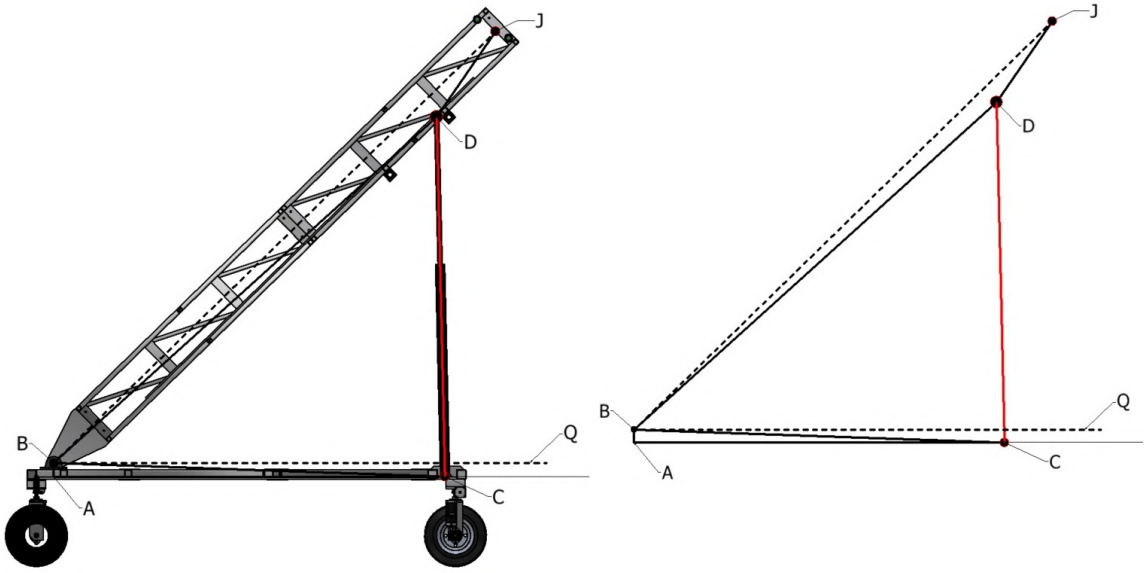

Figure A.3: Defining parameters relating driving actuator of tip inclination joint.

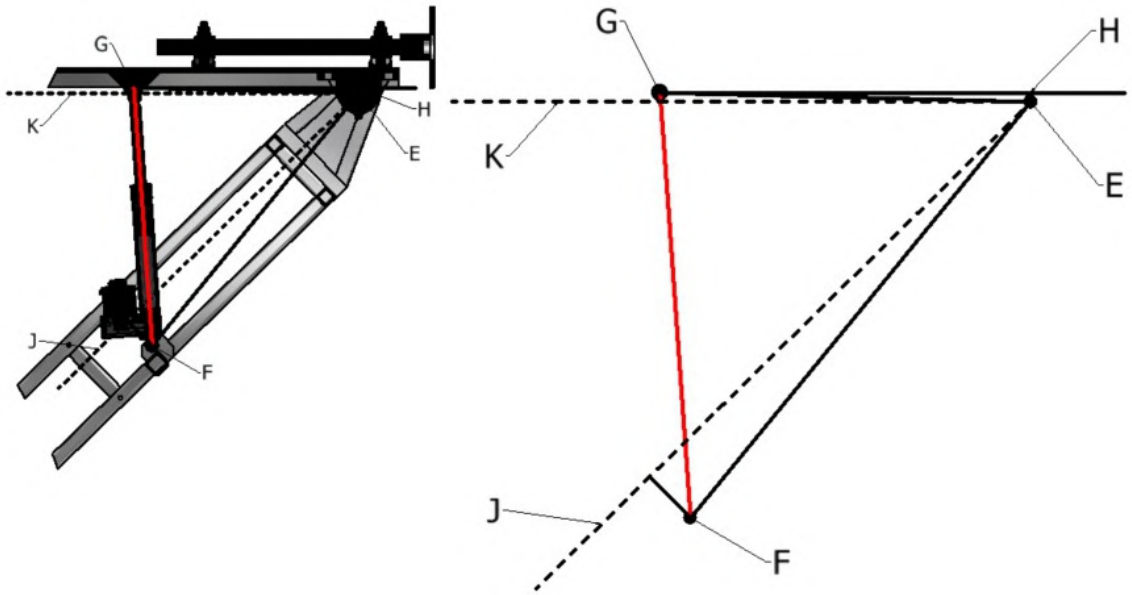

Appendix B

ATI Details and Visuals

Figure B.1: ATI in the Grand Falls tunnel.

Figure B.2: ATI actuation definitions.

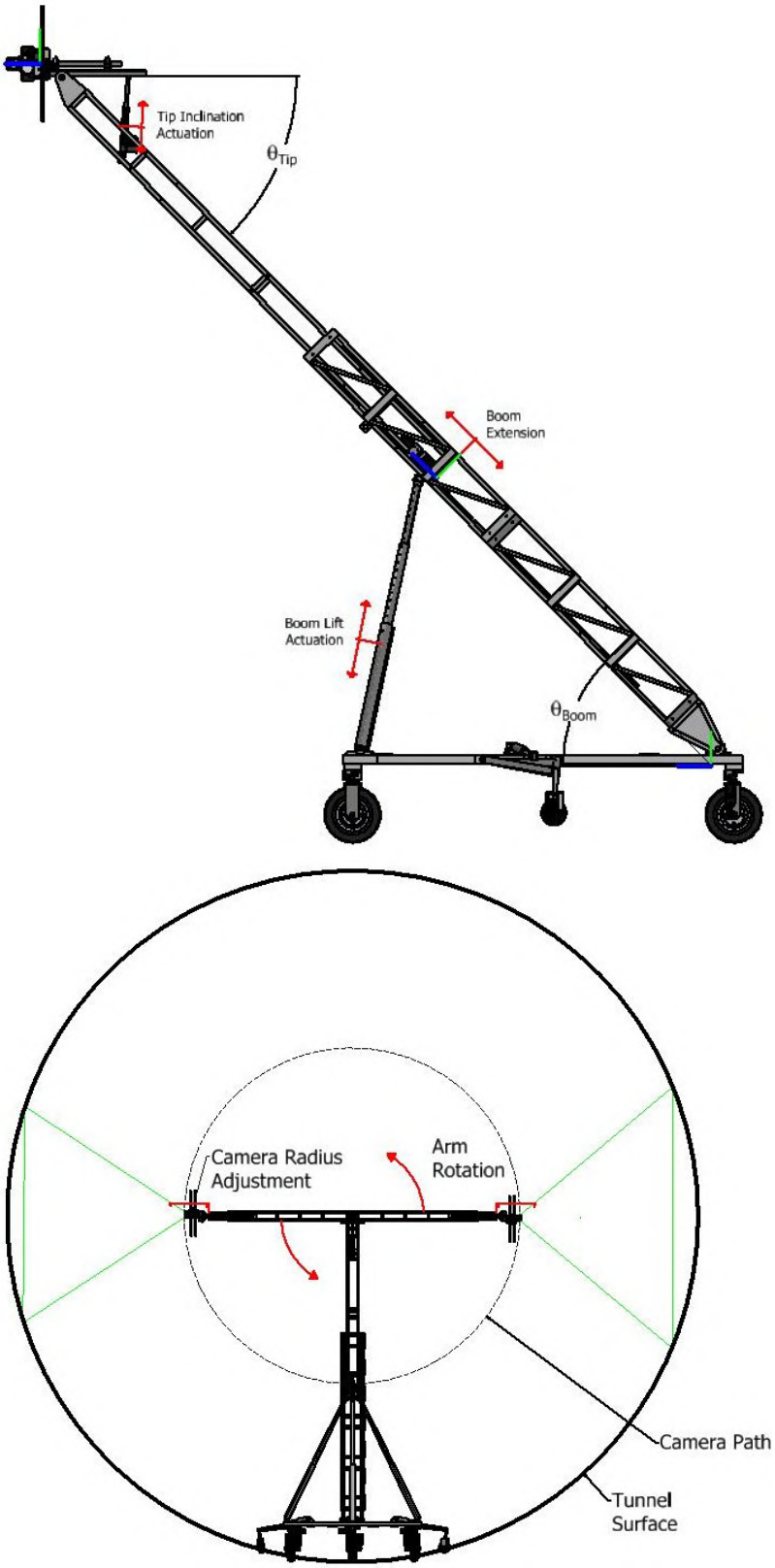

Figure B.3: ATI in the shop and testing environment.

Figure B.4: ATI model in different extensions.

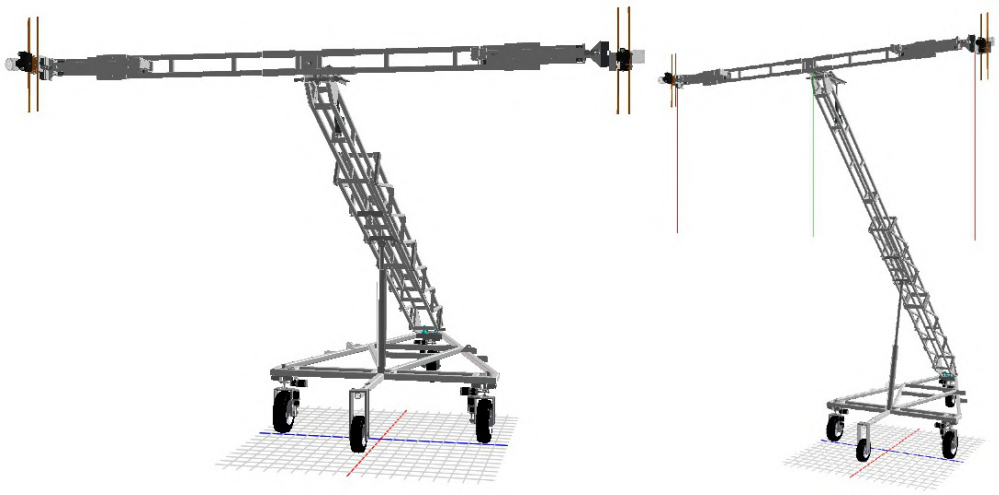

Figure B.5: Boom tip system: tip inclination actuator and arm rotation platform.

Table B.1: Linear Actuator Summary

Action	Actuator	Stroke	Force	Feedback	Manufacturer
Radial Extension	FA-OS-240-12-18	18 in.	200 lb	Optical	Firgelli Auto
Boom Lift	FA-BH50-1124-12-30	30 in.	1124 lb	Hall Effect	Firgelli Auto
Tip Inclination	FA-PO-150-12-6	6 in.	150 lb	Potentiometer	Firgelli Auto
Outriggers	8507824	6 in.	270 lb	N/A	Hydroworks
Boom Extension	PKP266D42B2 / PLE60-40B	inf	40 Nm	N/A	Oriental Motor
Arm Rotation	PKP2913D45A / PLE80-40B	inf	110 Nm	N/A	Oriental Motor
Steer Rotation	PKP2913D45A / PLE80-40B	inf	110 Nm	N/A	Oriental Motor
Drive Motor	BLY343D-48V-1000/ GBPH-0902-NS-100-AA341-500	inf	240 Nm	Hall Effect	Anaheim Automation

Appendix C

Additional Control Data

Figure C.1: Experimental stroke response of the lift actuator from various inputs.

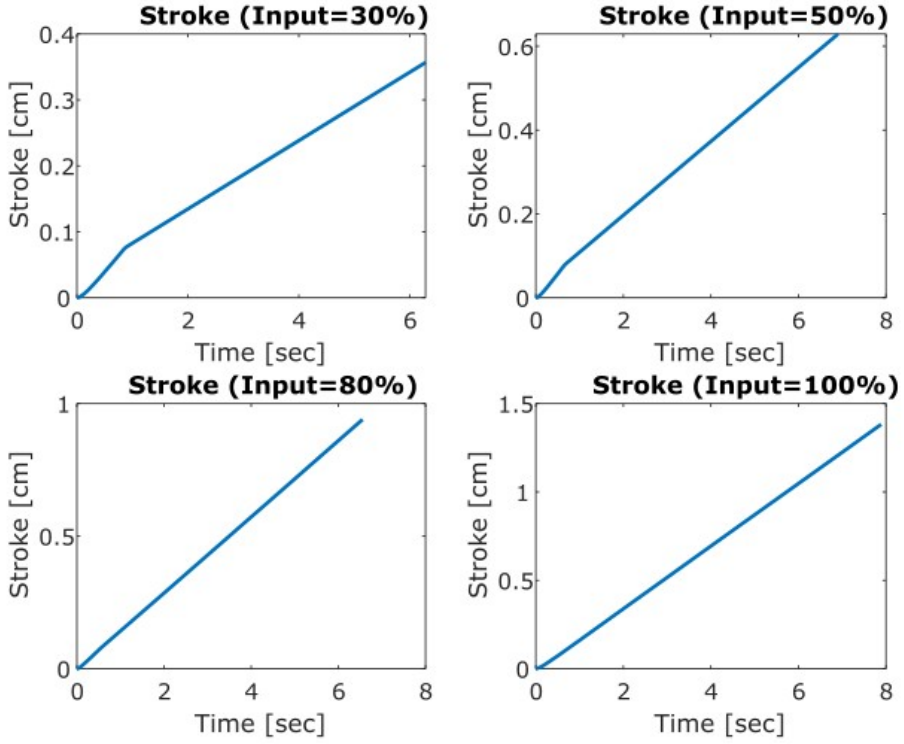

Figure C.2: Experimental responses showing the effect of load on speed and stroke of the arm extension actuators.

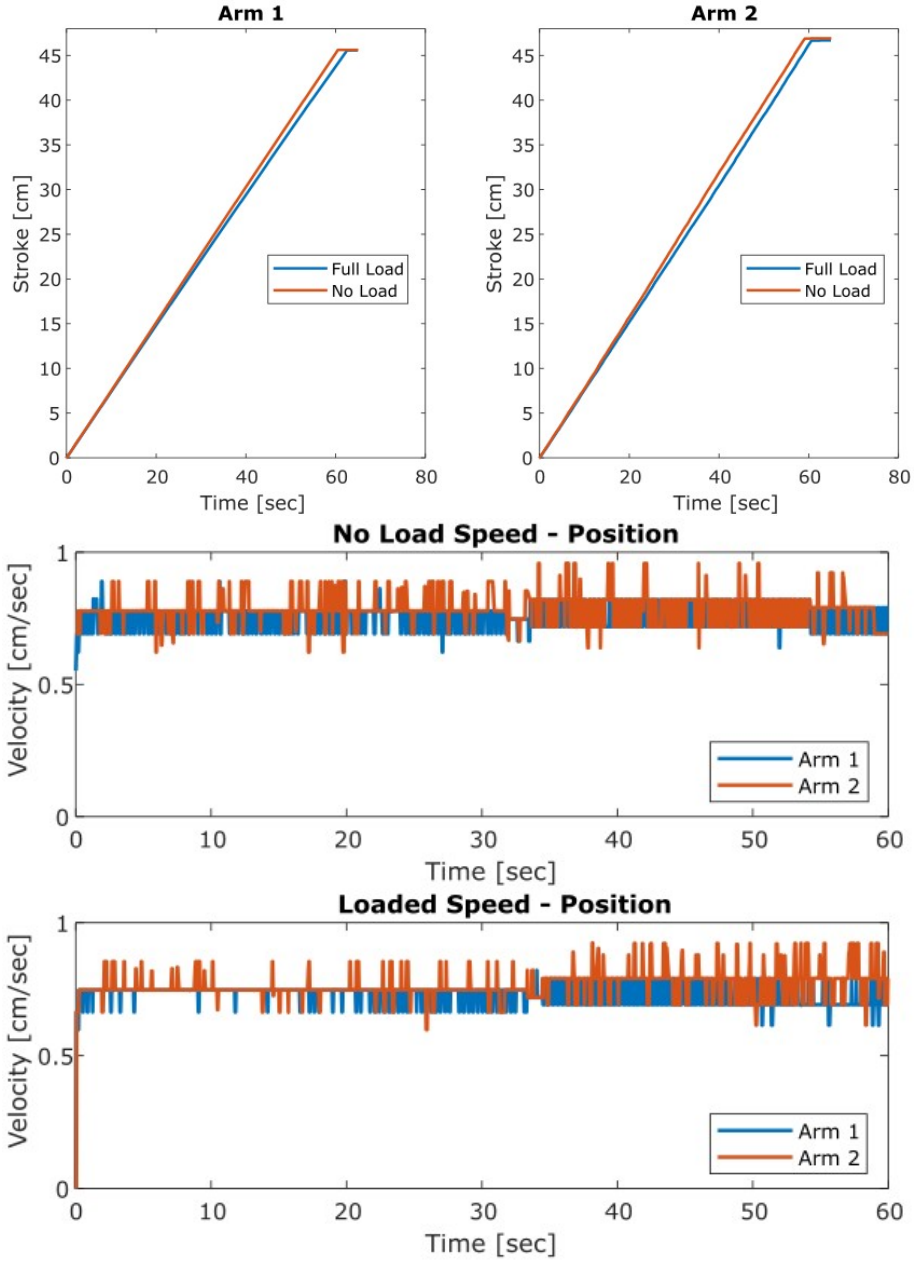

Figure C.3: Open loop drive wheel responses at various inputs.

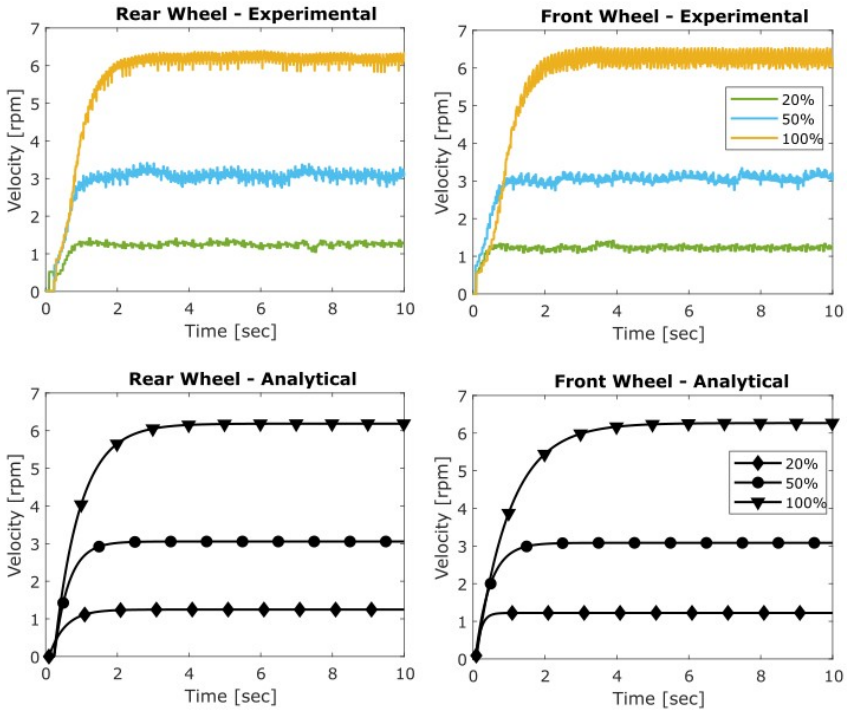

Figure C.4: Open loop drive wheel responses at various low range inputs.

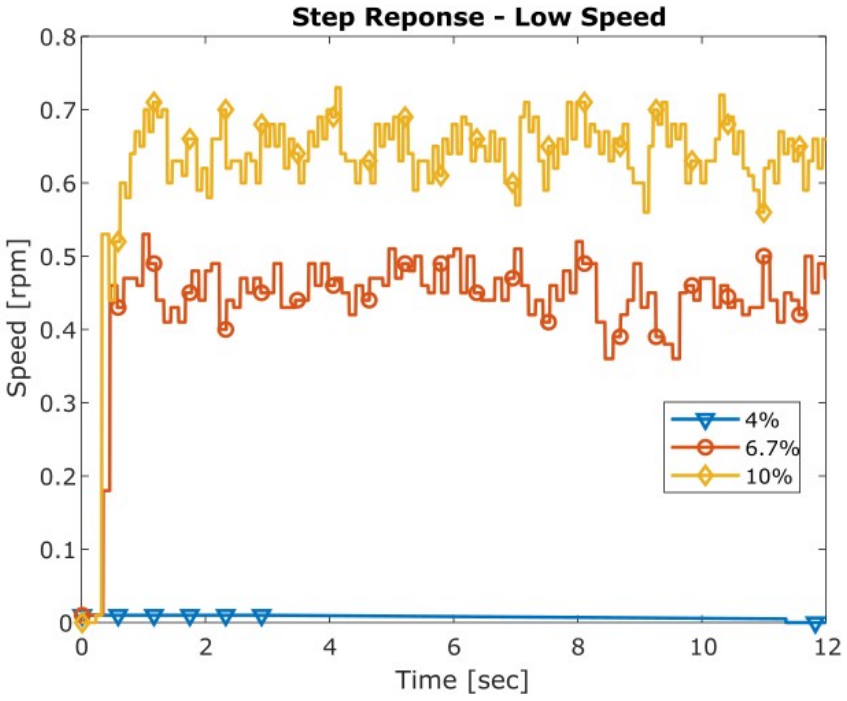

Figure C.5: Simulated responses from each wheel's estimated analytical model at various mid range inputs.

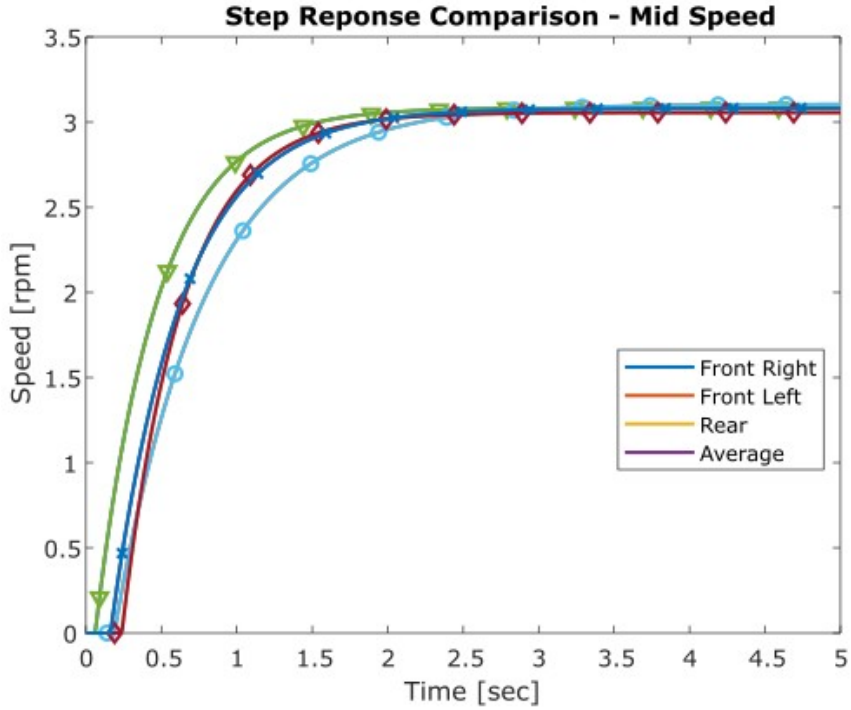

Table C.1: Summary of estimated model data from open loop data

System Description	**Steady State Speed [rpm]**	**System Gain**	**Time Constant [sec]**	**System Delay [sec]**
Front Right Wheel - Low Speed	1.2223	0.02445	0.1377	0.07956
Front Right Wheel - Mid Speed	3.0835	0.02467	0.410032	0.061208
Front Right Wheel - High Speed	6.2667	0.02458	0.939252	0.0867
Front Left Wheel - Low Speed	1.2508	0.02502	0.234092	0.34476
Front Left Wheel - Mid Speed	3.1043	0.02483	0.59534	0.188696
Front Left Wheel - High Speed	6.1982	0.02431	0.82654	0.330308
Rear Wheel - Low Speed	1.2474	0.02495	0.44506	0.09248
Rear Wheel - Mid Speed	3.0556	0.02444	0.401712	0.237828
Rear Wheel - High Speed	6.1866	0.02426	0.7208	0.228608

Curriculum Vita

Candidates Full Name:	Ryan Daniel Keizer
Universities Attended:	University of New Brunswick Fredericton, New Brunswick Bachelor of Science in Engineering (Mechanical /Mechatronics Option) [First Division] 2016-2021

Publications and Conference Presentations:

R. Keizer, R. Dubay, L. Waugh and C. Bradley, "Robotic Camera Positioning System for Inspection of Tunnels: A Conceptual Design," 2022 IEEE International Systems Conference (SysCon), Montreal, QC, Canada, 2022, pp. 1-8.

R. Keizer, C. Bradley, L. Waugh, and R. Dubay, "Vehicle concepts for the photogrammetric inspection of Hydroelectric Tunnels," Transforming Construction with Reality Capture Technologies, Fredericton, New Brunswick, Canada, 2022.

R. Keizer, "Mobile Robotic Camera Positioning System for Hydroelectric Tunnel Inspection," Mechanical Engineering Graduate Society Conference, Fredericton, New Brunswick, Canada, 2022.